
Hit reconstruction for the Silicon Tracking System of the CBM experiment

Dissertation
zur Erlangung des Doktorgrades
der Naturwissenschaften

vorgelegt beim Fachbereich Physik
der Johann Wolfgang Goethe-Universität
in Frankfurt am Main

von
Hanna Malygina (geb. Melnyk)
aus Varash (Kuznetsovsk), Ukraine

Frankfurt am Main (2018)
(D 30)

vom Fachbereich Physik der
Johann Wolfgang Goethe-Universität als Dissertation angenommen.

Dekan: Prof. Dr. Owe Philipsen

Gutachter: Prof. Dr. Peter Senger
Prof. Dr. Joachim Stroth

Datum der Disputation: 2018

Abstract

The mission of the Compressed Baryonic Matter (CBM) experiment is to investigate the phase diagram of strongly interacting matter in the region of high net-baryon densities and moderate temperatures. According to various transport models, matter densities of more than 5 times saturation density can be reached in collisions between gold nuclei at beam energies between 5 and 11 GeV per nucleon, which will be available at FAIR. The core detector of the CBM experiment is the Silicon Tracking System (STS), which is used to measure the tracks of up to 700 particles per collision with high efficiency ($> 95\%$) and good momentum resolution ($< 1.5\%$). The technological and experimental challenge is to realize a detector system with very low material budget, in order to reduce multiple scattering of the particles, and a free-streaming data readout chain, in order to achieve reaction rates up to 10 MHz together with an online event reconstruction and selection. The STS comprises 8 tracking stations positioned between 30 cm and 100 cm downstream the target inside a magnetic field, covering polar emission angles up to 25 degrees. A station consists of vertical structures with increasing number (between 8 and 16, depending on station number), each structure carrying between 2 and 10 double-sided microstrip silicon sensors, which are connected through low-mass microcables to the readout electronics placed at the detector periphery outside the active detector area.

The work presented in this thesis focuses on the detector performance simulation and local hit pattern reconstruction in the STS. For efficient detector design and reconstruction performance, a reliable detector response model is of utmost importance. Within this work, a realistic detector response model was designed and implemented in the CBM software framework. The model includes non-uniform energy loss of an incident particle within a sensor, electric field of a planar p-n junction, Lorentz shift of the charge carriers, their diffusion, and the influence of parasitic capacitances. The developed model has been verified with experimental data from detector tests in a relativistic proton beam. Cluster size distributions at different beam incident angles are sensitive to charge sharing effects and were chosen as an observable for the verification. Taking into account parasitic capacitances further improves the agreement with measured data.

Using the developed detector response model, the cluster position finding algorithm was improved. For two-strip clusters, a new, unbiased algorithm has been developed, which gives smaller residuals than the Centre-Of-Gravity algorithm. For larger clusters, the head-tail algorithm is used as the default one. For an estimate of the track parameters, the Kalman Filter based track fit requires not only hit positions but their uncertainties as an input. A new analytic method to estimate the hit position errors has been designed in this work. It requires as input neither measured spatial resolution nor information about an incident particle track. The method includes all the sources of uncertainties independently, namely: the cluster position finding algorithm itself, the non-uniform energy loss of incident particles,

the electronics noise, and the discretisation of charge in the readout chip. The verification with simulations shows improvements in hit and track pull distributions as well as χ^2 -distributions in comparison to the previous simple approach. The analytic method improves the track parameters reconstruction by 5 – 10 %.

Several STS module prototypes have been tested in a relativistic proton beam. A signal-to-noise ratio was obtained at the level of 10 – 15 for modules made of 30 cm long microcable and of either one or two $6.2 \times 6.2 \text{ cm}^2$ CiS sensors. First simulations have shown that this signal-to-noise ratio is sufficient to reach the required efficiency and momentum resolution. The high-radiation environment of CBM operation will deteriorate the sensor performance. Radiation hardness of sensors has been studied in the beam with sensors irradiated to $2 \times 10^{14} \text{ 1 MeV } n_{\text{eq}}/\text{cm}^2$, twice the lifetime dose expected for CBM operation. Charge collection efficiency drops by 17 – 25 %, and simultaneously noise levels increase 1.5 – 1.75 times. The simulations show that if all sensors in the STS setup are exposed to such a fluence uniformly, the track reconstruction efficiency drops from 95.5 % to 93.2 % and the momentum resolution degrades from 1.6 % to 1.7 %.

Kurzfassung

Das Ziel des Experimentes CBM (Compressed Baryonic Matter) ist es, das Phasendiagramm von stark wechselwirkender Materie bei hohen Baryonendichten und moderaten Temperaturen zu untersuchen. Transportmodellen folgend können in Kollisionen von Goldkernen bei Strahlenergien zwischen 5 und 11 GeV pro Nukleon, wie sie von der Beschleunigeranlage FAIR bereitgestellt werden, Dichten von bis zu dem Fünffachen der normalen Dichte von Atomkernen erreicht werden. Das Herzstück des CBM-Experimentes ist das Silicon Tracking System (STS), in welchem die Spuren von bis zu 700 Teilchen pro Kollision mit hoher Effizienz ($> 95\%$) und guter Impulsauflösung ($< 1,5\%$) nachgewiesen werden. Die technische Herausforderung ist es, dies mit einem Detektorsystem mit minimalen Materialbudget zu erreichen, um den Einfluß von Kleinwinkelstreuung der Teilchen möglichst gering zu halten. Um hohe Reaktionsraten von bis zu 10 MHz messen und in Echtzeit auswerten zu können, ist ferner eine freilaufende, selbstgetriggerte Datenauslese erforderlich. Das STS besteht aus acht Detektorstationen, die innerhalb des magnetischen Dipolfeldes im Abstand von 30 bis 100 cm vom Target positioniert sind. Es deckt Polarwinkel bis zu 25 Grad ab. Jede Station besteht aus einer Anzahl von vertikalen Strukturen ("Leitern"), von denen jede wiederum zwischen zwei und zehn doppelseitige Mikrostreifensensoren trägt. Die Sensoren werden durch niedrigmassige Analogkabel mit der Ausleseelektronik verbunden, die an der Detektorperipherie, außerhalb der aktiven Zone, angebracht ist.

Die in dieser Dissertation vorgestellte Arbeit beschäftigt sich mit Simulationen der Detektorperformanz und der Rekonstruktion der Position der Durchstoßpunkte von Teilchenspuren im STS, eine Voraussetzung für die Rekonstruktion der Trajektorien und somit ihrer Impulsbestimmung. Für ein optimales Detektordesign und gute Rekonstruktionsperformanz ist ein verlässliches und realistisches Modell der Detektorantwort auf den Durchgang von geladenen Teilchen unverzichtbar. Im Rahmen dieser Dissertation wurde ein solches Detektormodell entwickelt und innerhalb der CBM-Softwareumgebung implementiert. Das Modell berücksichtigt den Energieverlust der Teilchen im Detektormaterial, die Erzeugung und Propagation von Elektron-Loch-Paaren im elektrischen Feld der p-n-Halbleitergrenze, die Lorentz-Verschiebung der driftenden Ladungsträger im äußeren Magnetfeld, ihre thermische Diffusion sowie den Einfluß parasitärer Kapazitäten. Das entwickelte Modell wurde anhand experimenteller Daten aus Detektortests mit relativistischen Protonenstrahlen validiert. Als Observable für die Validierung wurde die Verteilung der Clustergröße für verschiedene Einfallswinkel gewählt, da diese eine deutliche Abhängigkeit von Ladungsteilungseffekten und parasitären Kapazitäten aufweist.

Mit Hilfe des entwickelten Detektormodelles wurde ferner der Algorithmus zur Bestimmung der Teilchenposition (Cluster Fitting) verbessert. Für Cluster aus zwei Streifen wurde ein neuer Algorithmus implementiert, der genauer ist als die üblicherweise benutzte Bestimmung des Ladungsschwerpunktes. Für größere Cluster

wird der sogenannte Head-Tail-Algorithmus benutzt, der nur die Information aus dem ersten und letzten Streifen eines Clusters verwendet. Eine gute Kenntnis nicht nur der Position, sondern auch von deren Fehler ist von großer Bedeutung für die Genauigkeit moderner Spurrekonstruktionsalgorithmen wie dem in CBM verwendeten Kalman-Filter. Eine neue analytische Methode zur Bestimmung des Positionsfehlers wurde daher ebenfalls im Rahmen dieser Arbeit entwickelt. Diese Methode benötigt weder Informationen über gemessene Ortsauflösung noch über die Teilchentrajektorie. Sie berücksichtigt alle bekannten Quellen von Unsicherheit, wie diejenige aus der Integration von Ladung auf den Auslesestreifen, fluktuierender Energieverlust der Teilchen im Detektor, elektronisches Rauschen und die Ladungsdiskretisierung in der Ausleseelektronik. Die neue, analytische Methode verbessert die Auflösung der Spurparameter um 5 – 10 % gegenüber der bisherigen, einfacheren Implementierung. Mehrere STS-Sensorprototypen wurden in einem Protonenstrahl getestet. Ein Signal-zu-Rausch-Verhältnis von 10 bis 15 wurde für Module gemessen, die aus einem oder zwei Sensoren der Größe $6,2 \times 6,2 \text{ cm}^2$ und aus einem 30 cm langen Mikrokabel bestanden. Simulationen zeigen, dass dieser Wert hinreichend ist, um die gewünschte Effizienz und Impulsauflösung zu erreichen. Die hohe Strahlenbelastung während der Betriebszeit des CBM-Experimentes wird allerdings die Sensoreigenschaften verschlechtern. Zum Studium dieser Beeinträchtigung wurden Sensoren einer Strahlendosis von $2 \times 10^{14} \text{ 1 MeV } n_{\text{eq}}/\text{cm}^2$ ausgesetzt; dies entspricht dem zweifachen der in CBM erwarteten Lebensdosis. Durch die Bestrahlung sinkt die Effizienz um 17 bis 25 %; gleichzeitig erhöht sich das Rauschen um einen Faktor 1,5 bis 1,75. Simulationen zeigen, dass unter der Annahme, dass alle Sensoren dieser Strahlendosis gleichförmig ausgesetzt sind, die Spurrekonstruktionseffizienz von 95,5 auf 93,2 % absinkt; die Impulsauflösung verschlechtert sich lediglich von 1,6 auf 1,7 %.

Contents

1	INTRODUCTION	8
1.1	Exploration of the phase diagram of strongly interacting matter . . .	8
1.2	The Facility for Antiproton and Ion Research	12
1.3	The Compressed Baryonic Matter experiment	13
1.4	The Silicon Tracking System	17
1.5	Motivation for reliable detector response model	22
1.6	Silicon detectors	22
2	DETECTOR RESPONSE MODEL	26
2.1	Simulation of silicon detectors	26
2.1.1	Energy loss simulation	27
2.1.2	Transport of electron-hole pairs	28
2.1.2.1	Description of the electric field	29
2.1.2.2	Diffusion	31
2.1.2.3	Magnetic field	33
2.1.3	Cross-talk effect	34
2.1.4	Modelling of the response of the readout electronics	35
2.2	Implementation	36
2.2.1	Overview of existing digitizers	36
2.2.2	Implementation of a realistic STS digitizer	39
2.2.2.1	Energy loss model	39
2.2.2.2	Charge carrier transport	40
2.2.2.3	Additional effects	41
2.2.2.4	Influence of the modelled effects on the performance	46
2.3	Comparison with the simple model	48
2.3.1	Digi level	48
2.3.2	Cluster level	49
2.3.3	Hit level	52
2.3.4	Track level	53
2.4	Summary	54

3	STS CLUSTER AND HIT RECONSTRUCTION	56
3.1	Cluster reconstruction	56
3.1.1	Centre-of-Gravity algorithm	59
3.1.2	The unbiased algorithm	62
3.1.3	Algorithms comparison	64
3.2	Hit reconstruction	67
3.3	Estimation of the hit position error	68
3.3.1	Overview of existing methods for estimation of the hit position error	69
3.3.1.1	Vertex Locator of LHCb	69
3.3.1.2	The strip detector of the CMS tracker	70
3.3.1.3	Estimation of resolution from experimental data and simulation	70
3.3.2	Development of the analytic method	71
3.3.2.1	General idea of estimation of hit position error	71
3.3.2.2	Error of the cluster position finding algorithm	72
3.3.2.3	Error due to non-uniformity of energy loss	72
3.3.2.4	Additional source of errors	73
3.3.3	Hit position error verification	73
3.3.3.1	Hit position pull distribution	74
3.3.3.2	Track reconstruction	75
3.3.3.3	Particle reconstruction	79
3.4	Summary	80
4	EVALUATION OF DETECTOR RESPONSE IN A RELATIVISTIC PROTON BEAM	82
4.1	Experimental setup	82
4.2	Beamtime data analysis	90
4.2.1	Signal-to-noise ratio	93
4.2.2	Radiation hardness of the sensors	96
4.3	Detector response model verification	98
4.4	Summary	103
5	SUMMARY AND CONCLUSIONS	105
APPENDIX A ADDITIONAL PLOTS FOR COMPARISON OF THE DETECTOR RESPONSE MODELS		108
APPENDIX B URBAN METHOD		112
APPENDIX C 2-STRIP CLUSTERS		115
C.1	The unbiased CPFA	117
C.2	The Centre-of-Gravity CPFA	118

APPENDIX D N-STRIP CLUSTERS IN THE UNBIASED ALGORITHM	120
APPENDIX E DATA FROM THE IN-BEAM TESTS	122
E.1 Test of irradiated sensors	122
E.2 Test of modules	128
E.3 Cluster size distribution	134
APPENDIX F INFLUENCE OF THE MICRO-CABLES ON THE CHARGE COL- LECTION	135
LIST OF ACRONYMS	137
ZUSAMMENFASSUNG	139
BIBLIOGRAPHY	144
ACKNOWLEDGEMENTS	155

1

Introduction

1.1 EXPLORATION OF THE PHASE DIAGRAM OF STRONGLY INTERACTING MATTER

Significant efforts have been made so far to explore the phase diagram of strongly interacting matter [1]. The region of high temperatures has been investigated experimentally at RHIC (Relativistic Heavy Ion Collider) [2] and LHC (Large Hadron Collider) [3] experiments using heavy-ion collisions at very high energies [4–8]. In such collisions, the matter is produced at low net baryon densities, i.e. with almost equal amount of baryons and antibaryons. Similar conditions are predicted to exist in the early universe several microseconds after the big bang. After hadronization, the system freezes out chemically at a temperature around 160 MeV [9]. This temperature coincides with the transition temperature predicted by Lattice QCD calculations for a chiral phase transition, which is found to be a smooth cross-over from partonic to hadronic matter [10].

Model calculations predict structures in the phase diagram at large baryon chemical potentials, such as a first order phase transition between hadronic and partonic matter, with a critical endpoint. Figure 1.1 illustrates the result of such a model [11]. In the hadronic phase, quarks and gluons cannot exist as free particles, they are confined (shown in yellow). At high temperatures and densities, a new state of matter, Quark-Gluon Plasma (QGP), can be created (shown in red). In such a state, quarks and gluons are deconfined and can move freely. A quarkyonic phase is predicted to exist in between, which has properties of both high density baryonic matter and deconfined and chirally symmetric quark matter. At very high baryon chemical potential and low temperature, one may anticipate that the ground state of strongly

interacting matter should form Cooper pairs leading to colour superconductivity (shown in blue).

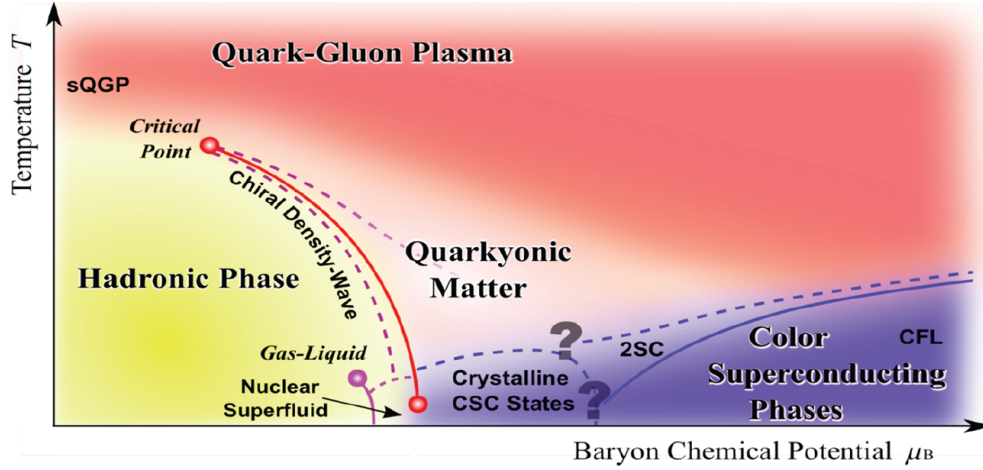


Figure 1.1: Phase diagram of strongly-interacting matter [11].

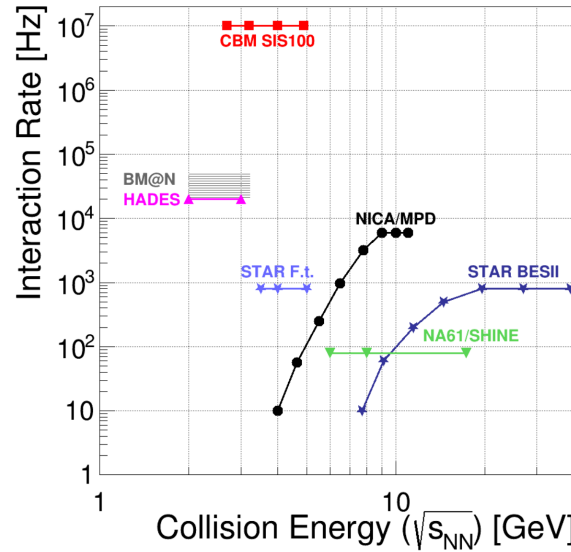


Figure 1.2: Interaction rates of existing and planned experiments devoted to exploration of the phase diagram of strongly interacting matter at high net baryon densities [12]. The CBM experiment will run at unprecedented interaction rate: 2-3 orders of magnitude higher than other experiments.

Investigation of the properties, the equation of state and the degrees of freedom of dense baryonic matter is of fundamental interest, also for our understanding of astrophysical objects, such as neutron stars and neutron star mergers [11, 13]. According to model calculations, heavy-ion collisions at moderate beam energies are very suitable to produce and to investigate strongly interacting matter at very

high net baryon densities in laboratory experiments. There are several existing and planned experiments with focus on this collision energy: the beam energy scan at STAR¹ at RHIC [15], NA61 at SPS² with light and medium size ions [16], MPD³ at the NICA⁴ facility at JINR⁵ [17], HADES⁶ at SIS18 [18], and the BM@N⁷ experiment at JINR [19]. However, the expected yields of the observables for the experiments mentioned above are limited by low interaction rates or detector constraints [12]. The rate capabilities of existing and future heavy-ion experiments are shown in fig. 1.2. The Compressed Baryonic Matter (CBM) experiment at FAIR (Facility for Antiproton and Ion Research) [20] is designed to run at high interaction rates (up to 10 MHz) and is capable of measuring both bulk and rare probes with high precision [21]. The CBM experiment will run with gold beam energies from 2 – 11 AGeV. According to the different models predictions, in central Au+Au collisions already at 5 AGeV, the nuclear fireball will be compressed to more than 6 times saturation density and will spend a relatively long time within the phase coexistence region or even beyond (see fig. 1.3).

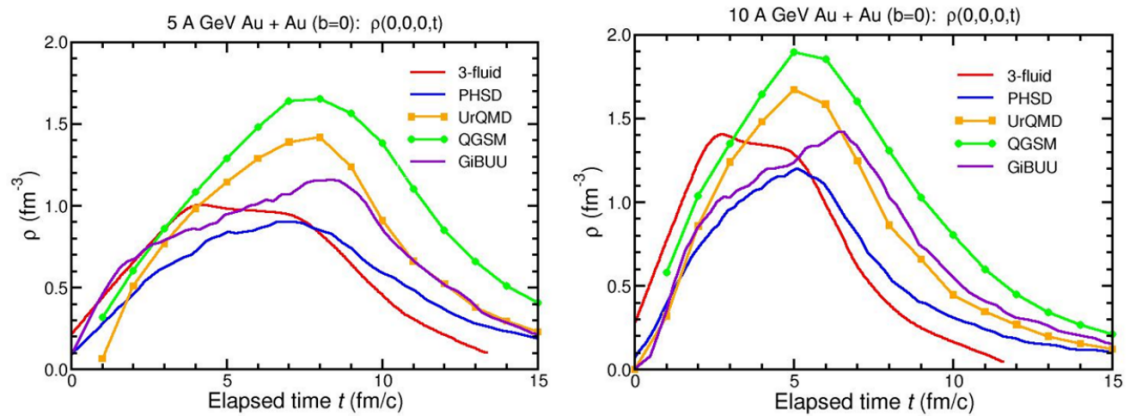


Figure 1.3: Evolution of the central net baryon density as a function of elapsed time. Calculations were done by different transport models and 3-fluid hydrodynamics code for central Au+Au collision at 5 AGeV (*left panel*) and 10 AGeV (*right panel*) [22].

A comprehensive study of the phase diagram at high net-baryon densities is the main focus of the CBM physics program. Operating at intermediate beam energies, where baryonic matter is expected to be compressed most, CBM will be able to address the following questions:

¹Solenoidal Tracker at RHIC [14]

²Super Proton Synchrotron, CERN, Switzerland

³Multi-Purpose Detector

⁴Nuclotron-based Ion Collider fAcility

⁵Joint Institute for Nuclear Research, Russia

⁶High Acceptance Di-Electron Spectrometer

⁷Baryonic Matter at Nuclotron

- Does the phase diagram of nuclear matter exhibit structures like a first order phase transition and a critical point at high densities? The following observables yield information:
 - The existence of a plateau in the caloric curve (the fireball temperature vs. the collision energy) would indicate a first-order phase transition [23]. The slope of the invariant mass distribution of dilepton pairs can serve as a temperature measurement [24]. The region $1 - 2.5 \text{ GeV}/c^2$ refers to the thermal radiation of dilepton pairs.
 - The directed flow of hadrons is sensitive to the details of the phase transition [25].
 - Yields of strange hadrons consistent with the thermal model are indicators of the phase transition (in particular Ω baryons) [26]. The equilibration of strange baryons could not be understood in terms of hadronic two-body relaxation processes in the limited life time of the fireball. If system undergoes a transition from a partonic phase to the hadronic final state, the equilibration is driven by multi-body collisions in the high particle density regime near the phase boundary.
 - Lattice QCD calculations show that high-order event-by-event fluctuations of conserved quantities (electrical charge, baryon number, strangeness) are expected to be sensitive to the proximity of the critical point [27, 28].
 - The existence of QGP can be confirmed by charmonium suppression [29]. This effect is expected due to colour screening of heavy quarks in the deconfined phase.
- Is there a **restoration of the chiral symmetry** at high densities?
 - An important consequence of this effect is the in-medium modifications of hadrons. Particularly, the spectral function of vector mesons (for example, ρ -meson) will be modified [30]. The invariant mass distribution will be investigated via lepton pair measurements for different collision systems. The thermal radiation includes a broadened in-medium ρ -meson, radiation from the QGP, and dileptons from multi-pion annihilation. The latter reflects $\rho - a_1$ chiral mixing and, therefore, provides a direct link to chiral symmetry restoration.
- What is the **equation of state of the nuclear matter** at high net baryon density?
 - This question can be answered by measurements of collective flow of hadrons, which is generated by the density gradient of the early fireball [31, 32].
 - Directed flow v_1 is sensitive to the softening of the equation of state [25].

- Splitting in the elliptic flow v_2 for different particle types is determined by the baryon chemical potential [33].
- Other promising observables are multi-strange hyperons, which are produced in sequential collisions of Λ hyperons and kaons, and, therefore, they are sensitive to the fireball density [34]. This sensitivity is largest at lower beam energies close to or even below the production threshold in elementary collisions.

1.2 THE FACILITY FOR ANTIPROTON AND ION RESEARCH

The international Facility for Antiproton and Ion Research in Darmstadt will provide wide research opportunities in the fields of nuclear, hadron, atomic and plasma physics [20, 35]. The upgraded existing GSI (GSI Helmholtzzentrum für Schwerionenforschung) accelerators UNILAC (Universal Linear Accelerator) and SIS18 (SchwerIonenSynchrotron) will serve as injectors. They will be followed by a superconducting double-synchrotron SIS100 with a circumference of 1,100 meters and with magnetic rigidities of 100 Tm. A possible upgrade option SIS300 can be placed in the same tunnel in order to reach higher energies.

The research program devoted to the exploration of compressed baryonic matter will start with primary beams from the SIS100 (protons with the kinetic energy up to 29 GeV, gold ions with up to 11 AGeV, light nuclei with $Z/A = 1/2$ up to 14 AGeV). The layout of the existing GSI facility and the planned FAIR accelerator complex is presented in fig. 1.4.

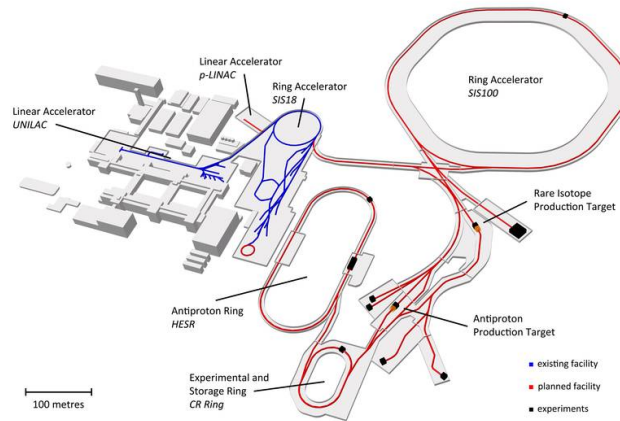


Figure 1.4: Layout of the FAIR: the existing GSI part in *blue* and the planned FAIR part in *red* [20].

1.3 THE COMPRESSED BARYONIC MATTER EXPERIMENT

Compressed Baryonic Matter (CBM) is one of the four scientific pillars of FAIR. The goal of the CBM experiment is investigation of the phase diagram of strongly interacting matter (fig. 1.1) in the region of high net baryon densities and moderate temperatures employing high-energy nucleus-nucleus collisions. The CBM experimental setup is a fixed-target forward spectrometer. It is currently being developed by the international collaboration including institutions in Germany, Russia, India, Romania, Poland and further countries. CBM will start its operation in 2024 with the beam from the SIS100 synchrotron.

CBM has an extensive physics program [21, 34]. Many of the important observables are rare diagnostic probes carrying the information of the dense stage of the fireball evolution. To collect sufficient statistics, an interaction rate up to 10 MHz is planned with a continuous (non-bunched) beam. Most of the observables have complex trigger topologies. This requires free data streaming from the detectors, sending time-stamped detector measurements to a computing farm, where track reconstruction, event formation, and analysis will be performed on-line. The high interaction rates lead to a large raw data flow (1 TB/s estimated), which is impossible to store. Thus, fast algorithms for reconstruction and event selection will be performed in real time.

The CBM detector has been designed as a multipurpose device which will be capable to register hadrons, electrons and muons in proton-nucleus and nucleus-nucleus collisions over the full FAIR beam energy range (see section 1.2 for the details). The CBM detector system has an angular acceptance between 2.5° and 25° to cover mid-rapidity and the forward rapidity hemisphere for symmetric collision systems over the FAIR energy range. The CBM setup comprises the following elements (see fig. 1.5):

- a dipole magnet to enable momentum measurements;
- a Micro Vertex Detector (MVD) to measure short-lived decay vertices and low-momentum particles;
- a Silicon Tracking System (STS) to provide tracking of charged particles and to measure their momentum;
- a Time-of-Flight (TOF) wall to identify hadrons;
- a Ring Imaging Cherenkov detector (RICH) to provide electron/pion identification;
- a Transition Radiation Detector (TRD) to suppress pions and to support track reconstruction;
- a Muon Chamber (MUCH) for muon identification and track reconstruction;
- an Electromagnetic Calorimeter (ECAL) for photon energy measurement;
- a Projectile Spectator Detector (PSD) for the collision centrality and event plane determination;
- a First-Level-Event-Selection (FLES) system to provide online event recon-

struction and selection.

The CBM setup may be used in two operation modes. One version is optimised for the detection of electrons and hadrons, another one is laid out for muon detection. In the first configuration, all the subsystems apart from MUCH will be involved. In the muon configuration, the RICH detector is replaced by MUCH and ECAL is removed.

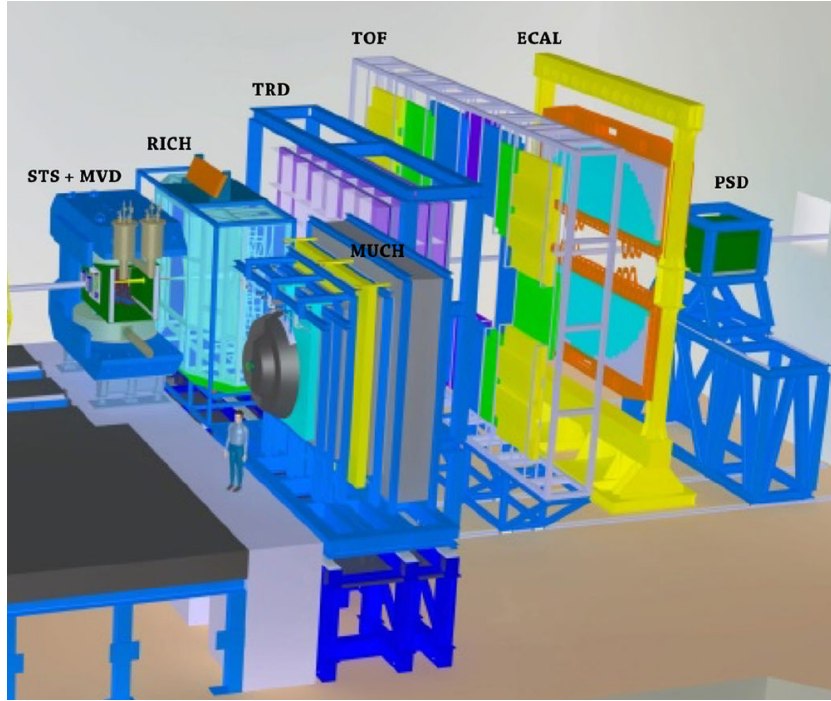


Figure 1.5: The CBM setup in the electron-hadron configuration. The MUCH for the muon configuration is shown in parking position [36].

DIPOLE MAGNET. The superconducting dipole magnet provides a vertical magnetic field with a field integral of 1 Tm from the interaction point to approximately 1 m downstream the target [37]. The tracking detectors, the MVD and the STS, in the thermal enclosure will be placed inside the magnet gap [38].

MICRO VERTEX DETECTOR. The main task of the MVD is to distinguish between primary vertex and displaced vertices, for example, to reconstruct decays of charmed hadrons: D-mesons or Λ_c baryons. This task requires a high resolution along the position vector $\approx 70 \mu\text{m}$, which turns to $5 \mu\text{m}$ spatial resolution [39] and low material budget. The MVD is located directly behind the target (5 – 20 cm downstream) in the dipole magnet. The MVD is placed in vacuum thus it is able to reconstruct low-momentum tracks that helps to reject background for di-electrons [39]. At least

4 interaction points must be registered in order to reconstruct a track; the MVD fits this minimal requirement with 4 detector layers. The requirements of high spatial resolution, low material budget and high radiation tolerance are fulfilled with CMOS Monolithic Active Pixel Sensors with fine pixel size of several dozens of μm [40, 41]. The first station has material budget of about $0.3\% X_0$. Being operated in the target chamber vacuum, the sensors need to be cooled, with the total anticipated power of 300 W [39]. This is possible by integrating the sensors on a highly heat-conductive support structure made from poly-crystalline CVD diamond carriers (first two stations) and sheets of Thermal Pyrolytic Graphite (last two stations). Both materials provide mechanical stability and low material budget. Due to the limited readout speed, the MVD will participate only in data taking with the interaction rate up to 10^5 Hz [41].

SILICON TRACKING SYSTEM. The STS is placed behind the MVD, outside the vacuum chamber, in the magnetic field. The STS is a key detector of the CBM setup providing charged particle tracking; the detailed description of its design can be found in section 1.4.

RING IMAGING CHERENKOV DETECTOR. The RICH is placed outside the magnetic field downstream the STS [42] in case of the electron-hadron configuration of the CBM setup. This detector is dedicated to particle identification via Cherenkov radiation. It allows separating electrons from pions up to $8 \text{ GeV}/c$ [43] with a pion suppression factor above 300 and electron identification efficiency above 85% [41]. Gas constituents and its pressure are chosen to cover the largest possible momentum range: CO_2 radiator at 2 mbar overpressure [43].

The focusing mirror is divided into two halves above and below the beam pipe, each made of about 40 individual spherical mirror tiles. Each half of the photodetector planes is split into two wings consisting of about 250 Hamamatsu H12700 Multianode Photomultiplier Tubes (MAPMT). The pixel size of these MAPMTs results in an uncertainty of the Cherenkov angle comparable or smaller than those expected from other sources such as multiple scattering, bending in the magnetic stray field, surface inhomogeneity of the mirror or dispersion [44]. There are following main challenges constraining the RICH design:

- high interaction rate and charged particle flux require gas with low fluorescence;
- magnetic field distortion of the PMTs performance: additional shield is required between STS and RICH;
- limited space for the radiator: thickness of 1.7 m was chosen;
- low material budget: low-mass support structures are involved.

MUON CHAMBERS. In the muon configuration of CBM, the RICH is replaced with the MUCH. It is experimentally challenging to identify low-momentum muons

in heavy ion collisions due to the high particle multiplicity [45]. The MUCH is located downstream the STS and consists of several layers of hadron absorber and detector planes. In order to reduce number of mesons decaying into muons, the absorber/detector system has to be as compact as possible. The MUCH geometrical detector acceptance is from 5.6° to 25° : the lower limit is given by the beam pipe, and the upper limit by the dipole magnet [46]. The MUCH will be operated in different setup configurations by varying the positions of the absorber-detector combinations. The detector planes of MUCH are based on the Gas Electron Multiplier (GEM) technology.

TRANSITION RADIATION DETECTOR. The TRD is a particle identification detector complementary to the RICH [41]. The TRD identifies electrons above momenta of $1 \text{ GeV}/c$ [41] with a pion suppression factor $10 - 20$ and an electron efficiency of 90% . Its performance is driven by the requirement to detect dielectron pairs with invariant masses between ϕ and J/ψ masses ($1 - 3 \text{ GeV}$). The TRD is also involved in the measurements of fragments and hyper nuclei. Additionally, the TRD makes tracking between the RICH and the Time-of-Flight detector and is used as tracking station in the muon configuration of CBM, providing spatial resolution about $300 \mu\text{m}$. The current geometry of the TRD consists of one station with four detector layers. The design decision was made to build the TRD layers from Multi-Wire Proportional Counter detector in combination with an adequate radiator. The drift chamber is rather short in order to have smaller signal collection time: $3.5 + 3.5 \text{ mm}$ amplification area and 5 mm drift region allow to get signal from one charged particle track in timescale below $200 \mu\text{s}$.

TIME-OF-FLIGHT DETECTOR. The TOF is a hadron identification detector with the same angular coverage as the STS [47]. A full-system time resolution $> 80 \text{ ps}$ and an efficiency higher than 95% are required for the kaon to pion discrimination [48]. The Multi-gap Resistive Plate Chambers technology is considered as a good solution for TOF giving 60 ps time resolution at 98% efficiency [49]. The TOF wall is placed at 6 m downstream the target (for SIS100 energies) and is divided into four rate regions.

ELECTRO-MAGNETIC CALORIMETER. The main purpose of the ECAL is to identify electrons and photons and to provide measurements of their energy and position [50]. It is a “shashlik” type calorimeter consisting 140 layers of 1 mm lead and 1 mm scintillator with the cell size of $6 \times 6 \text{ cm}^2$, that results in total more than 4000 readout channels [51].

PROJECTILE SPECTATOR DETECTOR. The PSD provides independent estimation of the centrality and the reaction plane of the ion collisions based on forward rapidity

energy [41]. It is a compound calorimeter, involving lead plates as an absorber and plastic scintillator plates for the measurement of the energy deposited by hadronic showers. The PSD is placed at the distance of 8 m from the target and consists of 44 individual modules with the 6 cm hole in the center. The transverse size of the modules is $20 \times 20 \text{ cm}^2$; the total length of the detector is about 120 cm.

FIRST-LEVEL-EVENT-SELECTION. The CBM physics program requires high-statistics measurements, which leads to high interaction rate and high data rate. Assuming an archiving rate of 1 GByte/s and an event size of 10 kByte for a minimum bias Au+Au collision, a maximum interaction rate of 100 kHz can be accepted by a traditional data acquisition and storage architecture. Higher event rates require an online event selection algorithm, which rejects the background events at least by a factor of 100 before the data can be stored. The event selection system will run on a high-performance computer farm based on many-core CPUs and graphics card (GSI GreenIT cube). Track reconstruction is based on parallel track finding and fitting algorithms, implemented with the Cellular Automaton [52] and Kalman Filter [53] methods. The event selection system for some physics processes (for example, open charm production) will involve a software trigger.

1.4 THE SILICON TRACKING SYSTEM

The Silicon Tracking System (STS) is the core CBM detector [54]. Its main task is to reconstruct tracks of charged particles (with high efficiency $> 95\%$ for $p > 1 \text{ GeV}/c$) and to measure their momenta with high resolution ($\approx 1.5\%$ for $p > 1 \text{ GeV}/c$). Such limitations are required for successfully reconstruction of particles of the physics interest. To fulfil this requirement, the STS has to provide high hit reconstruction efficiency (close to 100%) and high spatial resolution ($\lesssim 20 \mu\text{m}$), which leads to the fine granularity of the detector. The presence of a strong magnetic field is needed in order to measure the particle momentum; the curvature of its trajectory is inversely proportional to the momentum. The necessity of the high momentum resolution requires a low material budget.

In order to match the CBM physic program, the STS has to cope with high hit rates (up to 700 charged particles per central Au+Au event at the highest CBM interaction rate 10^7 Hz) without a hardware trigger (see section 1.3). Sensors with sufficient granularity together with fast free-streaming electronics are being developed to fit the requirement mentioned above.

The STS design allows to fulfil all the constrains mentioned above. There are 8 detector stations (sensor layers) placed between 30 cm and 100 cm downstream the target in the 1 T dipole magnetic field. They cover polar angles from 2.5° to 25° (see fig. 1.6). Total material budget lays within $1.3\% X_0$ per station including both routing cables from the sensor to electronics and the support structure (see fig. 1.7).

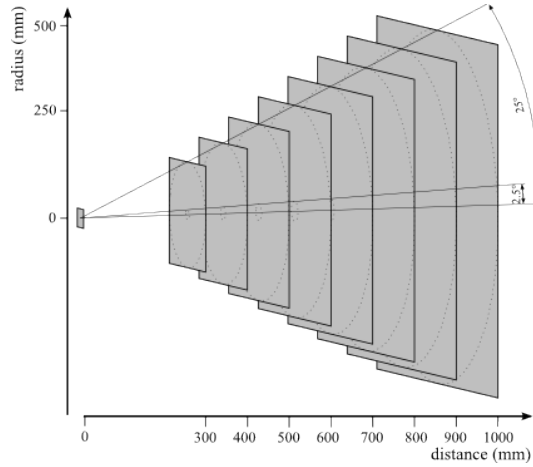


Figure 1.6: Concept of the STS. Tracking stations are placed between 30 cm and 100 cm with 10 cm gap between closest neighbours. Radii of the stations are schematically indicated [54].

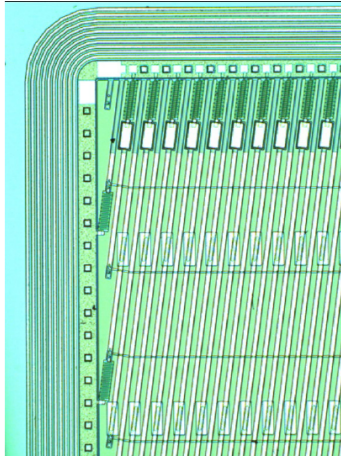


Figure 1.8: Sensor (prototype CBM03) corner from p-side under microscope. Inclined white lines are the p-strips, four thin horizontal lines — the second metal layer [54].

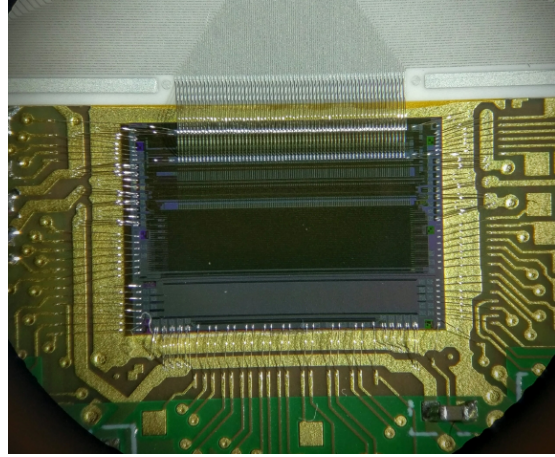


Figure 1.9: STS-XYTER chip in PCB (Printed Circuit Board) under microscope [55].

The sensors are double-sided microstrip silicon sensors with $58\mu\text{m}$ strip pitch and about $300\mu\text{m}$ thickness made from n-type high-resistive silicon. There are 4 main sensor sizes involved: 6.2 cm wide and 2.2, 4.2, 6.2, 12.2 cm long. Each one has 1024 strips per side. One sensor side is read-out by 8 ASICs (Application-Specific Integrated Circuit). Smaller sensors with shorter strips will be placed in the inner region of the stations close to the beam pipe, where the hit density is high. This will reduce the hit rate per sensor to ease the hit reconstruction. A few narrower sensors will cover the space around the beam pipe. All sensors overlap in order to

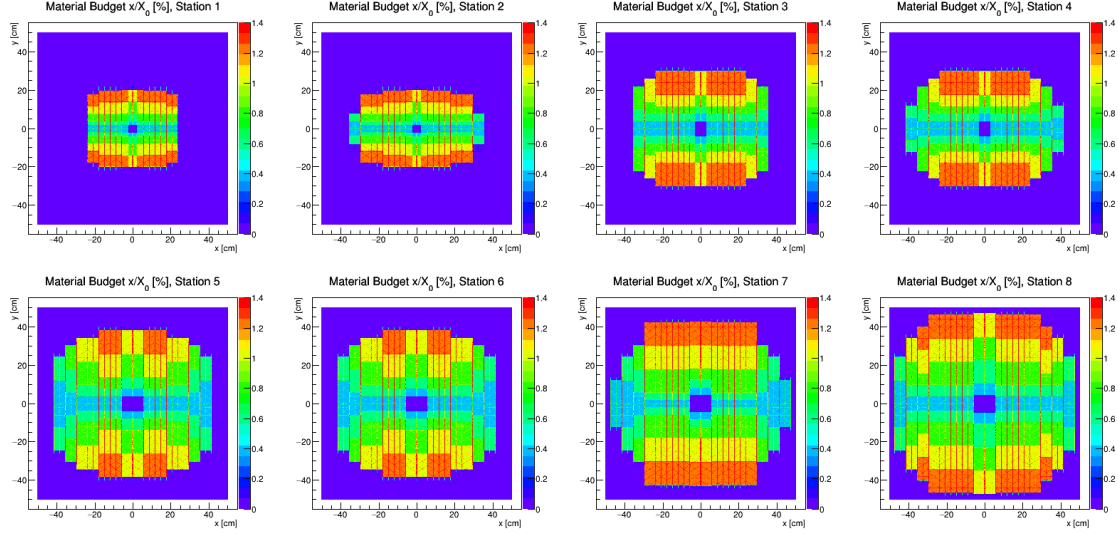


Figure 1.7: Material budget map for each station including all support structures and routing cables.

minimise dead space in between.

Measuring two coordinates simultaneously with the double-sided sensors allows minimising the material budget. Strips on the n-side are vertical and those on the p-side are tilted by 7.5° with respect to the n-side strips. The angle was chosen in order to suppress the number of fake hits (see section 3.2) yet keeping the spatial resolution sufficiently high: $10 - 20 \mu\text{m}$ in the bending plane and $100 - 200 \mu\text{m}$ in the perpendicular plane. The second metal layer connects the short strips (near the sensor edge) on the p-side (schematically shown in fig. 3.2). This feature allows to preserve the constant number of 1024 strips per side but complicates the hit position reconstruction (see section 3.2). The chosen topology allows to read the sensors out from one edge in the vertical direction. It allows to connect sensors with electronics from only one side and place the electronic out of the detector acceptance.

The radiation tolerance is a vital quality condition of the silicon microstrip sensors, regarding the severe radiation conditions in the STS environment. The radiation hardness was confirmed up to twice the expected lifetime fluence [40, 56, 57]. The lifetime fluence for the STS operating under the SIS300 conditions is 10^{14} cm^{-2} in 1 MeV neutron equivalent for the innermost sensors. Charge collection efficiency drops only by 15 – 20 % after irradiation to twice this level.

The self-triggering fast readout electronics is placed outside of the acceptance to minimise the material budget inside. The electronics is based on the custom designed ASIC — STS-XYTER (STS X and Y coordinate, Time and Energy Readout chip) [58]. Its technological predecessor, n-XYTER (neutron-X-Y-Time-Energy Readout) [59], was used when STS-XYTER was at the design stage. STS-XYTER can cope with hit rates up to 47 Mhit/s per ASIC, which converts to average maximum rate of 0.37 Mhit/s per channel. This is much below the maximum hit rate of

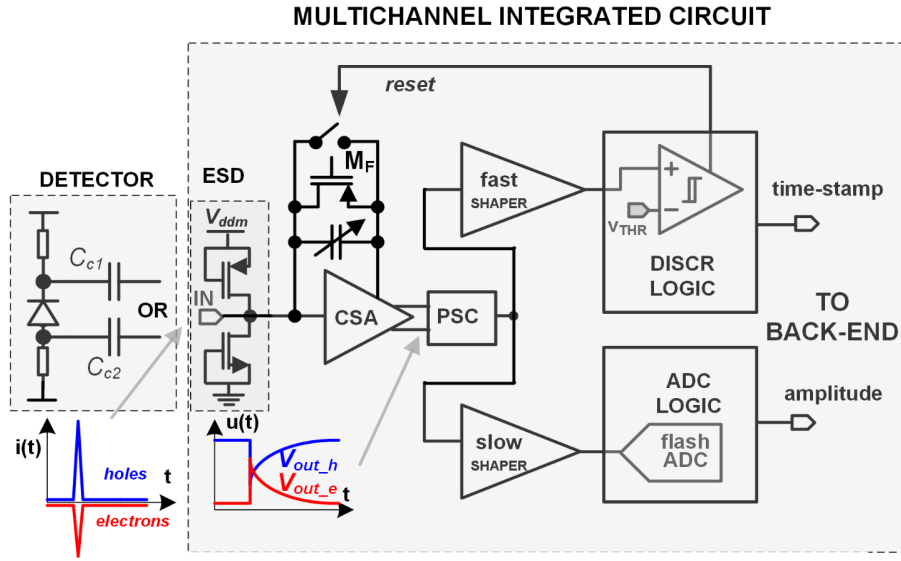


Figure 1.10: Simplified block diagram of the STS-XYTER ASIC. CSA — Charge Sensitive Amplifier, PSC — Polarity Selection Circuit, DISCR — discriminator, ADC — Analogue-to-Digital Converter [55]. The chip architecture features fast and slow branch with double discriminator logic for low noise performance.

0.12 Mhit/s that corresponds to hit density 10 MHz/cm² for the innermost sensors. Each of 128 channels of the STS-XYTER chip has two pulse shaping amplifiers to achieve a good amplitude resolution and a low noise rate in combination with a sufficient time resolution:

- the slow shaper with 80 ns shaping time provides amplitude information. It has a 5-bit continuous-time flash Analogue to Digital Converter (ADC), which gives precision of amplitude measurements $\approx 3\%$ of the ADC dynamic range;
- the fast shaper with 30 ns shaping time provides time information with time stamp 3.125 ns.

The dynamic range of STS-XYTER is 15 fC that is roughly 4 times more than the most probable charge created in 300 μm silicon by a Minimum Ionising Particle (MIP).

The readout electronics is connected to the sensors with ultra-thin micro-cables [54]. They are covered with the grounded shielding layer in order to reduce the noise level. For the signal transmission, two layers of micro-cable with the aluminium strips with a pitch of 116 μm are used. They are separated with a meshed spacer in order to reduce the parasitic inter-layer capacitance. The supporting material for the aluminium strips is 20 μm polyimide.

The sensors are mounted onto the lightweight space frames with end supports; these structures are called “ladders” [54]. The frames are made from carbon fiber,

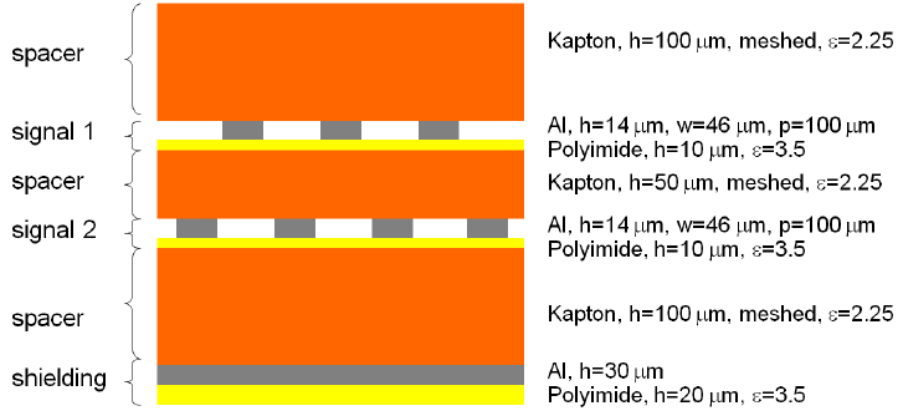


Figure 1.11: Cross section of a micro-cable that reads one side of a sensor [54].

which provides mechanical stability keeping the low mass in the physical acceptance [41]. The contribution of the material of supporting structures is found to be small comparing to the impact of the sensors and the micro-cables.

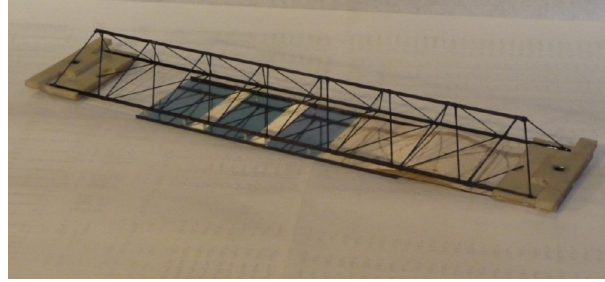


Figure 1.12: Mechanical prototype of 3 mock-up sensors and corresponding micro-cables mounted onto a ladder's carbon fiber support [54].

The cooling system for the STS has two requirements:

- keep the sensors at the temperature not higher than -5°C , to reduce shot noise level due to leakage current for the irradiated sensors: the innermost sensors around the beam pipe will dissipate in operation around $1\text{ mW}/\text{cm}^2$ after accumulation of the lifetime dose;
- remove the heat dissipated by the front-end electronics boards (FEB): each FEB produces about 20 W , resulting in the power dissipation of about $40 - 45\text{ kW}$ for the total system.

The heat transfer inside the acceptance should be realised with a minimal amount of material. This induces usage of gas convection in the STS volume. At the same time, the humidity must be kept low to avoid condensation on the sensors.

For the cooling of electronics, evaporative heat transfer based on CO_2 was chosen, because of its high volumetric heat transfer coefficient [41]. The cooling blocks will be tightly connected to the boxes holding the front-end electronics at the top side and bottom side of the STS [41].

1.5 MOTIVATION FOR RELIABLE DETECTOR RESPONSE MODEL

The core detector of the CBM experiment is the Silicon Tracking System (STS) [54]. Its main task is to reconstruct tracks with good momentum determination and high efficiency. To exploit the full precision performance of the STS, realistic simulations and efficient reconstruction algorithms are required. Precise modelling of detectors in simulations is the key to understanding their performance, which, in turn, is a prerequisite for the proper design choice and, later, for the achievement of valid physics results.

A realistic detector response model developed for the STS is presented in this work. It includes all relevant physical processes occurring in the silicon detector. To utilise the full capacities of the detector, a proper hit reconstruction algorithm is required. I focus on both the accurate determination of the centre of a cluster (which is a set of several activated strips) and the corresponding measurement uncertainty. A proper estimate of the error is important for track reconstruction, particularly for the accurate estimation of the track parameters and rejection of invalid track candidates.

1.6 SILICON DETECTORS

Semiconductor detectors are widely used in High Energy and Particle Physics. A semiconductor detector can be thought of as an ionisation chamber. However, it has the following advantages [60]:

- low “ionisation” energy of few eV;
- large energy loss per length of the ionising particle due to high mass density;
- good energy resolution;
- radiation tolerance;
- rapid charge collection due to high mobilities of the charge carriers.

Mostly, semiconductor detectors are made from germanium, diamond, or silicon. Diamond detectors are radiation hard and have a large band gap of 5.5 eV [60] that leads to low leakage current. However, these detectors are expensive. Germanium detectors have a small band gap of 0.66 eV [60] that requires cooling to liquid nitrogen temperatures. Silicon detectors have a band gap of 1.2 eV and can be operated at room temperature. The average energy to create an electron-hole pair is 3.6 eV [60]. Conduction in silicon without doping (intrinsic semiconductor) takes place when electrons from the valence band are thermally excited to the conductive band. The electrons in the conductive band and the holes in the valence

band conduct electrically under the influence of an electric field. The drift velocities for electrons (e) and holes (h) differ and depend on the applied electric field E [60]:

$$v_e = \mu_e E, \quad v_h = \mu_h E, \quad (1.1)$$

where $\mu_{e/h}$ is the mobility of electrons/holes.

Electrical properties of silicon are mainly defined by doping. For example, the resistivity (the inverse conductivity) depends on the doping concentration as:

$$\rho = \frac{1}{e(\mu_h N_h + \mu_e N_e)}, \quad (1.2)$$

where $N_{e/h}$ is the free electron/hole concentration, and e the elementary charge. In n-type silicon (doped with the element with $Z+1$ charge number, where Z is the atomic number of Silicon), the electrons are the majority carriers, the holes have relatively low concentration. Thus, the resistivity is dominated by the electron concentration:

$$\rho = \frac{1}{e\mu_e N_e}. \quad (1.3)$$

In p-type silicon, the situation is the opposite.

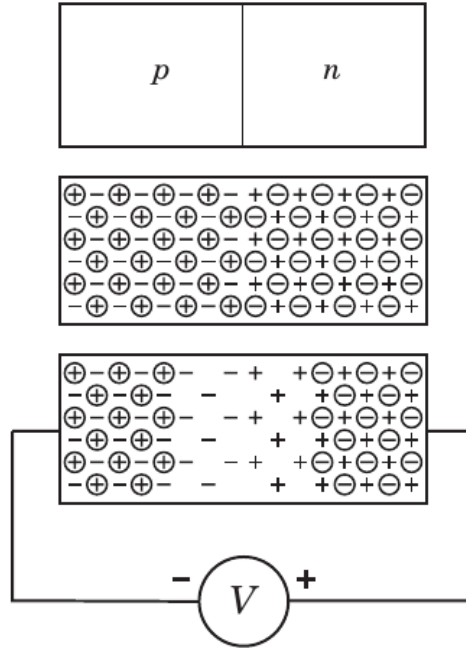


Figure 1.13: P-n junction formed by regions of p- and n-types joined together (*top*). The mobile electrons and holes are shown with *circles*. If an external reverse bias potential is applied (*bottom*), the mobile charges are drawn away from the junction [61].

Joining p-type silicon with n-type silicon creates a diode with a p-n junction formed at the bound. The strong gradient of positive and negative charges causes diffusion of electrons into the p-type region and holes — into the n-type region. This creates an electric field that counteracts the diffusion and an equilibrium is reached. This potential is about 0.6 V for Silicon and is called the diffusion potential or the built-in potential V_{bi} . If the reverse bias voltage is applied (positive polarity on the n-side, and negative on the p-side), the majority carriers in each region of the p-n diode are drawn away from the junction [61]. Thus, this region is depleted of mobile charges (see fig. 1.13).

The reverse bias voltage V_b yields the depletion width [61]

$$w_d = \sqrt{\frac{2\varepsilon(V_b + V_{bi})}{eN}}, \quad (1.4)$$

where N is the dopant concentration, and ε the dielectric constant. If w_d extends to the whole diode thickness, the diode is fully depleted. The full depletion voltage, ideally, removes all the charge carriers from the junction volume, and no current can flow. However, due to thermal excitation, electrons can cross the band gap yielding so-called “dark current” I_R . It depends on temperature T as

$$I_R \propto T^2 \exp\left(-\frac{E_g}{2kT}\right), \quad (1.5)$$

where k is the Boltzmann constant, and E_g the band gap energy.

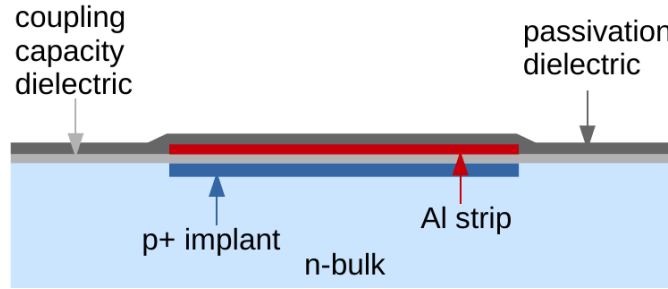


Figure 1.14: Schematic view of the sensor layers on the p-side. N-side looks similarly, only p^+ -implants are replaced by n^+ -implants.

When a particle crosses the reverse-biased sensor, electron-hole pairs are created along the particle track and drift in opposite directions under influence of the electric field. While drifting, the charge carriers induce a current pulse on the electrodes. The signal induction finishes when all the electrons and holes reach the corresponding electrodes. This provides the information about the deposited energy by the incident particle. If the electrodes of the diode are segmented, this can provide spatial information.

The STS silicon sensors have n-type bulk, p^+ -implants on the p-side, and n^+ -implants on the n-side. The implants of both sides are covered with a thin layer of dielectric (SiO_2 , Si_3N_4 , or a stack of both), and each implant has a metallisation layer on top, which duplicates the shape of the corresponding implant. Thus, the metal strips are capacitively coupled to the implant and connected to the readout electronics. The schematic layout of the p-side is shown in fig. 1.14. Strips on the opposite sides are oriented under a stereo angle, providing 2D information about the particle hit.

2

Detector response model

An accurate detector model in simulations is a prerequisite for proper design and correct reconstruction of physics signals. The previous available version of the detector simulation for the STS [62, p.7] does not take into account any charge sharing effects and has some deviation from the experimental data (especially for perpendicular tracks section 4.3). This issue clearly demonstrates that the detector response model needs to be improved.

The structure of this chapter is the following:

- In section 2.1, the simulation of the detector response, subdivided into main processes, is described. Methods available in literature are mentioned briefly for each process.
- Section 2.2 presents an overview of detector response models, which are used by other experiments. A particular implementation for the realistic model, which was chosen by the STS group, is described here. The influence of different physical processes on the STS measured quantities, such as cluster size, spatial resolution, etc., is presented.
- Section 2.3 compares the realistic digitizer for the STS with the former model.

2.1 SIMULATION OF SILICON DETECTORS

Simulations of the silicon strip detector response can be divided into the following modelling steps:

1. passage of an incident particle through the sensor medium: the energy loss and the creation of charge carriers (electron and holes);
2. transport of charge carriers within the sensor volume:
 - movement of the charge carriers to the readout plane in the electric field, which can have a complex geometry in a general case;
 - diffusion of the charge carriers during the drift;
 - affection on the particle movement by the magnetic field;
3. charge redistribution over readout channels due to the interstrip capacitance;
4. signal integration in the readout electronics;
5. electronic noise and threshold.

All these effects are subsequently addressed in the following sections.

2.1.1 ENERGY LOSS SIMULATION

An incident charged particle electromagnetically interacts with the material of the sensor and loses its energy along the track. There are several ways to estimate the distribution of the energy loss. Some of them are listed below from the simplest to more comprehensive:

1. **uniform energy loss:** simulate the total energy loss throughout whole sensor thickness with some distribution (particularly, Landau distribution) and distribute energy losses uniformly along the incident particle trajectory within the sensor volume [63–66];
2. **non-uniform energy loss:** divide the trajectory into steps and
 - (a) simulate energy losses in each of them using some distribution:
 - i. the Landau distribution. It is, in general, not valid for a layer as thin as several $100\ \mu\text{m}$ even for as energetic electrons as $1\ \text{GeV}$ (see [67] and fig. 2.1);
 - ii. the Landau distribution convoluted with the Gaussian, the width parameter of the Gaussian distribution is tuned in a way to reproduce the correct value of the most probable energy loss for the total thickness of the sensor (see [68], where the step size is $10\ \mu\text{m}$);
 - iii. the standard GEANT routine `GLANDZ` [67]. It determines proper distribution for given step size and incident particle characteristics [69, 70];

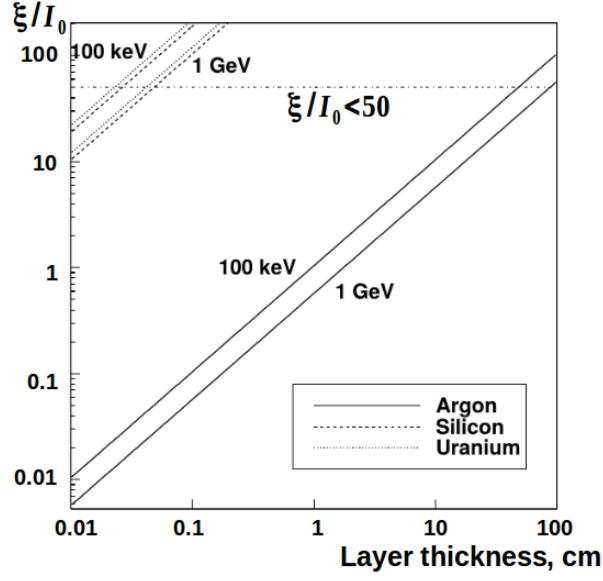


Figure 2.1: The variable ξ/I_0 for electrons with kinetic energy 100 keV and 1 GeV in different materials. This variable can be used to measure the validity of the Landau theory. The contribution of the collisions with low energy transfer which can be estimated with the relation ξ/I_0 . Landau theory assumes that the number of these collisions is high, and consequently, it has a restriction $\xi/I_0 \gg 1$. The ξ/I_0 ratio depends on the type and energy of the particle, Z , A , and the ionisation potential of the material, and the layer thickness [67].

- iv. any other (semi-)empirical model suited for thin layers, for example the Urban method [67, 71].
- (b) simulate a number of the incident particle collisions in each step according to the Poisson law and energy losses in each interaction involving differential and total collision cross sections. The evaluated energy loss is later associated to the current step of the trajectory. For example, in [72] and [73] the step size of $1 \mu\text{m}$ is used. The total energy loss of 2 GeV protons in such small layer of silicon is shown in fig. 2.2.
- 3. **full Monte Carlo simulation:** the energy loss is estimated based on a detailed numerical modelling of the incident particle motion and the accompanying ionisation process [74]. Thus, the momentum and the initial coordinates of each charge carrier is modelled.

2.1.2 TRANSPORT OF ELECTRON-HOLE PAIRS

After an electron-hole (e-h) pair has been created, the charge carriers start to drift in the electromagnetic field and to move due to the thermal diffusion.

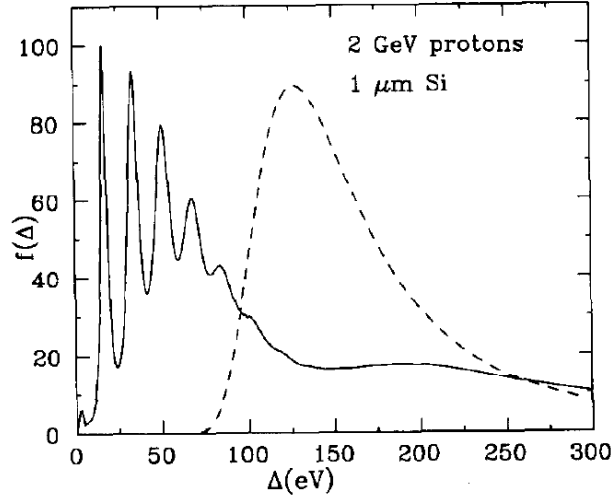


Figure 2.2: The energy loss spectrum for 2 GeV protons traversing a Si absorber of thickness $1\ \mu\text{m}$ as calculated in [72] (solid line). The function $f(\Delta)$ extends to a maximum value $\Delta_M = 9\ \text{MeV}$. The separate peaks at 17, 34, 51... eV correspond to 1, 2, 3 ... plasmon excitations. The Landau function for such a absorber is shown as dashed line.

2.1.2.1 DESCRIPTION OF THE ELECTRIC FIELD

Electric field inside the sensor has a complex shape. There are two approaches to model the motion of e-h pairs in the electric field:

1. To calculate a detailed map of the electric potential (taking into account strips, metallisation layers, doping, etc.) and then to solve the equation of motion for each hole and electron $\vec{v} = \mu \vec{E}$, where μ denotes the mobility of the charge carrier [64–66, 74, 75]. The first order differential equation of motion is solved numerically with Runge-Kutta method. At each time step δt , the step

$$\delta \vec{r} = \vec{r}(t + \delta t) - \vec{r}(t) \quad (2.1)$$

is evaluated.

2. To approximate the electric field with an analytic expression for a field in a planar abrupt p-n junction in overdepleted regime [61, 63, 66, 68–70] (fig. 2.3):

$$|E(z)| = \frac{V_{\text{bias}} + V_{\text{dep}}}{d} - \frac{2z}{d^2} V_{\text{dep}}, \quad (2.2)$$

where d is the thickness of the sensor, V_{dep} the depletion voltage, and V_{bias} the bias voltage. Then the produced charge is projected on the readout plane.

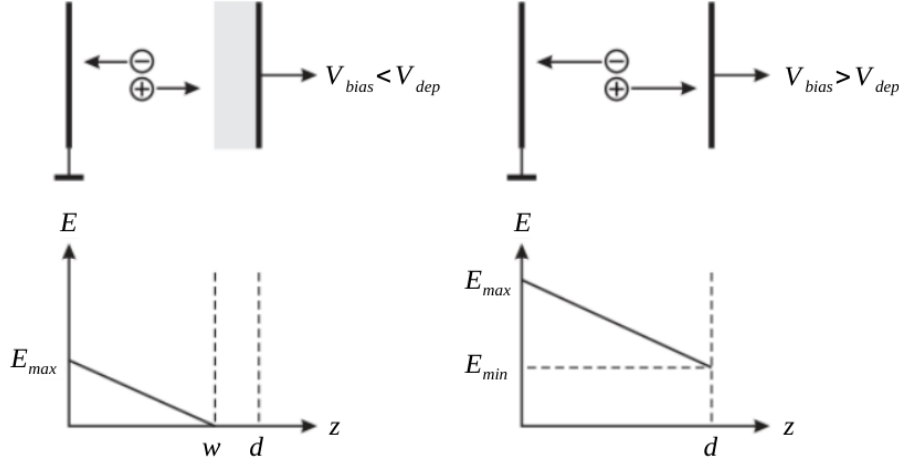


Figure 2.3: Distribution of the electric field for $V_{\text{bias}} < V_{\text{dep}}$ (left) and $V_{\text{bias}} > V_{\text{dep}}$ (right) (taken from [61] and modified).

The current induced at time t on the k th electrode by a moving charge carrier is given by the Shockley-Ramo theorem:

$$i_k(t) = -q\vec{v} \cdot \vec{E}_{wk}, \quad (2.3)$$

where q is the charge of the carrier, \vec{v} its velocity, and \vec{E}_{wk} the weighting field associated to the k th electrode, which is determined by setting the k th electrode to a unit potential and all others — to zero potential [64–66, 74, 75] (fig. 2.4).

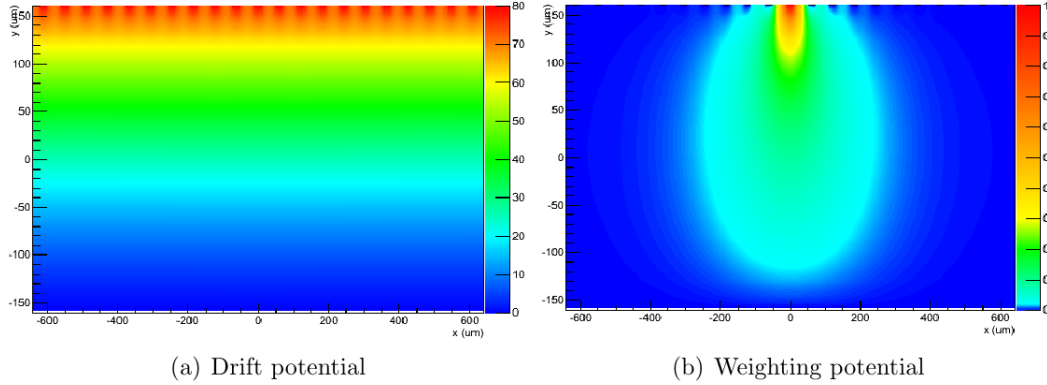


Figure 2.4: Drift (left) and weighting (right) potentials of a two-dimensional strip detector with: the lateral extent of $1000 \mu\text{m}$, the thickness of $300 \mu\text{m}$, the strip pitch of $50 \mu\text{m}$ and the strip width of $20 \mu\text{m}$ [64].

If the integration time of a pre-amplifier is larger than the collection time of all the charge carriers, the integrated charge is the full deposited charge. In this case, the measured electrode gets the current induced only by those carriers, which moving terminates on this very electrode [61]. The other electrodes get zero net current.

2.1.2.2 DIFFUSION

There are several methods to model diffusion from the most detailed to the simplest ones:

1. Additionally to the drift in electric field, a small shift of each charge carrier in random direction due to diffusion can be modelled. There are two methods to evaluate it:

- (a) following [64, 76], the velocity of charge carrier is assumed to obey the Boltzmann distribution:

$$P(v) = \frac{-m_{\text{eff}}v}{k_{\text{b}}T} \exp\left(\frac{-m_{\text{eff}}v^2}{2k_{\text{b}}T}\right) \quad (2.4)$$

with the mean thermal velocity:

$$v = \left(\frac{3k_{\text{b}}T}{m_{\text{eff}}}\right)^{1/2},$$

where k_{b} is Boltzmann's constant, T the temperature, m_{eff} the effective mass. To get v , a uniformly distributed random number ξ is converted to random number distributed according eq. 2.4:

$$v_{\text{abs}} = \left(\frac{2k_{\text{b}}T}{m_{\text{eff}}} \ln \left| \frac{1}{1-\xi} \right| \right)^{1/2}.$$

A random direction for the movement is generated by a random unit vector.

- (b) The random walk can be described with the Gaussian law [74]:

$$\frac{dN}{N} = \frac{1}{\sqrt{4\pi Dt}} \exp\left(-\frac{r^2}{4Dt}\right) dr, \quad (2.5)$$

where dN/N is the fraction of particles in the line element dr at distance r from the production point and after time t . The standard deviation is given by:

$$\sigma = \sqrt{2Dt}, \quad D = \frac{kT}{e}\mu, \quad (2.6)$$

D is called the diffusion coefficient, T the temperature, e the elementary charge, and μ the mobility of the charge carrier. The diffusion effect can be taken into account during the solution of the equation of motion: the step $\delta\vec{r}$ from eq. (2.1) can be decomposed as: $\delta\vec{r} = \delta\vec{r}_E + \delta\vec{r}_D$, where $\delta\vec{r}_E$ is the step due to the electric field (that is evaluated with the Runge-Kutta

method) and $\delta\vec{r}_D$ is induced by the diffusion. The $\delta\vec{r}_D$ term is simulated with 3 numbers (σ_i) that represent the motion into 3 directions:

$$\delta\vec{r}_D = \begin{pmatrix} \cos\phi \cos\theta & -\sin\phi & -\cos\phi \sin\theta \\ \sin\phi \cos\theta & \cos\phi & -\sin\phi \sin\theta \\ \sin\theta & 0 & \cos\theta \end{pmatrix} \times \begin{pmatrix} \sigma_1 \\ \sigma_2 \\ \sigma_3 \end{pmatrix},$$

where σ_i are three random values distributed normally around zero with the width parameter given by eq. (2.6). Here, θ and ϕ are the angles of the direction of motion with respect to the electric field lines.

The additional random velocity calculated with the method from [64] or from [74] is used during induced current evaluation in eq. (2.3).

2. If the integration time is larger than the collection time, one can simplify the estimation of diffusion influence to the charge collection. Gaussian distribution (2.5) can be used to estimate the cloud increasing size during the whole drift time. In the electric field given by (2.2), the drift time for a charge carrier can be estimated as [61]

$$t_e = \frac{d^2}{2\mu_e V_{\text{dep}}} \ln \left(\frac{V_{\text{bias}} + V_{\text{dep}}}{V_{\text{bias}} - V_{\text{dep}}} \left(1 - \frac{2z}{d} \frac{V_{\text{dep}}}{V_{\text{bias}} + V_{\text{dep}}} \right) \right), \quad (2.7)$$

$$t_h = -\frac{d^2}{2\mu_h V_{\text{dep}}} \ln \left(1 - \frac{2z}{d} \frac{V_{\text{dep}}}{V_{\text{bias}} + V_{\text{dep}}} \right), \quad (2.8)$$

where V_{depl} is the depletion voltage, V_{bias} the bias voltage, μ the mobility, d the sensor thickness, z the initial position of the charge carrier along the axis perpendicular to the sensor plane. Since the collection time $t \propto 1/\mu$, the resulting σ in (2.6) doesn't depend on the type of the charge carrier. A fraction of the charge package collected in strip i is

$$f_i = \frac{1}{\sqrt{2\pi}\sigma} \int_{\Delta_i - p/2}^{\Delta_i + p/2} \exp\left(-\frac{x^2}{2\sigma^2}\right) dx,$$

where Δ_i is a distance from the charge package to the strip centre, p the strip pitch [70].

3. The simplest method to model the diffusion is to assign the Gaussian profile to the charge in the direction perpendicular to the incident particle track. The Gaussian width corresponds to the characteristic range of charge diffusion while the charge is collected by electrodes ($2\mu\text{m}$ in [65]). The evolution of the diffusion during the collection time is ignored.

2.1.2.3 MAGNETIC FIELD

In presence of the magnetic field orthogonal to the electric field in the sensor, the charge carriers do not longer drift straight to the electrodes but are deflected due to the Lorentz force (see fig. 2.5, [63, 64, 75]). The direction of the movement is then changed by the Lorentz angle θ_L . Since the velocities of electrons and holes are different, the Lorentz forces acting on them will also differ:

$$\begin{aligned}\tan \theta_{L,i} &= \frac{\Delta x_i}{d} = \mu_H^i B = \mu^i r_H B, \\ \Delta x_i &= \mu^i(E, T) r_H B d.\end{aligned}\tag{2.9}$$

Here, μ_H is the Hall mobility, μ the drift mobility, r_H the Hall scattering factor, Δx the Lorentz shift, i denotes the carrier type (e – electrons or h – holes) [77].

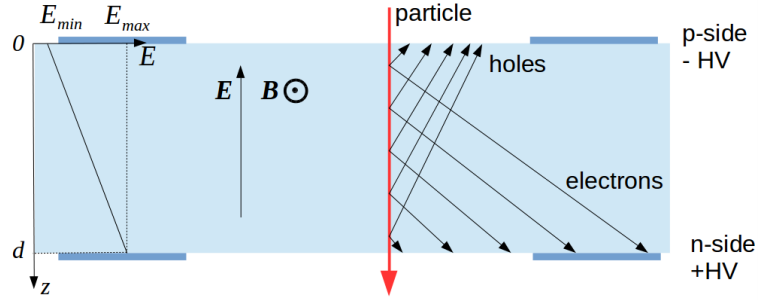


Figure 2.5: An illustration of the Lorentz shift. Electrons and holes travel at different angles. This angle also depends on the electric field.

The drift mobility depends on the electric field and temperature

$$\mu = \mu_{\text{low}} \left(1 + \left(\frac{\mu_{\text{low}} E}{v_{\text{sat}}} \right)^\beta \right)^{-1/\beta},$$

where μ_{low} , β , and v_{sat} are temperature-dependent parameters and are different for electrons and holes (see [77]), the electric field E can be determined at current z -coordinate using eq. (2.2). Thus, the value of the Lorentz shift depends not only on the type of the charge carrier but also on the initial coordinate.

In order to take a magnetic field into account, the following approximations can be involved:

1. Solving the equation of motion of the charge carriers (2.1) one can include a shift at each step. In this case, a proper value of the electric field is taken into account at each step [65].
2. Calculate the mean electric field along the trajectory of each charge carrier and use this value to calculate the Lorentz shift.

3. Assume that the shift angle is the same for all charge carriers of one type and calculate the shift according to this angle [66].

2.1.3 CROSS-TALK EFFECT

Cross-talk is a redistribution of a signal among the strips due to the presence of the parasitic interstrip capacitance C_i . To estimate a fraction of the measured charge that is induced on a neighbouring strip due to the cross-talk, the following simplified relation can be used:

$$Q_{\text{neib strip}} = \frac{Q_{\text{strip}} C_i}{C_{\text{bulk}} + C_c + 2C_i}. \quad (2.10)$$

Here, Q_{strip} is the signal on the measured strip, $Q_{\text{neib strip}}$ the signal on one of its neighbour, C_c the coupling capacitance, C_{bulk} the bulk capacitance (see left part of fig. 2.6). If $C_{\text{bulk}} \ll C_i$, C_c , eq. (2.10) simplifies to

$$Q_{\text{neib strip}} = \frac{Q_{\text{strip}} C_i}{C_c + 2C_i}. \quad (2.11)$$

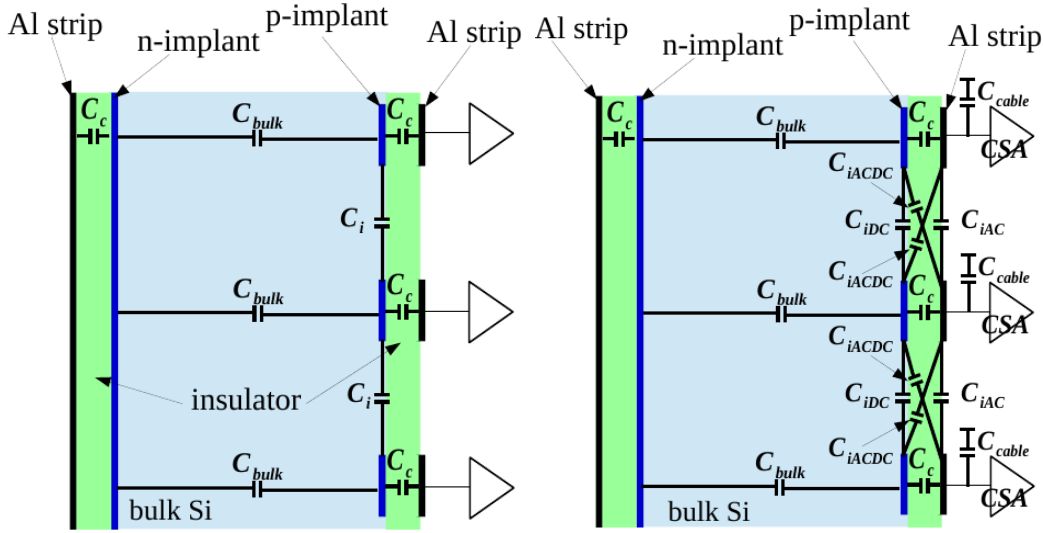


Figure 2.6: Double-sided silicon microstrip detector layout: simplified (*left*) and more detailed one (*right*). The schemes are not scaled properly.

A more sophisticated approach involves readout electronics and, if present, transmission lines that connect readout electronics with the sensors. It includes not only charge sharing between strips in a sensor (cross-talk) but also charge sharing between the sensor, the transmission lines, and the charge sensitive amplifier (see the right part of fig. 2.6). Because a particular configuration of the readout scheme and parameters of all the components play a role here, I will not give any general formulae but only describe our implementation later in section 2.2.2.3.

2.1.4 MODELLING OF THE RESPONSE OF THE READOUT ELECTRONICS

Free charge created in the sensor induces current on implants and the current is transferred to charge sensitive amplifier (CSA) through strips and transmission lines. Here, the readout electronics comes into play. If the integration time of the readout chip is smaller than the drift time of the charge carriers, the time profile of the signal should be taken into account. It can be estimated using the Shockley-Ramo theorem (2.3).

Here, I describe only the effects of the readout electronics assuming that all current is integrated in the CSA. In this sense, the simulation is time independent.

The main task of the readout chip is the amplification and the discretisation of the signal. However, the chip introduces its own noise. There are following main sources of the electronic noise:

- the leakage current through the silicon sensor — the shot noise;
- the thermal noise of the resistive structures (bias resistors, metal strips, transmission lines);
- the electronic noise of the amplifier.

Because different noise sources are assumed to be independent, the total noise (Equivalent Noise Charge) is

$$ENC_{\text{total}}^2 = ENC_{\text{shot}}^2 + ENC_{\text{thermal}}^2 + ENC_{\text{amplifier}}^2. \quad (2.12)$$

Each component can be estimated separately [61, 78] or one can measure the total noise of the system.

The noise is added to the signal in each fired readout channel. It is so called signal-correlated noise. In self-triggered systems, the noise rate, which is independent of signal, can be estimated with Rice formula [61].

After the noise simulation, the threshold is applied to the signal before the discretisation in self-triggered systems. The charge calibration is a procedure which allows later to convert ADC values to the units of charge (fC or ke). It is usually performed by giving a probe charge to the input of the CSA and measuring an output in ADC units. Alternatively, a relation between ADC units and charge can be calculated from a model. Particular simplistic method is to assume linear amplification and linear charge discretisation for a given dynamic range Q_{max} and number of ADC channels $nADC$:

$$q[ADC] = \frac{q[e]}{Q_{\text{max}}} nADC.$$

Since the calibration varies channel-to-channel, this effect can be added as an uncertainty to the calibration parameters.

In case of the triggerless running scenario, the time behaviour of the readout electronics is important. The time resolution defines the quality of a time-based cluster finder that involves information about the time difference between signals, which are assumed to originate from the same incident particle. The single-channel dead time restricts the hit rate. The signals, which come to the same readout channel one after another, can overlap in time. A bandwidth of the chip data stream also limits the hit rate.

2.2 IMPLEMENTATION

In the `cbmroot` framework, the digitizer is a set of the software elements dedicated for the simulation of the detector response. It covers a complete chain of the physical processes starting from the charge creation in a silicon sensor bulk to the digital signal as an output. Digitization is the last step in the STS simulation chain; previous stages of the simulation provide particles initiating from the interaction points and perform their interaction with the detector material. The digitizer involves the following input information: the entry and the escape coordinates of an incident particle in the sensor medium, its type and energy, and the time of the particle traversal. The digitizer gives digis as output. A digi is a signal characterised with the charge, the time of registration, and the sequential number of the corresponding readout channel. In this way, a digi from the digitizer is equivalent to a digi measured in an experiment.

The previous version of the detector simulation for the STS includes uniform energy loss, noise, threshold and Lorentz shift in the magnetic field [62, p.7]. It does not properly reproduce the experimental data for perpendicular tracks (see section 4.3). The decision was made to improve the detector response model. In the following section one can find an overview of the existing simulations of silicon detectors; it is helpful for understanding the way of the further improvements of the STS digitizer. An overview of silicon strip detector simulations from other particle physics experiments demonstrates a wide variety of chosen models.

2.2.1 OVERVIEW OF EXISTING DIGITIZERS

VELO OF LHCb. The VErteX LOcator of the LHCb experiment [79] at (LHC) consists of single-sided silicon strip sensors segmented in a way to measure r or ϕ coordinates [80]. According to [70], the following effects are included into VELO digitizer program:

- the emission of δ -electrons;
- inhomogeneous charge distribution along the track;
- charge diffusion during charge collection;
- capacitive charge coupling between strips.

The VELO is located outside of the magnetic field, thus, no Lorentz shift simulation is needed. The track is divided into $1\text{ }\mu\text{m}$ steps. Energy loss in each segment is sampled using the Geant routine `GLANDZ` [67]. This routine employs Landau, Vavilov or Urban method in dependence on parameters κ and ξ/I (fig. 2.1). Parameter κ is proportional to the ratio of mean energy loss to the maximum allowed energy transfer in a single collision with an atomic electron:

$$\kappa = \frac{\xi}{E_{\text{max}}},$$

E_{max} is the maximum transferable energy in a single collision with an atomic electron. Parameter κ defines the contribution from the collisions with energy transfer close to E_{max} . I is the mean ionisation potential of the atom, and ξ/I defines the contribution of the collisions with low energy transfer. The diffusion is modelled with the Gaussian distribution with width defined by eq. (2.6). The electric field is assumed to be perpendicular to the sensor plane. Charge sharing due to the interstrip capacitances was measured and the results are used in simulations.

SEMICONDUCTOR TRACKING SYSTEM OF ATLAS. The Semiconductor Tracking System of the ATLAS [81] experiment at LHC is based on single-sided silicon microstrip sensors [66]. Each module consists of two daisy-chained sensors glued back-to-back at 40 mrad angle. There are two different digitisation models implemented in the ATLAS semiconductor tracker. The simple approach splits an incident particle trajectory into $5\text{ }\mu\text{m}$ steps, then the energy is divided uniformly among these steps. The energy is converted to charge using the mean electron-hole pair-creation energy of 3.63 eV/pair , and the hole charge drifts to the readout surface in a single step taking into account the Lorentz angle (θ_L) and diffusion. A single value of the Lorentz angle, calculated assuming a uniform value of the electric field over the entire depth of the wafer, is used irrespective of the original position of the hole cloud. The drift time is calculated as a sum of two components: one corresponding to drift perpendicular to the detector surface, calculated assuming an electric field distribution as in a uniform flat diode, and a second corresponding to drift along the surface. The simulation of electronics includes the cross-talk to 2 neighbours. Electronic noise is added to the signal amplitude afterward; it is generated from the Gaussian distribution with the standard deviation equal to the ENC taken from data. Strips with a signal above the readout threshold are recorded. Further random strips from among those without any signal are filled with randomly generated noise amplitudes in order to reproduce the noise occupancy observed in the data.

An advanced digitisation model was implemented in addition in order to check predictions of the simple model. In this model, the drift of both electrons and holes in the silicon is traced step-by-step from the point of production to the strips or HV plane, and the charge induced on the strips from this motion is calculated using a

weighting potential according to the Ramo theorem (2.3). The electric field at each point is calculated using a two-dimensional finite element model. The effect of the diffusion is included by choosing the actual step length, independently in each of two perpendicular distributions, from a Gaussian distribution of width (2.6). The mean cluster width predicted by this model is slightly larger than those predicted by the simple digitisation model. The difference is about $1.6\,\mu\text{m}$ for tracks with incident angles close to the Lorentz angle. The minimum cluster width occurs at incident angles about 0.1° larger in the advanced model. Since both mentioned models give similar output, the default digitisation model is chosen to be a simple model; it is used in the ATLAS numerical simulations.

CDF. The Collider Detector at Fermilab (CDF II) was a general purpose detector with a cylindrical geometry. The silicon detector of CDF consists of three sub-components; the innermost layer L00 is directly mounted on the beampipe [82]. The inner component of the tracking system was a series of silicon microstrip detectors. The sensors were made from high-resistivity n-type silicon with a nominal thickness of $300\,\mu\text{m}$. Sensors in L00 were single-sided, providing $r - \phi$ information.

Detector response model for L00 is described in [73]. In order to simulate the detector response, an incident particle trajectory is divided into $1\,\mu\text{m}$ steps. The total number of the electron-hole pairs is calculated at each step: the number of collisions in $1\,\mu\text{m}$ of silicon is simulated with the Poisson distribution of mean 4, and the energy losses are calculated according to [72]. The diffusion is taken into account according to the model from [63], which involves broadening of a cloud and the Lorentz angle. The Lorentz angle is assumed to be constant for all steps of the trajectory. To simulate noise, the random value distributed according to the Gaussian law was added to each signal.

SILICON DETECTORS OF PAMELA. The PAMELA (a Payload for Antimatter Matter Exploration and Light-nuclei Astrophysics) apparatus is involved in studies of the cosmic ray flux, with a special interest on the antimatter component [83, 84]. The magnetic spectrometer consists of double-sided silicon sensors with $300\,\mu\text{m}$ thickness and orthogonal strips. The detector response simulation is described in [69]. According to it, an incident particle track is divided into $10\,\mu\text{m}$ steps and the charge generation is calculated using the GEANT 3 framework. The electric field is assumed to be parallel on the junction side: charge packets are simply translated towards the strips. The diffusion is considered as a Gaussian enlargement of the packet up to width: $\sigma = \sqrt{2Dt}$. On the ohmic side, the presence of p-stop strips is taken into account: the lower density of field lines can be observed close to stopping strips and charge carriers spend more time before being collected on the strips. The diffusion width was parametrised for the ohmic side as a function of the interstrip position. The cross-talk effect is simulated with a simplified formula: the fraction of the signal appearing on adjacent channel corresponds to the ratio:

$r = C_{\text{interstrip}}/C_{\text{coupling}}$. This ratio is obtained by tuning simulation to fit data. To simulate the electronic noise, Gaussian fluctuations have been superimposed on the signals. The corresponding standard deviation has been extracted from the beam-test data. The magnetic field effects were not included in the simulations.

2.2.2 IMPLEMENTATION OF A REALISTIC STS DIGITIZER

In this section, I describe an implementation of the realistic detector response model for the STS.

2.2.2.1 ENERGY LOSS MODEL

The first method of the energy loss simulation listed in section 2.1.1 does not account for the non-uniformity of the energy loss along an incident particle track. This method could be considered only for total energy loss estimation. Since, the STS sensors are granulated, more detailed description is required. Methods 2(b) and 3 bring considerable computational overhead. They require massive arrays of differential cross-sections. Thus, method 2(a) is chosen for the realistic digitizer. The track of an incident particle is divided into equal-sized layers with length of about $3\text{ }\mu\text{m}$ within the sensor. Then the energy loss is estimated in each layer of the track using Urban method [71]. Such layer length is the lower limit of the standard Urban method, choosing a smaller value requires special implementation of the method. On the other hand, the layer length should be the finest possible to have detailed simulation. The Urban method is used in Geant to compute the energy loss in the similar case to what is present in the STS. The estimate of energy losses is calculated in the `CbmStsPhysics::EnergyLoss` method. The detail description of Urban method is given in Appendix B.

STOPPING POWER. The Urban method requires the mean energy loss as an input parameter. There are tables available for electron and proton stopping powers [85, 86] for energies up to 10 GeV. For electrons with energy up to 100 GeV, we use the table from [87] for silicon. For protons with energy up to 600 GeV, we use data for aluminium from [88]. For other particles (heavier than an electron), the stopping power can be scaled:

$$\left[\frac{dE}{dx}\right]_{M,Z} = Z^2 \left[\frac{dE}{dx} \left(\frac{E \times M_p}{M}\right)\right]_{proton},$$

where Z , E , and M are the charge, the energy, and the mass of the particle, M_p the proton mass [89].

The tables are read and stored by `CbmStsPhysics::ReadDataTablesStoppingPower`, and the calculation of stopping power for the current incident particle is implemented in `CbmStsPhysics::StoppingPower`.

2.2.2.2 CHARGE CARRIER TRANSPORT

DRIFT IN THE ELECTRIC FIELD. Since the electric field lines in the sensor medium are essentially straight except in a small zone close to the surface (see figs. 2.4 and 2.7), the electric field of a planar p-n junction according to eq. (2.2) is implemented: charge carriers drift along a straight line to the electrodes.

For the STS-XYTER, the integration time in the slow channel is 90 – 280 ns [90]. The collection time for a charge carrier produced at the opposite electrode is 8 ns for electrons and 22 ns for holes (at the bias voltage of 100 V, and the detector thickness of 300 μm). Thus, the integration time is larger than the collection time, only the charge carriers, which terminate on the electrode, contribute to signal. There is no need to use the Shockley-Ramo equation (2.3) to evaluate the signal.

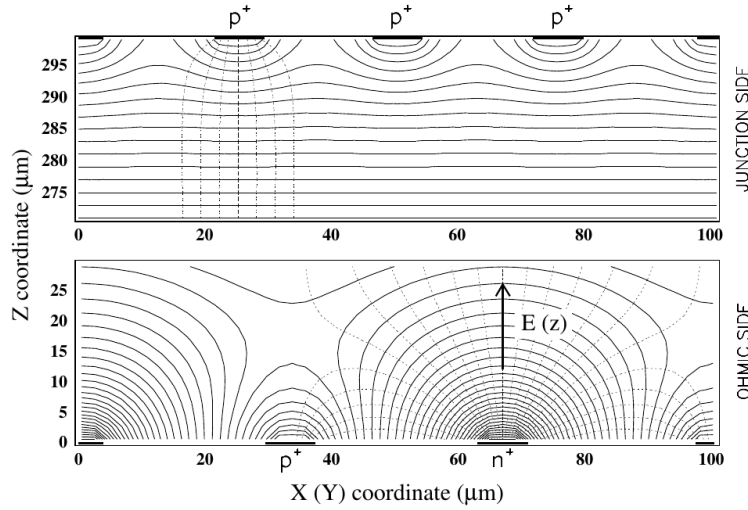


Figure 2.7: Calculated equipotential lines (*solid*) and electric field lines (*dashed*) in proximity of junction (*top*) and ohmic (*bottom*) sides of the sensor. The calculation is done for sensors of PAMELA experiment with strip pitch of 25.5 μm on the p-side and 66.5 μm on the n-side [69].

DIFFUSION. As it was already mentioned, the STS-XYTER integration time is larger than the drift time of the charge carriers, thus, the simple method is used to account for the diffusion. The shape of the charge cloud of each charge package is assumed to be Gaussian with σ given by eq. (2.6). This width is calculated in `CbmStsPhysics::DiffusionWidth`. For each charge package, the fraction of the charge, which is registered in the nearest and two adjacent strips, is estimated in `CbmStsSensorTypeDssd::Diffusion`.

MAGNETIC FIELD INFLUENCE. Formula (2.9) is used to calculate the Lorentz shift. Parameters in this equation appear to be temperature dependent. I use the values of r_H at about 270 K and the following scaling relations taken from [91] for the rest

of parameters. For holes:

$$\begin{aligned}\mu_{\text{low}} &= 470.5 \cdot \left(\frac{T}{300}\right)^{-2.5} \frac{\text{cm}^2}{\text{Vs}} \\ \beta &= 1.213 \cdot \left(\frac{T}{300}\right)^{0.17} \\ v_{\text{sat}} &= 8.37 \cdot 10^6 \cdot \left(\frac{T}{300}\right)^{0.52} \frac{\text{cm}}{\text{s}} \\ r_{\text{H}} &= 0.7.\end{aligned}$$

For electrons:

$$\begin{aligned}\mu_{\text{low}} &= 1417 \cdot \left(\frac{T}{300}\right)^{-2.2} \frac{\text{cm}^2}{\text{Vs}} \\ \beta &= 1.109 \cdot \left(\frac{T}{300}\right)^{0.66} \\ v_{\text{sat}} &= 1.07 \cdot 10^7 \cdot \left(\frac{T}{300}\right)^{0.87} \frac{\text{cm}}{\text{s}} \\ r_{\text{H}} &= 1.15.\end{aligned}$$

The parameters of Hall mobility are calculated in `CbmStsSensorConditions::SetHallMobilityParameters`. Each charge package (the charge created in a trajectory layer) is shifted by Δx . Since the electric field is not constant along the charge package movement trajectory, I assume that the charge package moves in a mean electric field: $E = 0.5 (E(z_1) + E(z_2))$, where z_1 is the coordinate of package creation and z_2 the coordinate of the readout plane for current charge carriers. Using this value of electric field, Δx is calculated in `CbmStsSensorTypeDssd::LorentzShift`.

2.2.2.3 ADDITIONAL EFFECTS

CROSS-TALK. The charge at each strip is recalculated according to eq. (2.11) in `CbmStsSensorTypeDssd::CrossTalk`. This equation can be used as an average estimate over all sensors independent of sensor length. Neglecting C_{bulk} in the denominator is done because $C_{\text{bulk}} \ll C_c$ by 2 order of magnitude. The measured value for C_c and C_i are used [41, pp. 24-25] and are listed below in this section.

The sophisticated approach mentioned in section 2.1.3 involves the readout electronics and micro-cables. I consider here in detail the charge sharing between the strips in the sensor, and the charge division between the sensor, the micro-cable, and the charge sensitive amplifier (CSA).

The ratio of the total charge integrated in the readout electronics to the charge collected on the respective doping implants is estimated in this approach. The

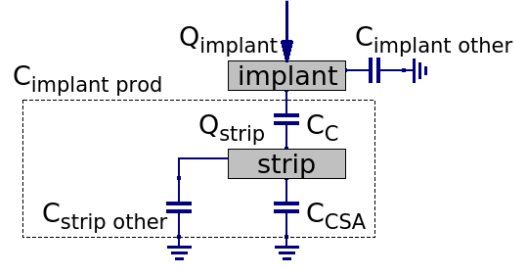


Figure 2.8: Capacitances at strip readout.

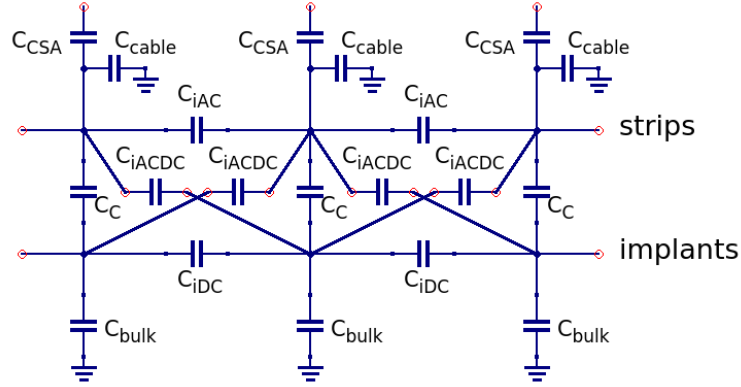


Figure 2.9: Simplified capacitance scheme of microstrip silicon detector with AC-coupling.

time structure of the signal is completely ignored: no ballistic deficit is assumed in the case of the STS readout. This assumption is valid for slow shapers of both n-XYTER ($\tau_{\text{rise}} = 130 \text{ ns}$) and STS-XYTER ($\tau_{\text{rise}} = 80 \text{ ns}$) chips. The maximum drift time of charge carriers in $300 \mu\text{m}$ of silicon is 30 ns , and the signal stretching in the transmission lines between the sensor and the readout electronics is as small as few ns (can be estimated as $R_{\text{cable}}C_{\text{cable}}$) and can be neglected.

The CSA connected to the strip of interest is considered here as a capacitance of value C_{CSA} . The micro-cable is considered as parasitic capacitance C_{cable} . The simplified equivalent circuit of the one readout channel is shown in fig. 2.8. The total capacitance from the implant to the ground and all virtual grounds can be divided into two parts: so-called “productive capacitance” that leads to the charge coupling to the respective strip ($C_{\text{implant prod}}$), and “parasitic capacitance” ($C_{\text{implant other}}$) that leads to the charge sharing between strips or to the charge loss through back plane of the sensor. In general, $C_{\text{implant other}} \neq 2C_{\text{iDC}} + 2C_{\text{iACDC}} + C_{\text{bulk}}$, but assuming $C_{\text{iDC}}, C_{\text{iACDC}}, C_{\text{bulk}} \ll C_{\text{C}}, C_{\text{CSA}}$ (that is the case for the STS), $C_{\text{implant other}} = 2C_{\text{iDC}} + 2C_{\text{iACDC}} + C_{\text{bulk}}$, where C_{iDC} is the capacitance between neighbouring implants, C_{iAC} the capacitance between neighbouring aluminium strips, C_{iACDC} the capacitance between the implant and neighbouring aluminium strip (all the capacitances are shown on the right part of fig. 2.6 and fig. 2.9). The productive capacitance of the

implant is

$$C_{\text{implant prod}} = \frac{C_c(C_{\text{strip other}} + C_{\text{CSA}})}{C_c + C_{\text{strip other}} + C_{\text{CSA}}}.$$

With the assumption that $C_{\text{iAC}}, C_{\text{iACDC}}, C_{\text{cable}} \ll C_{\text{CSA}}$, the parasitic capacitance of the strip is $C_{\text{strip other}} = C_{\text{cable}} + 2C_{\text{iAC}} + 2C_{\text{iACDC}}$.

The charge coupled to the aluminium strip is

$$Q_{\text{strip}} = \frac{Q_{\text{implant}} C_{\text{implant prod}}}{C_{\text{implant prod}} + C_{\text{implant other}}}. \quad (2.13)$$

The charge integrated in the CSA is

$$Q_{\text{CSA}} = \frac{Q_{\text{strip}} C_{\text{CSA}}}{C_{\text{CSA}} + C_{\text{strip other}}}. \quad (2.14)$$

Formula (2.14) estimates the integrated charge in the CSA connected to the strip of interest. To estimate the charge integrated on the neighbouring CSA, I consider several paths, through which the neighbouring CSA couples to the implant of interest. I take into account the charge sharing only within the sensor (not within the micro-cable or in the chip). Therefore, if the charge coupled to the neighbouring strip is known, the integrated charge on the neighbouring CSA can be estimated with formula (2.14). Then the charge integrated in the neighbouring CSA is

$$\begin{aligned} Q_{\text{CSA}}^{\text{neib}} = Q_{\text{implant}}^{\text{centr}} \frac{Q_{\text{CSA}}^{\text{neib}}}{Q_{\text{strip}}^{\text{neib}}} & \left(\frac{Q_{\text{strip}}^{\text{neib}}}{Q_{\text{implant}}^{\text{neib}}} \cdot \frac{Q_{\text{implant}}^{\text{neib}}}{Q_{\text{implant}}^{\text{centr}}} + \frac{Q_{\text{strip}}^{\text{neib}}}{Q_{\text{implant}}^{\text{centr}}} + \right. \\ & \left. + \frac{Q_{\text{strip}}^{\text{centr}}}{Q_{\text{implant}}^{\text{centr}}} \cdot \frac{Q_{\text{strip}}^{\text{neib}}}{Q_{\text{strip}}^{\text{centr}}} + \frac{Q_{\text{strip}}^{\text{centr}}}{Q_{\text{implant}}^{\text{centr}}} \cdot \frac{Q_{\text{implant}}^{\text{neib}}}{Q_{\text{strip}}^{\text{centr}}} \cdot \frac{Q_{\text{strip}}^{\text{neib}}}{Q_{\text{implant}}^{\text{neib}}} \right) \end{aligned} \quad (2.15)$$

Here, the first term in the brackets corresponds to the charge sharing through C_{iDC} and C_c and comprises about 90 % of the total charge integrated on the neighbouring strip (for the capacitance values given in section 2.2.2.3), the second term corresponds to the coupling through C_{iACDC} (about 6 % of the total charge), the third term through C_c and C_{iAC} (about 2 % of the total charge), and the last term through C_c , C_{iACDC} and C_c (about 1 % of the total charge). The following formulae can be used to calculate terms, given in the last equation:

$$\begin{aligned} \frac{Q_{\text{implant}}^{\text{neib}}}{Q_{\text{implant}}^{\text{centr}}} &= \frac{C_{\text{iDC}}}{C_{\text{implant prod}} + C_{\text{implant other}}}, \\ \frac{Q_{\text{strip}}^{\text{neib}}}{Q_{\text{implant}}^{\text{centr}}} &= \frac{C_{\text{iACDC}}}{C_{\text{implant prod}} + C_{\text{implant other}}}, \end{aligned}$$

$$\frac{Q_{\text{implant}}^{\text{neib}}}{Q_{\text{strip}}^{\text{centr}}} = \frac{C_{\text{iACDC}}}{Q_{\text{CSA}} + C_{\text{strip other}}},$$

$$\frac{Q_{\text{strip}}^{\text{neib}}}{Q_{\text{strip}}^{\text{centr}}} = \frac{C_{\text{iAC}}}{Q_{\text{CSA}} + C_{\text{strip other}}}.$$

Then, eq. (2.15) can be written as

$$\begin{aligned} Q_{\text{CSA}}^{\text{neib}} = Q_{\text{implant}}^{\text{centr}} \frac{Q_{\text{CSA}}}{Q_{\text{strip}}} & \left(\frac{Q_{\text{strip}}}{Q_{\text{implant}}} \cdot \frac{C_{\text{iDC}}}{C_{\text{implant prod}} + C_{\text{implant other}}} + \right. \\ & + \frac{C_{\text{iACDC}}}{C_{\text{implant prod}} + C_{\text{implant other}}} + \frac{Q_{\text{strip}}}{Q_{\text{implant}}} \cdot \frac{C_{\text{iAC}}}{C_{\text{CSA}} + C_{\text{strip other}}} + \\ & \left. + \left(\frac{Q_{\text{strip}}}{Q_{\text{implant}}} \right)^2 \frac{C_{\text{iACDC}}}{C_{\text{CSA}} + C_{\text{strip other}}} \right). \end{aligned} \quad (2.16)$$

Formulae (2.14) and (2.16) implicitly depend on lengths of the sensor and the micro-cable, which blocks the implementation of these in the digitizer because no sensor-specific parameters are currently supported.

For the verification of the detector response model described in section 4.3, detailed formulae (2.14) and (2.16) were used to estimate the charge integrated on the CSA connected to the strip of interest and neighbouring strips. C_{iAC} , C_{iDC} , C_{iACDC} , C_{c} , C_{bulk} were measured in [41, pp. 24-25] for several sensors. Mean values are used for the simulations (for CiS sensors): $C_{\text{bulk}} = 0.21 \pm 0.004 \text{ pF/cm}$, for p-side

$$\begin{aligned} C_{\text{iDC}} &= 0.417 \pm 0.021 \text{ pF/cm}, \\ C_{\text{iAC}} &= 0.0333 \pm 0.0017 \text{ pF/cm}, \\ C_{\text{iACDC}} &= 0.0250 \pm 0.0013 \text{ pF/cm}, \\ C_{\text{c}} &= 20 \pm 3 \text{ pF/cm}, \end{aligned}$$

for n-side

$$\begin{aligned} C_{\text{iDC}} &= 0.542 \pm 0.054 \text{ pF/cm}, \\ C_{\text{iAC}} &= 0.043 \pm 0.004 \text{ pF/cm}, \\ C_{\text{iACDC}} &= 0.036 \pm 0.004 \text{ pF/cm}, \\ C_{\text{c}} &= 17 \pm 3 \text{ pF/cm}. \end{aligned}$$

Uncertainties of the interstrip capacitances are large because the central values vary strip-to-strip a lot. For example, fig. 2.10 shows the interstrip capacitance for one CiS single-metal sensor $6 \times 6 \text{ cm}^2$.

C_{cable} for the particular prototype of the micro-cable was measured and simulated

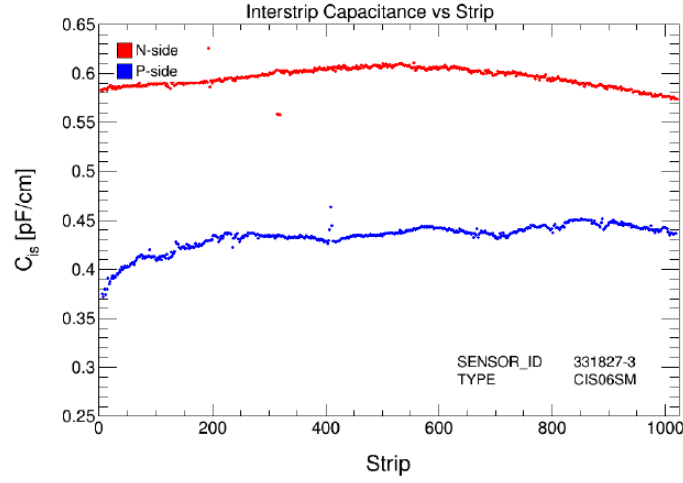


Figure 2.10: Interstrip capacitance C_{is} measured strip-by-strip for one single-metal sensor produced by CiS [92].

in [93, p. 144]. The value of 1.06 ± 0.2 pF/cm was chosen for both layers of the micro-cable; the discrepancy between values for different layers was found to be negligible comparing to the uncertainty. The design value of the n-XYTER input capacitance is $C_{CSA} = 300$ pF [94]. To estimate the dispersion of C_{CSA} value, the measurements from [78, p. 78] were used. From data in [78] I calculated C_{CSA} for 2 out of 128 channels of one particular chip: $C_{CSA_1} = 306 \pm 10$ pF and $C_{CSA_2} = 309 \pm 11$ pF. The measured values are consistent with the design value within the estimated uncertainties. Therefore, the design value $C_{CSA} = 300 \pm 10$ pF was confirmed for the usage in the simulations.

The sophisticated approach requires measurement of the capacitances of the latest version of the micro-cable and the sensor. It has to be implemented because the charge redistribution over all the capacitance plays leading role for the signal amplitude (see section 4.3 and Appendix F).

ELECTRONICS. Simulation of the response of the readout electronics includes the signal-correlated noise, the threshold, the digitisation of the analog signal in the ADC, the time resolution and the single-channel dead time.

The STS-XYTER chip will be operated in self-trigger mode, this way one can consider an impact of the noise only for channels with a signal. The noise amplitude is assumed to follow the Gaussian distribution with $\sigma = ENC$, the Equivalent Noise Charge is obtained from the measurements. The ENC depends on the micro-cable length and the sensor size (see eq. (2.12)). In the current implementation of the digitizer, the measured averaged value of 1000 e is used for the ENC for different modules. This value is consistent with the simulation performed by the STS-XYTER developers group [90]. The noise, which is non-correlated with the signal, yet to be included into the complete time-based simulation of the STS.

A typical value of the threshold value is set at 3 ENC in order to suppress the noise sufficiently but not to lose the signal [95, p. 17].

The conversion of the analog signal $q[e]$ into the digital signal $q[ADC]$ is implemented with formula:

$$q[ADC] = \frac{q[e] - Q_{thr}}{Q_{max}} nADC, \quad (2.17)$$

where $nADC$ is the number of the ADC channels, Q_{max} the dynamic range, Q_{thr} the threshold. If the analog signal is bigger than the dynamic range, $q[ADC] = nADC - 1$. In case of the STS-XYTER chip, $nADC = 32$ (5-bit ADC), $Q_{max} = 12 \text{ fC}$ [90].

The time resolution and the single-channel dead time are important for the time-based simulation. The respective values are 5 ns and 800 ns [96]. The chip bandwidth is big enough ($9 - 47 \text{ Mhit/s}$ per ASIC [58]) for the expected occupancy (see section 2.3.1), hence it is not required to be included into the simulation: no data loss is expected due to bandwidth constraint.

2.2.2.4 INFLUENCE OF THE MODELLED EFFECTS ON THE PERFORMANCE

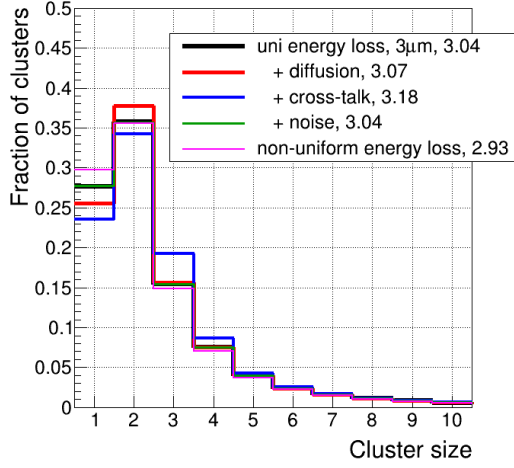
In this section, I address an influence of above described physical processes on the performance measures. Particularly, an impact on the cluster size, spatial resolution, etc., is presented. Five hundred minimum bias Au+Au events at 10 AGeV are simulated using the `cbmroot` framework. As a reference, the ideal detector response model with threshold and charge discretisation in readout electronics is used. In this model, the trajectory is divided into $\approx 3 \mu\text{m}$ layers, each of them receives the same amount of the deposited energy. To study the influence of each effect, I expand the reference model by adding one effect at a time: the diffusion, the cross-talk, the noise, and the non-uniform energy loss.

For cluster reconstruction, the simple cluster finder and the unbiased cluster position finding algorithm were involved (see section 3.1). Also, hits were reconstructed without any MC information (simple hit finder, see section 3.2).

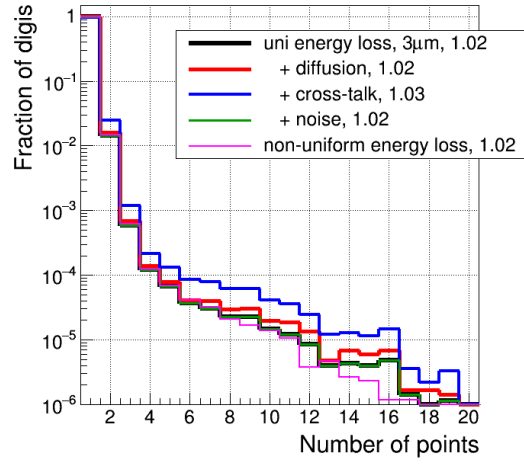
Figure 2.11a shows that the diffusion increases the probability of 2-strip cluster formation and suppresses appearance of 1-strip clusters but almost does not influence other cluster sizes in comparison with the reference case. The cross-talk increases the number of 3-strip and wider clusters at the expense of 1- and 2-strip clusters. The noise does not affect the cluster size distribution. All the effects mentioned above affect observables within the expectations. However, it appears to be nontrivial to predict an impact of the non-uniformity. As we can see from fig. 2.11a, it increases the number of 1-strip clusters.

Figure 2.11b shows that adding the cross-talk to the model increases the pile-up probability from about 1.5 % up to 2.7 %. Because the cross-talk influence depends on the capacitances in the equivalent sensor scheme (interstrip capacitance, coupling capacitance, etc.), careful measurement of these values is required.

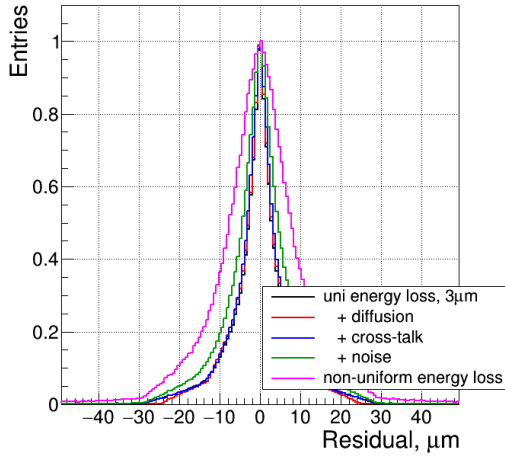
The non-uniformity of energy loss and noise are the key effects that deteriorate the spatial resolution: a difference between the true and the reconstructed position, see figs. 2.11c and 2.11d.



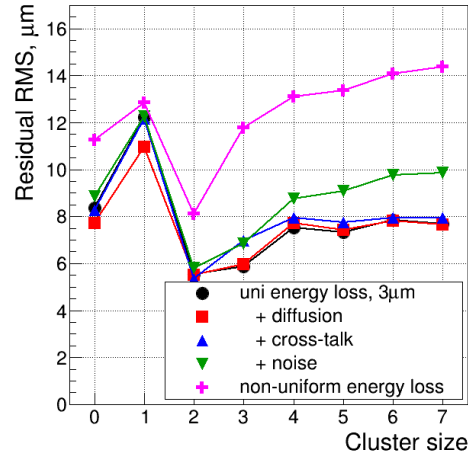
(a) Cluster size distribution.



(b) Number of incident particles (Monte-Carlo points) which correspond to one digi.



(c) Residual distributions for all clusters normalised by maximum. Only residuals for x-coordinate are shown (not inclined strips).



(d) Residual RMS vs cluster size. Only residuals for x-coordinate are shown (not inclined strips). Label "0" corresponds to all clusters.

Figure 2.11: Distributions for different detector response models: *black* — uniform energy loss only (trajectory is divided into $3\mu\text{m}$ steps), *red* — uniform energy loss with diffusion, *blue* — uniform energy loss with cross-talk, *green* — uniform energy loss with noise effects added, *magenta* — non-uniform energy loss only. In all cases, the threshold (3000e) and charge discretisation are as well taken into account.

2.3 COMPARISON WITH THE SIMPLE MODEL

In this section, a confirmation of the necessity of the development of the realistic detector response model is presented. I compare the previous model [62, p.7] with the new version described in section 2.2.2. The previous model is still available in the `cbmroot` framework as an optional approach. It includes the uniform energy loss, the noise, the threshold and the Lorentz shift in magnetic field with the average value of mobility for all the charge carriers of same sign. The realistic model enhances the simple model by taking into account the non-uniform energy loss, the diffusion, and the cross-talk. Also, the Lorentz shift is taken into account in a more advanced way (section 2.2.2.2) as opposed to the simple eq. (2.9). I used the same value of the noise and the threshold in the realistic model to facilitate comparison. No magnetic field was included in these simulations. For this task, 500 minimum bias Au+Au events at 10 AGeV were simulated.

2.3.1 DIGI LEVEL

Digi level is aimed to reproduce a raw data acquired by the detector in a real experiment. Figure 2.12 shows a comparison between the simple and the realistic models of detector response. In *top-left* panel of fig. 2.12, the number of digis produced by one MC-point (one MC-point corresponds to an incident particle crossing one sensor) is shown. The realistic model predicts more digis per particle, resulting in a higher value of the detector occupancy than the simple model prediction.

Top-right panel of fig. 2.12 shows the number of pile-up digis — digis, which correspond to two or more MC-points. The corresponding signals induced by several particles cannot be distinguished already at the level of readout electronics. The charge of such a digi is a sum of charges from each incident particle. The simple model artificially decreases pile-up effect from about 2.9 % down to 1.6 %. This is an expected effect, because the simple model does not include any charge sharing.

Digi charge distribution is presented in *bottom-left* panel of fig. 2.12. The peak at 31st ADC channel is explained by the details of the STS-XYTER operation. If the analogue signal charge is higher than the chip dynamic range (about $75000e = 12fC$), the biggest ADC value (31) is assigned to the charge (see section 2.2.2.3). The realistic model gives almost twice larger number of digis with charge of 1 ADC. This can become crucial for signal surviving if the threshold has to be increased due to a high noise level. The digis with charge as low as 1 ADC are not recorded in this case. This constraint makes noise suppression a key issue in the detector integration.

In the *bottom-right* panel of fig. 2.12, the total number of digis created in the whole STS in one Au+Au event is plotted. It can give one a feeling of how fast readout and data acquisition systems have to be. Occupancies for each module can be found in Appendix A. This prediction is used by DAQ (Data Acquisition) group of CBM

to estimate the number of readout lines that are required in the real experiment.

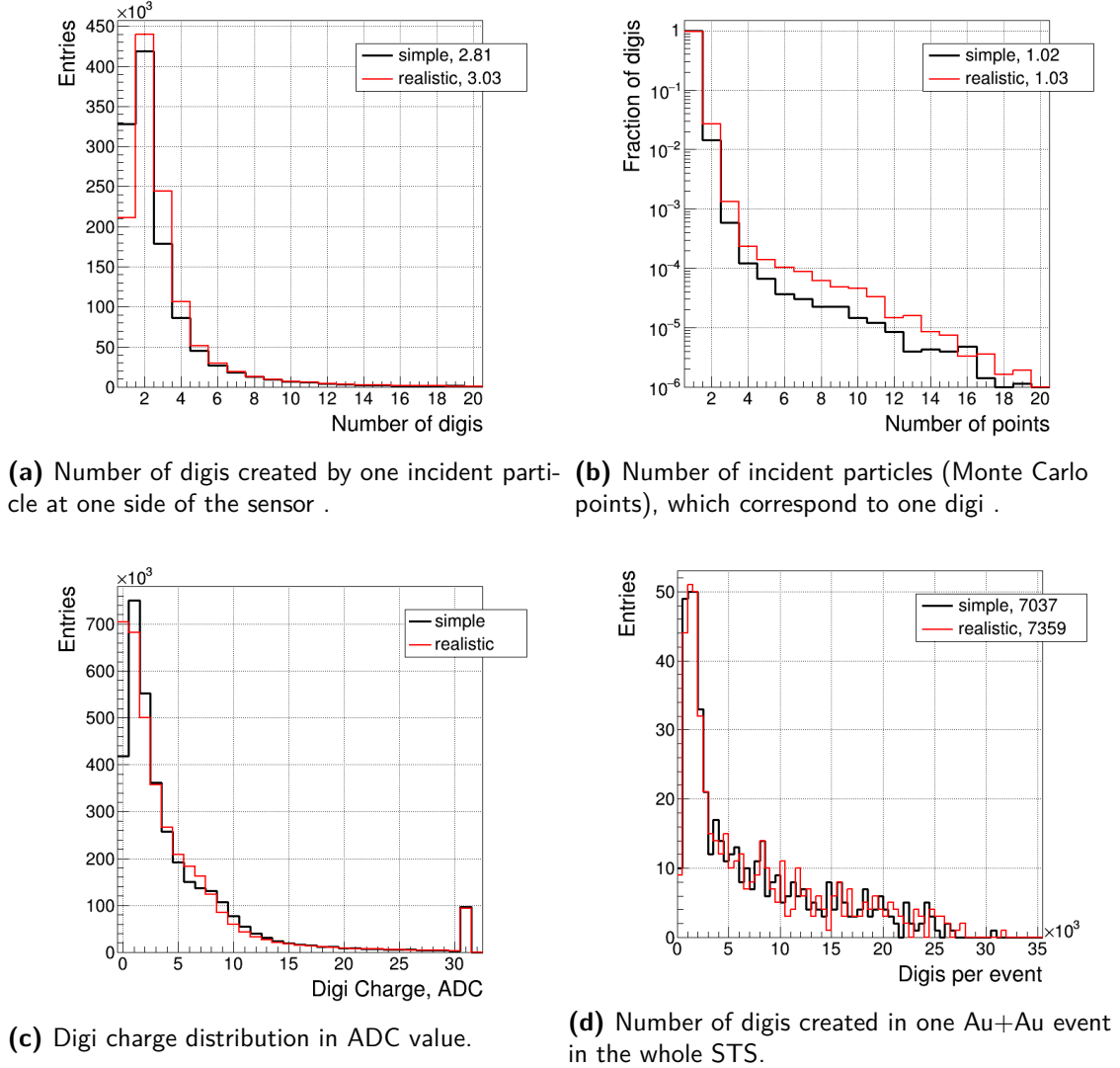
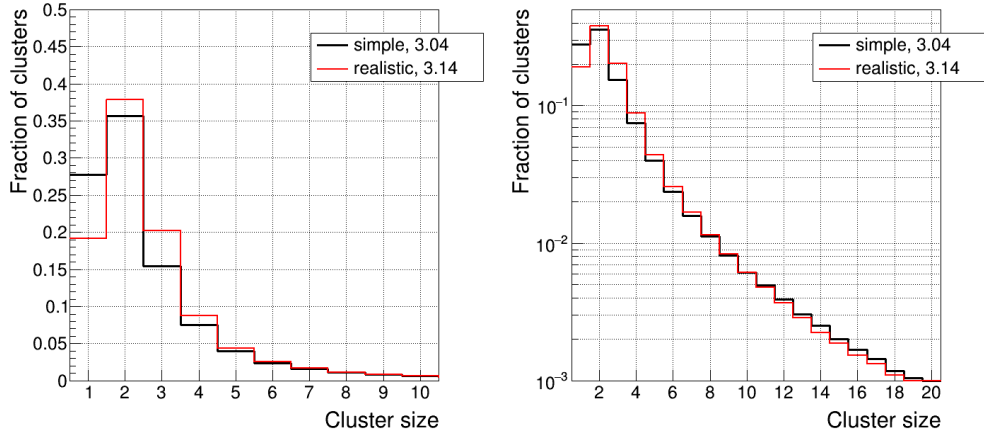


Figure 2.12: Distributions for the simple (black) and the realistic (red) detector response models. Mean values are given in the legends.

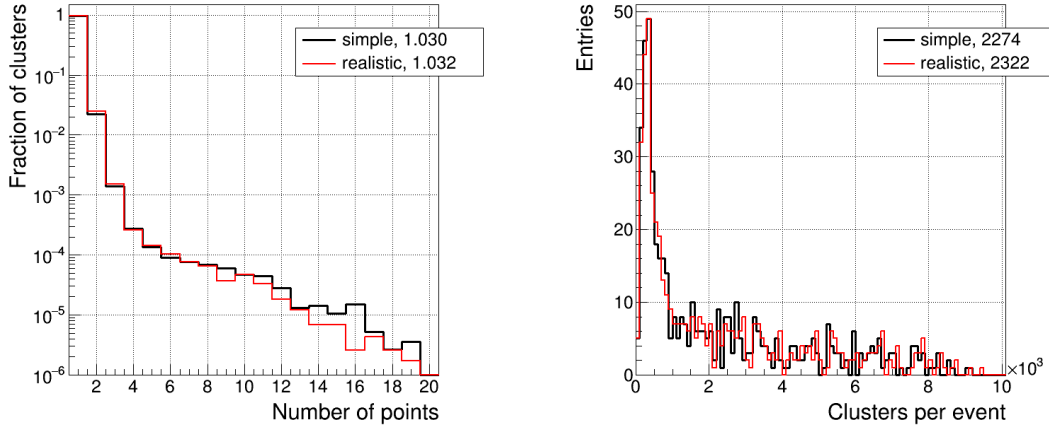
2.3.2 CLUSTER LEVEL

In this section, the simple cluster finder and the unbiased cluster position finding algorithm were employed (see section 3.1).

Figures 2.13-2.15 compare the performance of cluster reconstruction for two detector response models. Two *top* panels of fig. 2.13 reproduces an expected increase of mean cluster size. As it was shown in section 2.2.2.4, diffusion and cross-talk are two main contributors to this effect.



(a) Cluster size distribution.



(b) Number of incident particles (Monte-Carlo points) which correspond to one cluster.

(c) Number of reconstructed clusters in one Au+Au event in the whole STS.

Figure 2.13: Distributions for the simple (*black*) and the realistic (*red*) detector response models. Mean value of each plotted variable is mentioned in the corresponding legend.

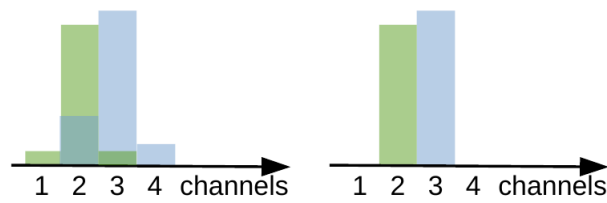
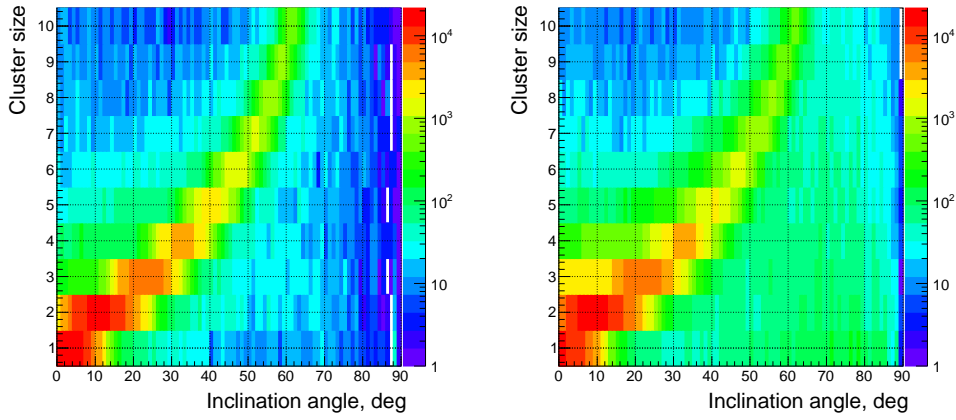
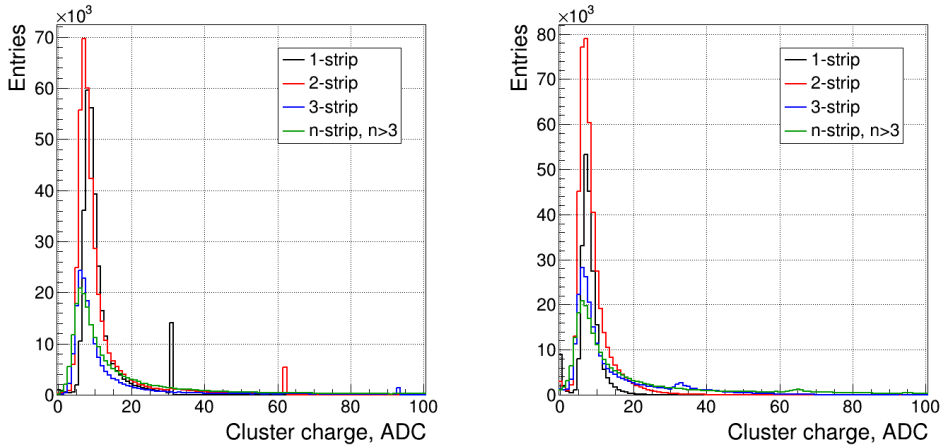


Figure 2.14: Merged clusters obtained using the realistic (*left*) and the simple (*right*) detector response model.

Bottom-left panel of fig. 2.13 shows that the number of merged clusters (overlapping or adjacent clusters treated as one) only 3 % larger with the realistic model than with the simple model though the corresponding difference in the digis pile-up is four times higher and reaches 13 % (see section 2.3.1). A reason for this effect is illustrated in fig. 2.14. Consider two adjacent digis in the simple model (left panel). In the realistic model, these digis can pile up into one digi due to the cross-talk and/or diffusion (right panel). Thus, in the simple model in this case, there is no digis pile-up but a cluster merge, while in the realistic model there is both the digis pile-up and the cluster merge. Therefore, the difference between the models in the merged clusters is smaller than in the digis pile-up.



(a) Cluster size dependence on inclination angle of incident particle track. The angle is calculated in plane perpendicular to sensor plane and perpendicular to strip direction. Colour scale represents the number of clusters.



(b) Cluster charge dependence on cluster size.

Figure 2.15: Distributions for the simple (*left*) and the realistic (*right*) detector response models.

Distribution of number of reconstructed clusters in one event is shown on the

bottom-right panel of fig. 2.13. More reconstructed clusters can increase hit reconstruction efficiency but increase number of fake hits as well (see section 3.2 for fake hits explanation).

Figure 2.15a presents a cluster size distribution as a function of the track angle. The simple detector model gives more pronounced and closer to one-to-one dependence in comparison to the realistic one. Another difference is the cluster size distribution for slightly inclined tracks: the realistic model predicts more 2- and 3-strip clusters at the expense of 1-strip clusters.

Figure 2.15b shows charge sharing processes in two response models. Cluster charge distribution for the simple model (*left* panel) has artefacts: spikes at ADC bins 31, 62, 93... To explain this, I refer to fig. 2.12c: digi charge distribution. When a particle loses large amount of energy in a sensor and has almost perpendicular track w. r. t. to the sensor plane, the simple model, most probably, produces only one digi. And this digi is considered as a 1-strip cluster. Thus, there is a spike for 1-strip cluster charge (the *black* line on the left panel of fig. 2.15b). A similar issue appears for a particle with some non-zero inclination: two digis with charge 31 ADC each are created and combined into a 2-strip cluster with charge 62 ADC (the spike for 2-strip clusters at 62 ADC, *red* line on the left panel of fig. 2.15b). The realistic model does not give these spikes but broad peaks after ADC bin: 31, 62, 93... A particle with the high energy loss, which penetrates a sensor perpendicularly, creates a 3-strip cluster: one neighbouring channel from each side of the fired channel gets some small charge due to cross-talk effect. In fig. 2.15b, there is a peak after 31 ADC exactly for 3-strip clusters (*blue* line on the right panel). The same explanation applies to bigger clusters (*green* line).

2.3.3 HIT LEVEL

The hit level enables analysis of spatial resolution (see section 3.2). The RMS of residual distribution is used to estimate the spatial resolution. It depends on the cluster size. The highest resolution is obtained for 2-strip clusters (see fig. A.3 and also fig. 2.16, Appendix A) and it worsens with increase of cluster size. The resolution determined using all cluster sizes depends on input cluster size distribution. As it was mentioned before, 500 Au+Au minimum bias events at 10 AGeV are simulated to reproduce the track angle distribution in the CBM experiment. For this distribution, the simple model yields on the average $2\mu\text{m}$ smaller residuals. For cluster size 3 and more strips, the residuals are underestimated by about $5\mu\text{m}$ with the simple model.

Hit reconstruction efficiency remains unchanged for both simple and realistic detector response model (see table 2.1). Fraction of fake hits increase from 33.4 % to 36.5 % for realistic detector response model in comparison with the simple one. This is explained by the increase in number of reconstructed clusters.

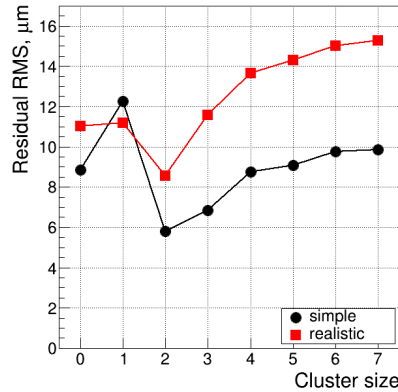


Figure 2.16: Residual RMS for different cluster sizes obtained using the simple (*black*) and the realistic (*red*) detector response models. Label “0” corresponds to all clusters.

Table 2.1: Hit reconstruction quality using the simple detector response model and the realistic one.

	Detector response model	
	Simple	Realistic
Number of reconstructed hits per event	1325	1391
Reconstruction efficiency, all particles	99.5 %	99.5 %
Reconstruction efficiency, π , $p_t > 0.5$ GeV	99.7 %	99.8 %
Fake hits fraction	33.4 %	36.5 %

2.3.4 TRACK LEVEL

The main requirement for the STS is high momentum resolution. At the same time, tracking efficiency should be kept high. In the `cbmroot`, the Cellular Automaton (CA) is employed to reconstruct tracks [97]. The Kalman Filter (KF) based track fit is used for precise estimation of the track parameters [98]. The reconstruction efficiency is defined as a ratio of reconstructed to reconstructable tracks. A track is reconstructable if an incident particle traverses at least four stations.

Simulations show that the tracking performance remains sufficient even after all the relevant processes being included in the model (see fig. 2.17). Momentum resolution is dominated by multiple scattering in the material; it limits the influence of the detector response model.

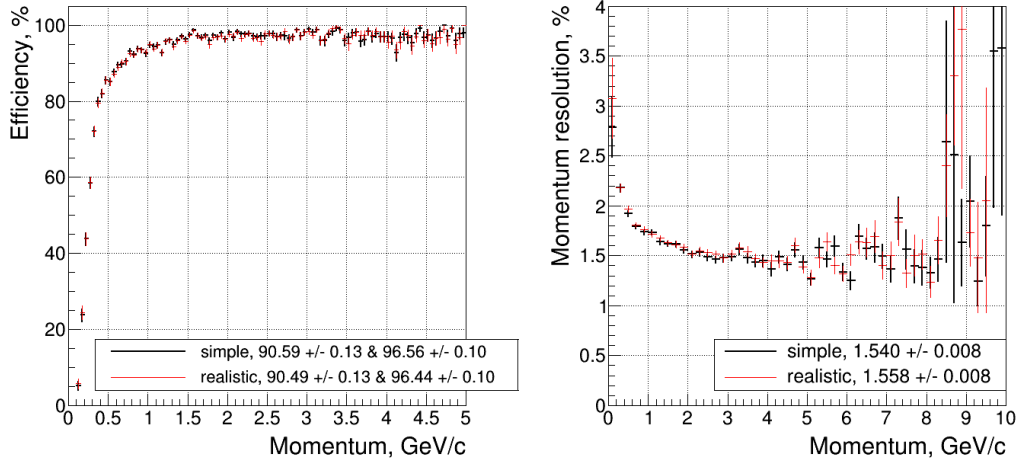


Figure 2.17: Tracking efficiency (*left*) and momentum resolution (*right*) when the simple (*black*) or the realistic detector response model (*red*) is used. In the *left* legend, the efficiency for all and fast (with $p > 1$ GeV) tracks is given. In the *right* legend, the average resolution only for fast tracks is shown.

2.4 SUMMARY

The previous version of the detector simulation for the STS [62, p.7] includes uniform energy loss, noise, threshold, and Lorentz shift in the magnetic field. However, it has some deviation with the experimental data (see section 4.3). The new realistic detector response model was designed and implemented. It enhances the previous simple model with non-uniform energy loss (according to the Urban model), diffusion, cross-talk due to the interstrip capacitance, and an advanced description of the Lorentz shift (see section 2.2.2). The detector response model described above was implemented in `cbmroot` such that the various physical effects can be switched on or off separately. This allows to study the influence of each effect on the detector performance. The simulation shows that both the diffusion and the cross-talk enlarge the detector occupancy and the cluster size. Both non-uniformity of the energy loss and the electronics noise worsen the spatial resolution (see section 2.2.2.4).

The main handle to validate the detector response model against data obtained from the tests of the detector prototypes is the cluster size distribution as a function of track incident angle on the sensor. The realistic model agrees better with the in-beam test data than the previous model. Accounting for the charge redistribution due to the presence of parasitic capacitances brings the most significant improvements into agreement (see section 4.3). Since 2017, the realistic model is the default version in `cbmroot` simulations.

The total STS performance obtained with two different models was compared (see section 2.3). The simple model yields underestimation of the pile-up effect: it

yields 1.6 % of digis, which correspond to two or more MC points, but the realistic model estimates it as 2.9 %. Detector occupancy (fired strips occupancy) is also underestimated by the simple model: it gives in average 7040 fired strips per event, while the realistic model gives 7360. These quantities are important for design of the DAQ system. Also, neglecting the realistic effects causes overestimation of the hit reconstruction quality. Namely, the spatial resolution is better by $5\text{ }\mu\text{m}$ for big clusters (with 3 or more strips) without including the realistic effects. The rate of fake hits increases from 33.4 % to 36.5 % with including of the realistic effects. At the same time, tracking performance in the STS only slightly depends on the chosen detector response model. Namely, the momentum resolution stays the same because it is dominated by multiple scattering in the material.

The realistic detector response model is a promised tool to get reliable results of the detector performance at different conditions: after irradiation (see section 4.2.2), at high noise level, with some strips/chips/modules being not read out [99], with sensors of different thicknessn [100]. Also, the realistic digitizer was used to study the potential of the STS as a particle identification detector involving measurements of the energy loss in the sensor [101].

Employing a simplistic detector response model is misleading in a detector performance estimate. The choice of a realistic detector response model should be done with a comparison against experimental data and with a comparison the model's influence on the detector performance as well. The second is necessary because there are several effects that deteriorate the detector performance but at the same time they are difficult to measure in experiment and distinguish their influence among other effects.

3

STS cluster and hit reconstruction

The proper choice of reconstruction algorithms allows to employ full capability of the detector. An accurate reconstruction of both position and error of the interaction point of a particle with the detector is required. It is a prerequisite for the determination of the particle momentum with high resolution.

The structure of this chapter is the following:

- Section 3.1 presents general ideas of cluster reconstruction and compares two cluster position finding algorithms.
- Section 3.2 describes hit reconstruction in double-sided strip sensors.
- In section 3.3, hit position error is discussed: an overview of existing method to estimate this error, the developed analytical method for the STS, and its verification.

3.1 CLUSTER RECONSTRUCTION

The goal of the cluster reconstruction is to group digis originating from the same incident particle into one object called cluster. This procedure is implemented in two steps: the cluster construction (the digis grouping) and the determination of the cluster centre. All the amplitude values that pass a hardware threshold produce digis; this way they all are considered to be signals at the first iteration. There are 3 models of the cluster finder currently implemented in the STS software:

- **ideal:** the Monte-Carlo information is used for cluster construction. In such an approach, a cluster is constructed from all the digis actually originating from

one incident particle. If several clusters are overlapped, they are excluded from the further analysis because signals from different particle in one strip can not be separated. This model is not applicable in a real experiment, but it is useful for testing purposes, for example, to test quality of position reconstruction (see section 3.1.3).

- **simple:** no MC information is used in the reconstruction. All neighbouring digis are combined into a cluster.
- **with dead channels map:** this model allows to account for dead channels. Some readout channels can be broken during different production stages: sensors or readout chips production, modules integration. A map of dead channels is available before the data acquisition. The cluster finder has an access to such a map, it is used during cluster construction. The algorithm allows clusters to have a gap in place of the dead channel.

Figure 3.1 illustrates the procedures implemented in the cluster finder models mentioned above.

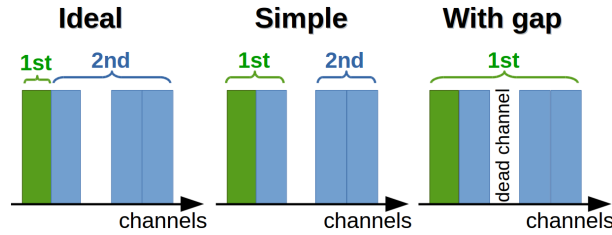


Figure 3.1: Performance of different cluster finder models: ideal (*left*), simple (*middle*), and with gap (*right*). Different colours of channels correspond to different incident particles that produce a digi. Braces show reconstructed clusters.

After digis are combined into clusters, an algorithm performs determination of the cluster centres. The cluster centre is a reconstructed position of the point, where the incident particle traverses the middle plane of the sensor. A Cluster Position Finding Algorithm (CPFA) calculates the cluster centre out of registered charges on the fired channels. The cluster centre position measured in channel numbers, because a conversion from channel number into geometrical position is trivial only on the n-side of the sensor, where strips are continuous. On the p-side, however, the outer (short) strips are interconnected with each other over the second metallisation layer (see section 1.4 and fig. 3.2), which leads to ambiguity, where interaction actually took place. Therefore, the geometrical position is calculated afterwards, during hit reconstruction. Combination of the information from both sides resolves the ambiguity (see fig. 3.2). Uncertainty of the cluster position is calculated in terms of integer channel numbers.

A position of the incident particle has to be reconstructed from the charges q_i measured on the strips of the cluster. Quality of a position reconstruction algorithm

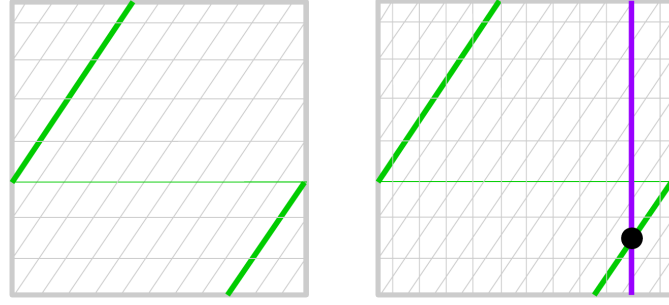


Figure 3.2: *Left:* Scheme of p-side strips interconnection. One green strip is fired, but due to second metal layer (thin horizontal green line), geometrical coordinate can not be reconstructed uniquely. *Right:* Strips scheme on both sides: p and n. Green strip is fired on p-side and violet strip — on n-side. Intersection of p- and n-strips gives uniquely reconstructed hit coordinate. The stereo-angle is shown not to scale.

is tested against minimising the position residuals. Residual is defined as the difference between true (x_{true}) and reconstructed (x_{rec}) values of the cluster position

$$\Delta x = x_{\text{true}} - x_{\text{rec}}. \quad (3.1)$$

It shows the accuracy of cluster position reconstruction. Moreover, the error of the reconstructed position

$$\sigma^2 = \langle \Delta x^2 \rangle - \langle \Delta x \rangle^2 \quad (3.2)$$

should be calculated as well to provide a correct estimation of the spatial resolution.

The algorithm is required to be unbiased, which means that the mean value of the residual should be zero. In other words, unbiased algorithm provides an estimate of the position without introducing a systematic shift.

To study the influence of the algorithm itself on the spatial resolution, at first, a simple model of the detector response and an ideal detector were applied. Later, all the realistic effects were added to the detector model. As the first order approximation, the detector response of silicon sensors can be described as a uniform charge distribution along the projection of the particle trajectory on the readout (strip) plane. This charge distribution, which is then integrated on the readout channels, can be characterised by two independent variables: the entry and the exit coordinates of the track in the sensor, x_{in} and x_{out} . Since the thickness of the sensors is small, the trajectory within the sensor is approximated by a straight line neglecting the multiple scattering and bending in the magnetic field, and the true coordinate is defined as

$$x_{\text{true}} \stackrel{\text{def}}{=} (x_{\text{in}} + x_{\text{out}})/2. \quad (3.3)$$

3.1.1 CENTRE-OF-GRAVITY ALGORITHM

A commonly used algorithm for cluster position finding is the Centre-Of-Gravity (COG) algorithm [68], which defines the cluster centre as

$$x_{\text{rec}} \stackrel{\text{def}}{=} \sum_i x_i q_i / Q, \quad (3.4)$$

where x_i is the centre coordinate of strip i , and $Q = \sum_i q_i$ is the total charge in the cluster.

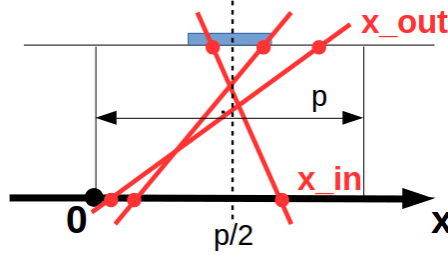


Figure 3.3: Schematic drawing of particle trajectories, which yield 1-strip clusters.

1-STRIP CLUSTERS. If only one strip gets the charge, the reconstructed position is defined straightforwardly: $x_{\text{rec}, 1s} = x_i$ (here and later in the text, index “1s” means “1-strip clusters”, “2s” — “2-strip clusters”, and “Ns” — “n-strip clusters”). In the coordinate system as shown in fig. 3.3, $x_{\text{rec}, 1s} = p/2$, with p being the strip pitch. Probability density distribution for trajectories that create a 1-strip cluster can be derived from those for x_{in} and x_{out} . Both variables are assumed to be uniformly distributed in $[0, p]$ (this has been confirmed with the simulations, see fig. 3.4) and independent. In this case, the non-normalised probability density $P_1(x_{\text{in}}, x_{\text{out}}) = P(x_{\text{in}}) \times P(x_{\text{out}})$, where

$$P(x_{\text{in/out}}) = \begin{cases} 1, & x_{\text{in/out}} \in [0, p] \\ 0, & x_{\text{in/out}} \notin [0, p] \end{cases}.$$

The normalisation factor for this probability density function is calculated as

$$N = \int_{x_{\text{in}}} \int_{x_{\text{out}}} P_1(x_{\text{in}}, x_{\text{out}}) dx_{\text{in}} dx_{\text{out}} = p^2. \quad (3.5)$$

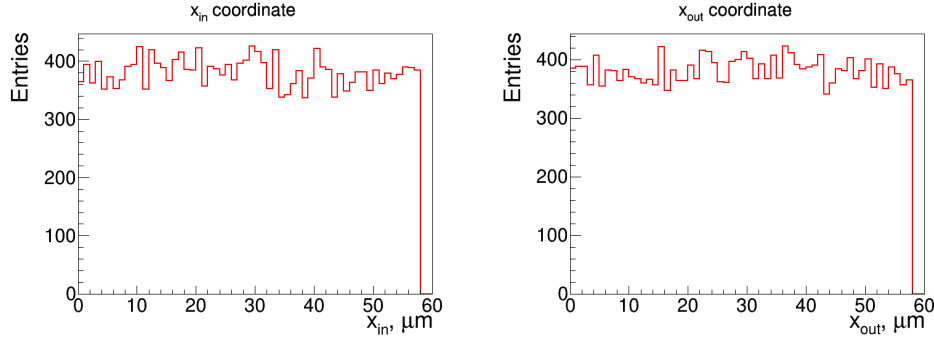


Figure 3.4: Simulated distributions for x_{in} and x_{out} for 1-strip clusters as expected in the STS.

And the mean value of the residual distribution is

$$\langle \Delta x \rangle = \langle x_{\text{true}} - x_{\text{rec}} \rangle = \frac{1}{N} \int \int_{x_{\text{in}} x_{\text{out}}} P_1(x_{\text{in}}, x_{\text{out}}) dx_{\text{in}} dx_{\text{out}} \left(\frac{x_{\text{in}} + x_{\text{out}}}{2} - \frac{p}{2} \right) = 0. \quad (3.6)$$

This means that the COG algorithm provides unbiased estimation of the position for 1-strip clusters. The mean position error can be estimated from

$$\begin{aligned} \sigma^2 = D = \langle \Delta x^2 \rangle - \langle \Delta x \rangle^2 &= \langle \Delta x^2 \rangle = \frac{1}{N} \int \int_{x_{\text{in}} x_{\text{out}}} P_1(x_{\text{in}}, x_{\text{out}}) dx_{\text{in}} dx_{\text{out}} \Delta x^2 = \\ &= \frac{1}{4N} \int \int_{x_{\text{in}} x_{\text{out}}} P_1(x_{\text{in}}, x_{\text{out}}) dx_{\text{in}} dx_{\text{out}} (x_{\text{in}} + x_{\text{out}} - p)^2 = \frac{p^2}{24}. \end{aligned} \quad (3.7)$$

Thus, the estimate of the position error for 1-strip clusters, which comes from the COG algorithm itself, is

$$\sigma_{\text{CPFA, 1s}} = \frac{p}{\sqrt{24}}. \quad (3.8)$$

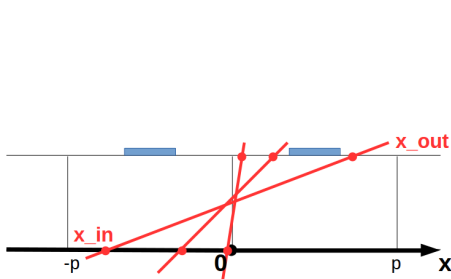


Figure 3.5: Schematic draw of 2-strip clusters formation.

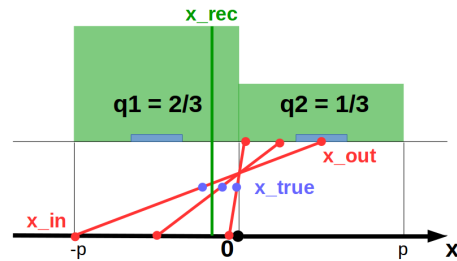


Figure 3.6: Possible trajectories of the particles that correspond to the 2-strip clusters with a fixed $k = q_2/q_1 = 1/2$.

2-STRIP CLUSTERS. The coordinate system (c.s.) is defined in fig. 3.5. The reconstructed coordinate is then: $x_{\text{rec}, 2s} \stackrel{\text{def}}{=} p/2 \times (q_2 - q_1)/(q_2 + q_1)$, where $q_{1,2}$ are the charges registered on the left and the right strip, respectively (see fig. 3.5). As in case of 1-strip clusters, it is assumed that x_{in} and x_{out} are independent, x_{in} is distributed uniformly in $[-p, 0]$ and x_{out} — in $[0, p]$. This assumption is only an approximation as fig. 3.7 shows.

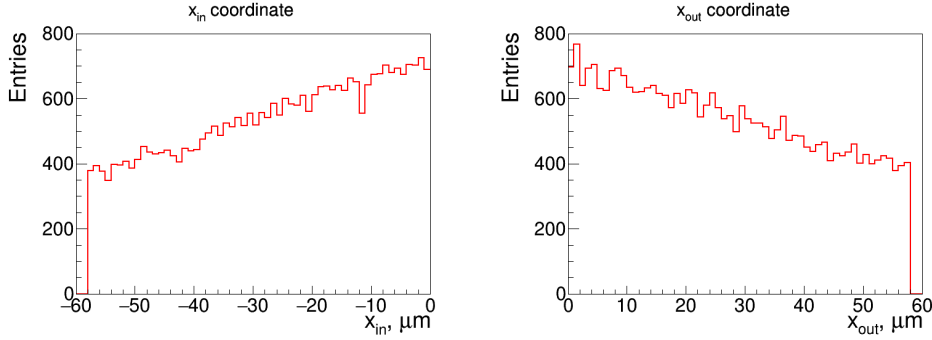


Figure 3.7: Simulated distributions for x_{in} and x_{out} for 2-strip clusters as expected in the STS.

The whole set of 2-strip clusters can be subdivided into subsets of clusters with a fixed ratio $k = q_2/q_1$ of the measured charges $q_{1,2}$ by the strips. Such subsets are natural consequence of the measurements performed by the strip detector — collection of the charge at a strip. Each subset is formed by a set of particle trajectories (see fig. 3.6). Since the fixed ratio k sets a constraint on the possible trajectories, one variable $(x_{\text{in}} + x_{\text{out}})/2 \equiv x_{\text{true}}$ together with the k value is enough to fully describe the given trajectory. Thus, the probability density function for the subset with a fixed ratio k can be calculated by the formula (see Appendix C):

$$P_2(x_{\text{true}}, k) = P(x_{\text{in}}) \cdot P(x_{\text{out}}) \cdot \left| \frac{-4x_{\text{true}}}{(1-k)^2} \right|. \quad (3.9)$$

where $P(x_{\text{in/out}})$ is defined as

$$P(x_{\text{in}}) = \begin{cases} 1, & x_{\text{in}} \in [-p, 0] \\ 0, & x_{\text{in}} \notin [-p, 0] \end{cases};$$

$$P(x_{\text{out}}) = \begin{cases} 1, & x_{\text{out}} \in [0, p] \\ 0, & x_{\text{out}} \notin [0, p] \end{cases}.$$

The CPFA is required to give the minimal residual not on average for all clusters, but for given measured $q_{1,2}$. Thus, the calculation of the mean residual for the fixed

k gives (see Appendix C.2 for details):

$$\frac{1}{N} \int_{x_{\text{true}}} P_2(x_{\text{true}}, k) dx_{\text{true}} \Delta x \neq 0. \quad (3.10)$$

In other words, the COG algorithm for 2-strip clusters is biased (see fig. 3.12).

N-STRIP CLUSTERS. The reconstructed position is defined by eq. (3.4). The estimation of the mean residual is similar to 1- and 2-strip clusters but is cumbersome. Since the method is biased already for 2-strip clusters, further calculations are omitted. Thus, in general, the COG algorithm does not provide a bias-free cluster reconstruction.

3.1.2 THE UNBIASED ALGORITHM

A unbiased algorithm can be derived from the requirement that the average residual $\langle x_{\text{rec}} - x_{\text{true}} \rangle$ vanishes (this section is based on [102] and [103]).

1-STRIP CLUSTERS. The only unbiased solution for 1-strip clusters is the same as for the COG algorithm (see section 3.1.1):

$$x_{\text{rec}, 1s} \stackrel{\text{def}}{=} x_i \quad (3.11)$$

and $\sigma_{\text{CPFA}, 1s} = p/\sqrt{24}$.

2-STRIP CLUSTERS. Condition $\langle x_{\text{rec}} - x_{\text{true}} \rangle \equiv 0$ lets one define x_{rec} as $\langle x_{\text{true}} \rangle$ for 2-strip clusters with given k in c.s. from fig. 3.6. In Appendix C.1, it is shown that $\langle x_{\text{true}} \rangle = p/3(q_2 - q_1)/(\max(q_1, q_2))$ (see eq. (C.6)) in the frame centred in the middle between the fired strips (see fig. C.1). Thus,

$$x_{\text{rec}, 2s} \stackrel{\text{def}}{=} \frac{1}{2}(x_1 + x_2) + \frac{p}{3} \frac{q_2 - q_1}{\max(q_1, q_2)}. \quad (3.12)$$

The corresponding dispersion

$$\sigma^2 = \frac{p^2}{72} \left(\frac{q_2 - q_1}{\max(q_1, q_2)} \right)^2. \quad (3.13)$$

Thus, in general:

$$\sigma_{\text{CPFA}, 2s} = \frac{p}{\sqrt{72}} \frac{|q_{i+1} - q_i|}{\max(q_i, q_{i+1})}, \quad (3.14)$$

where fired strips have numbers i and $i + 1$.

N-STRIP CLUSTERS. For clusters with number of strips $n > 2$ with fired strips from i to j the reconstruction position is calculated as (see Appendix D):

$$x_{\text{rec, Ns}} \stackrel{\text{def}}{=} \frac{1}{2} (x_i + x_j) + \frac{p}{2} \frac{q_j - q_i}{q_{i+1}}. \quad (3.15)$$

In case of ideal detector and uniform energy loss $q_{i+1} = q$, where $k = i + 1, \dots, j - 1$. This prescription exactly reproduces the true coordinate, i.e., the corresponding error vanishes.

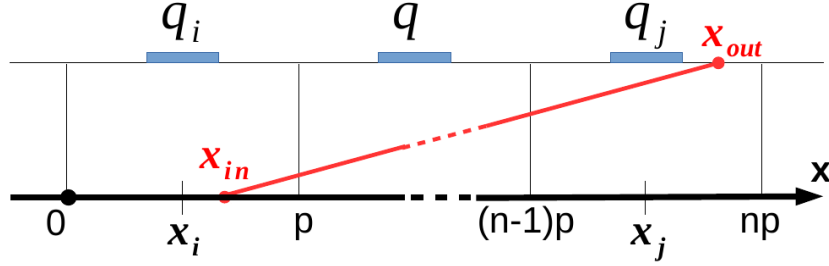


Figure 3.8: Schematic drawing of n -strip clusters formation.

Formula (3.15) works for uniform energy loss but introduces large residual in case of big fluctuations of energy losses, which sometimes occur. To avoid the influence of big fluctuations and other effects (for example, noise), several improvements are added to the formula:

$$x_{\text{rec, Ns}} \stackrel{\text{def}}{=} \frac{1}{2} (x_i + x_j) + \frac{p}{2} \frac{\min(q_j, q) - \min(q_i, q)}{q}; \quad q \stackrel{\text{def}}{=} \frac{1}{n-2} \sum_{k=i+1}^{j-1} q_k. \quad (3.16)$$

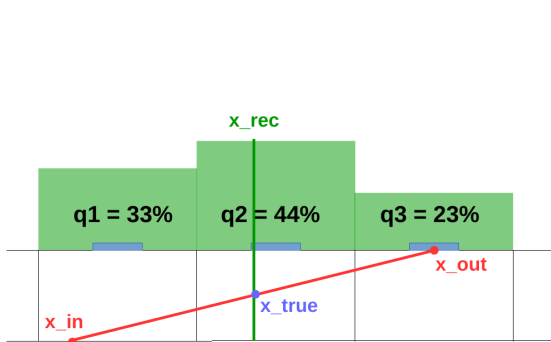


Figure 3.9: Schematic example of a 3-strip cluster simulated with the uniform model of energy losses and reconstructed with formula (3.15).

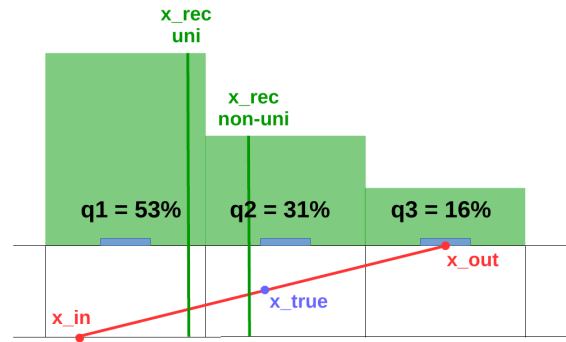


Figure 3.10: Schematic example of a 3-strip cluster simulated with the non-uniform model of energy losses and reconstructed with formula (3.15) (marked as “ $x_{\text{rec uni}}$ ”) and with formula (3.16) (marked as “ $x_{\text{rec non-uni}}$ ”).

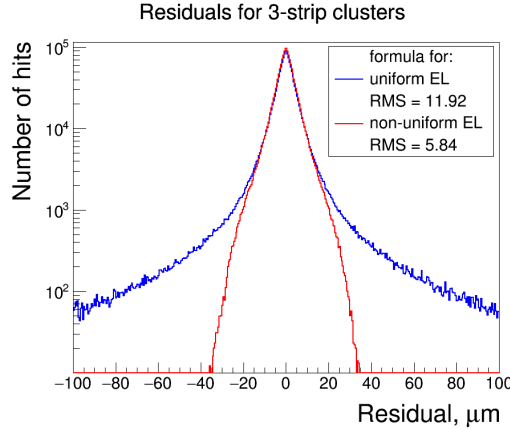


Figure 3.11: Residuals for 3-strip clusters using formula for the uniform energy loss (3.15) (*blue* line) and for the non-uniform energy loss (3.16) (*red* line). The ideal cluster finder and the ideal detector response were used with the non-uniform energy loss of the incident particle modelled.

Such constructed CPFA has a name “Analog head-tail” position finding algorithm [68]. Figures 3.9 and 3.10 explain how the energy loss model influences position finding precision. When the uniform energy loss is used in the simulation, formula 3.15 reconstructs the cluster position with zero residual (see fig. 3.9). But when the realistic non-uniform energy loss is simulated, the improved formula 3.16 yields better reconstruction (see fig. 3.10) than formula 3.15: the cluster position reconstructed with eq. (3.16) “ $x_{rec\ non-uni}$ ” is closer to the true coordinate “ x_{true} ” than the position reconstructed with eq. (3.15) “ $x_{rec\ uni}$ ”. Figure 3.11 shows the difference in residuals with both formulae, if the simulation includes the non-uniform energy loss of the incident particle.

Formula for non-uniform energy loss (3.16) is used in the unbiased algorithm, but the error introduced by the algorithm is assumed to be 0. The error due to the non-uniform energy loss will be explained in section 3.3.2.3.

3.1.3 ALGORITHMS COMPARISON

The motivation to develop a new CPFA was to find an unbiased algorithm. Figure 3.12 proves that our new algorithm is unbiased for 2-strip clusters: it gives zero average residuals at each configuration of $q_{1,2}$.

Several effects lead to deviations from a uniform charge distribution on the readout plane. These are fluctuations in the amount of charge created along the trajectory, the total system noise, the threshold, the diffusion and the charge discretisation in the readout electronics. In order to study the influence of the effects on the residuals of the cluster position, each of them was added one-by-one into the simulation. Figure 3.13 shows the RMS of residual distributions depending on different processes, which are taken into account in the simulation of the detector response. Labels’ explanation are the following:

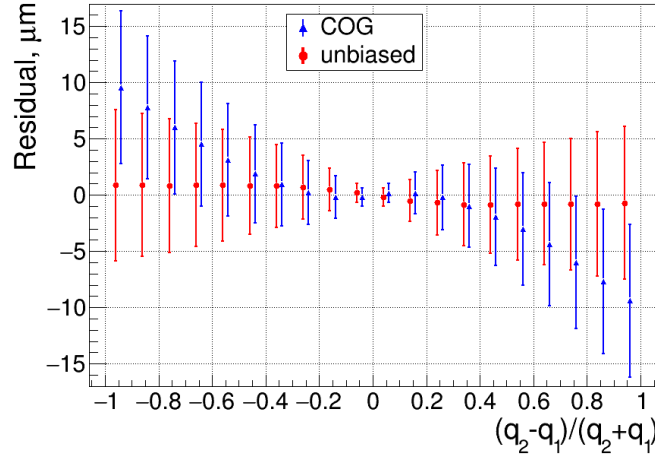


Figure 3.12: Simulated average residuals for 2-strip clusters as a function of the measured $q_{1,2}$. Data in *blue* are obtained with the COG algorithm, those in *red* — with the unbiased algorithm. The error bars are the RMS of the residual distribution. The data points are misaligned horizontally for visibility.

uni ideal: An ideal detector and the uniform energy loss along the particle trajectory. Each strip gets a fraction of the total charge, which is proportional to the trajectory projection on the strip. The term “ideal detector” means also:

- ignoring particles with $x_{\text{in/out}}$ out of the sensor active area;
- ignoring particles, which either are created inside the sensor or do not leave the sensor: $z_{\text{in/out}}$ inside the sensor volume;
- no dead time and perfect time resolution.

uni steps: The particle trajectory is divided into small steps (about $3\mu\text{m}$). Charge created at each step is registered in the strip according to the step centre position.

non-uni: The Urban method is used to simulate a non-uniform charge carriers creation along the incident particle trajectory (see section 2.2.2.1 for more details).

- + **discr:** The registered charge in each channel is discretised in the readout chip.
- + **noise:** The noise model is added to the detector response simulation.
- + **thr:** The threshold is applied.
- + **diff:** The diffusion is included to the detector model.
- + **cross talk:** The influence of the interstrip and other capacitances is taken into account.
- + **simple finders:** A simple cluster and hit finders (definitions in sections 3.1 and 3.2) are switched on, the “ideal detector” is switched off. An ideal cluster finder and an ideal hit finder are employed in all previous cases (see sections 3.1 and 3.2 for definitions).

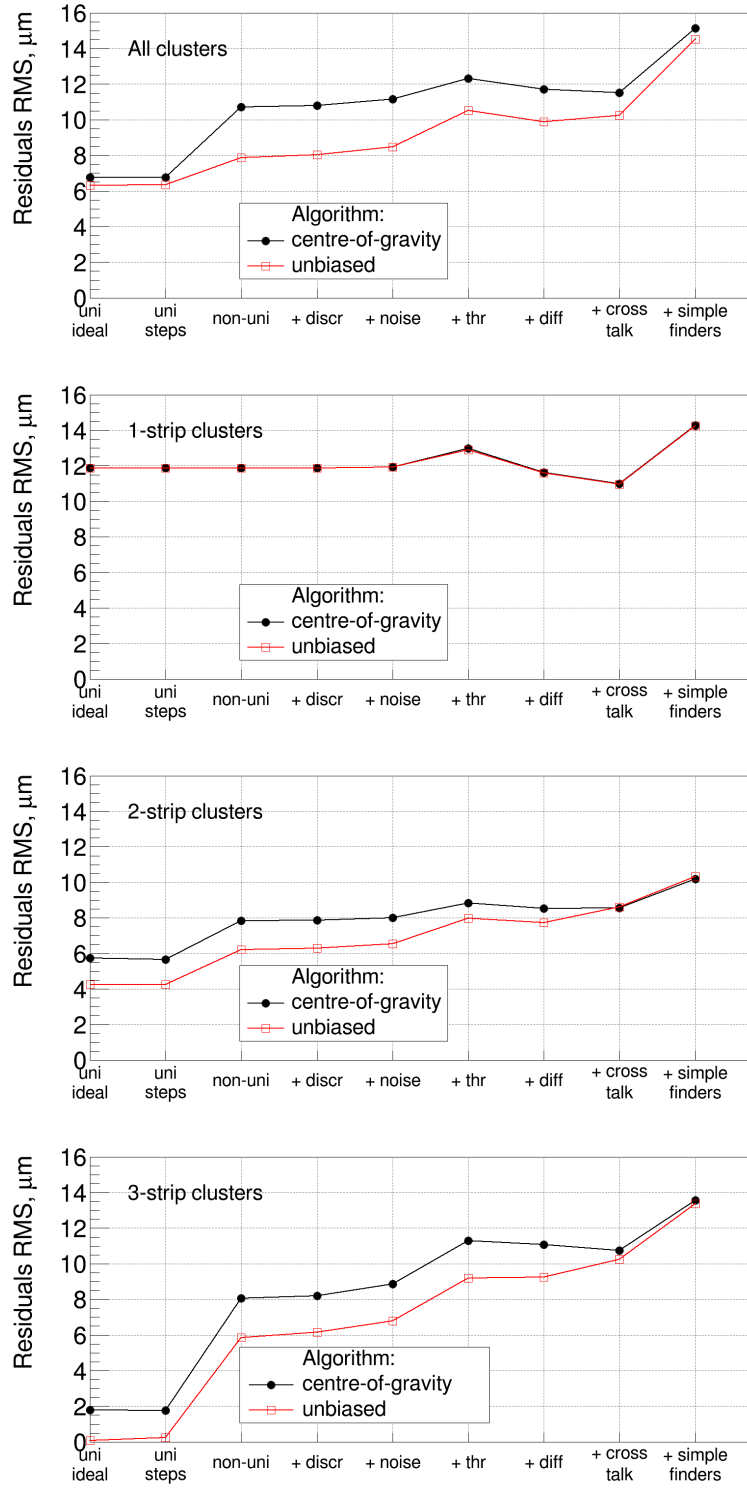


Figure 3.13: RMS of simulated residual distribution for Au+Au events at 10 AGeV for all clusters (*top*), only 1-strip clusters (*second top*), only 2-strip clusters (*second bottom*) and only 3-strip clusters (*bottom*) when taking into account different processes. See labels explanation in text.

All the effects mentioned in fig. 3.13 lead to the degradation of the position resolution such that the residual distribution alone does not favour the unbiased algorithm over the COG. However, the unbiased algorithm has an advantage that it is mathematically correct. Moreover, as shown in section 3.1.2, the unbiased algorithm allows to estimate the hit position error a priori. Thus, it will be used to estimate the hit position and its error (see section 3.3.2).

3.2 HIT RECONSTRUCTION

A hit is a combination of two clusters, centres of which correspond to the strips on different sides of the sensor that geometrically cross each other. Hits are characterised with geometrical coordinates in metric units (unlike cluster centres in channel numbers). The hit position is defined as the crossing point of the clusters on the p- and the n-sides of the sensor. The skew coordinate system that corresponds to the strip directions (see fig. 3.14) eliminates correlation between measurements on the opposite sides of the sensor. In this case, the uncertainty of the hit position is the cluster position uncertainty multiplied by strip pitch.

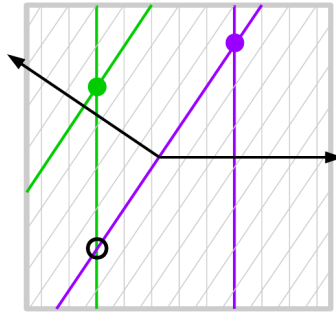


Figure 3.14: Hits in double-sided silicon sensors. The vertical grey lines show strips on one side of the sensor, the inclined lines — those on the other side (the stereo angle is not to scale for visibility). The figure illustrates two particles from the same event crossing the sensor. Green strips are fired by one particle, violet — by another. Three hits are reconstructed from the fired strips: two true hits shown with filled dots with corresponding colours and a fake hit due to the accidental intersection of the strips fired by different particles shown with an empty dot. The coordinate system is drawn with black arrows, the origin point is arbitrarily chosen.

Two models of the hit finder are currently implemented in the STS software:

- **ideal:** uses the MC information. A hit is a combination of two clusters that actually correspond to the same and only one incident particle. The number of reconstructed hits cannot exceed the number of MC points: there is no fake interaction points, commonly referred to as ghost or fake hits (see fig. 3.14).
- **simple:** no MC information is used. This method will be used in the reconstruction of the real experiment data. Number of reconstructed hits depends

on the number of reconstructed clusters on both sides of the sensor. If there is only one cluster on the p- and one cluster on the n-side, the position of the particle can be determined unambiguously. However, if there is more than one cluster on one of the sides of the sensor, and if the clusters can not be resolved in time, then finding the actual position of the particle can become ambiguous (see fig. 3.14). In such case, all possible crossing points are considered, and for every crossing point a hit is created. The fake hits can later be rejected by the track reconstruction algorithm [52]. The number of fake hits in a sensor with stereo angle α can be estimated as $(n^2 - n) \tan \alpha$ [61], where n is a number of particles, which traverse the sensor in the given time window.

3.3 ESTIMATION OF THE HIT POSITION ERROR

Being measurements of particle trajectories at the position of a station, found hits are used for reconstruction of tracks. For precise estimation of track parameters the Kalman Filter (KF) [104] based track fit is widely used in high energy physics and heavy ion experiments, as well as in the CBM experiment [53]. The KF method requires knowledge of not only the parameters of a measurement, but their precision as well, thus the covariance matrices of hits should be estimated.

In case of the STS detector, the errors of track parameters are caused by:

- intrinsic resolution of the detector that includes the error introduced by a cluster position finding algorithm and the error caused by non-ideal charge measurement (see section 3.3.2 for details);
- multiple scattering of particles in the material of the station including sensors, cables and support structures. Due to the low material budget of the STS stations, multiple scattering does not have an effect on the hit error itself, however it affects track parameters after track extrapolation between the stations or into the outer regions of the STS detector (to other subdetectors, such as the MUCH or the TOF).

Let us estimate the affect of the multiple scattering on the track position errors. For simplicity, tracks are assumed to be straight that corresponds to the case of zero magnetic field. The thickness of the innermost part of each STS station corresponds to $0.4 \% X_0$ and the average thickness of one STS station corresponds to $1 \% X_0$. Such low amount of material causes scattering at small angles, however it is large enough for a particle to undergo on average more then 10 acts of scattering. Therefore, according to the central limit theorem, the scattering angle distribution can be approximated with the Gaussian law with the width [105]:

$$\sigma_\theta = \frac{13.6 \text{ MeV}}{\beta c p} z \sqrt{x/X_0} [1 + 0.038 \ln(x/X_0)],$$

where p , βc , and z are the momentum, velocity, and charge number of the incident particle, and x/X_0 is the thickness of the scattering medium in units of radiation length. For 5 GeV pions and 10 cm distance between two stations, the width of the scattering angle distribution translates into $22 \mu\text{m}$ in case of $1\% X_0$ station thickness and $13 \mu\text{m}$ for $0.4\% X_0$ thick station. Thus, the contribution of the multiple scattering is the same order of magnitude as the errors originating from the intrinsic spatial resolution of the detector. Therefore for the correct fit of track parameters, correct estimation of hit position errors is of the particular importance.

All relevant physical processes, which occur in the detector, should be taken into account for estimation of the hit position error. The current implementation of the STS digitisation model (see section 2.2.2) allows each of the processes to be included independently providing a tool for investigation of their individual influence on the reconstructed hits.

In the next section, I give an overview of the methods, which are used by other groups worldwide to estimate hit position error.

3.3.1 OVERVIEW OF EXISTING METHODS FOR ESTIMATION OF THE HIT POSITION ERROR

Trackers built from silicon strip detectors were used or are being used in other experiments in high energy physics, for example, in LHCb and CMS at LHC. Thus, several algorithms were developed for estimation of hit position error for such kind of detectors.

3.3.1.1 VERTEX LOCATOR OF LHCb

The LHCb experiment contains the VELO detector built from the silicon strip detectors for precise vertex reconstruction [79]. In [106], the errors for u and v stereo coordinates are defined as $N \times \text{pitch} / \sqrt{12}$ for N strip clusters (u is the radial axis and v is the axis perpendicular to u resolved at the average ϕ). However, the parametrisation of the cluster position error as a function of the pitch only, as previously used in the LHCb tracking, is not sufficient for high quality determination of track parameters.

In [107] authors provide two version of continuous two dimensional parametrisations (pitch-angle) of the cluster position error. In the first version, one dimensional parametrisations as a function of pitch are produced for bins of projected angle

$$res^{1D}(\text{pitch})_{\alpha=\text{const}} = p_0^\alpha + p_1^\alpha \times \text{pitch}.$$

In the second, one dimensional parametrisations as a function of projected angle are produced for bins of pitch

$$res^{1D}(\alpha)_{\text{pitch}=\text{const}} = p_0^{\text{pitch}} + p_1^{\text{pitch}} \sin(p_2^{\text{pitch}} \times \alpha + p_3^{\text{pitch}}).$$

The parameters p_i are extracted from simulated events and pull distributions are used for the verification. When only the clusters are available, the error estimate is based on the parametrisation determined for the mean value of the projected angle of tracks in LHCb. This may lead to a very distorted pull distribution as a function of projected angle.

Thus, the simple method of the error estimation from [106] is not sufficient, and the second 2D method from [107] requires angle of tracks to be known.

3.3.1.2 THE STRIP DETECTOR OF THE CMS TRACKER

In the tracker of the CMS experiment [108], the uncertainty in the hit position is parametrised as a function of expected width of the cluster obtained from the track angle. In [109] additionally, when the observed width of a cluster exceeds the expected width by at least a factor of 3.5, the uncertainty in the position is set to the “binary resolution”, namely, the width of the cluster divided by $\sqrt{12}$. This broadening of the cluster is caused by capacitive coupling between the strips or energetic delta rays.

This method is applicable only after a track is reconstructed and the track angle is calculated.

3.3.1.3 ESTIMATION OF RESOLUTION FROM EXPERIMENTAL DATA AND SIMULATION

In [63], authors discuss their method to estimate the hit position error. At first, they fit the experimental data obtained with strip sensors with a model of charge sharing. The model includes planar electric field, charge carriers diffusion, their shift in magnetic field, and non-zero width of the primary produced charge distribution. The model assumes constant charge carriers mobility (not dependent on electric field and temperature), constant Lorentz angle (not dependent on electric field). There are three free parameters of the fit: the Lorentz angle, the effective temperature of the charge carriers, and the width of primary charge distribution. After obtaining these parameters from the fit, this charge sharing model together with the additional noise model of electronics is used in Monte-Carlo simulation for the perpendicular tracks of incident particles. The reconstructed position is calculated with the Centre-of-Gravity algorithm (same as described in section 3.1.1). The distribution of the difference between the simulated and the reconstructed position of the particle provides an estimation of the resolution. The resolution are calculated for different readout pitch. For example, for strip pitch and readout pitch both of $20\text{ }\mu\text{m}$, the resolution is $2.8\text{ }\mu\text{m}$.

A disadvantage of this method is the necessity to do the measurements (to find the proper parameters from the fit) and then run the simulation for each incident angle.

3.3.2 DEVELOPMENT OF THE ANALYTIC METHOD

3.3.2.1 GENERAL IDEA OF ESTIMATION OF HIT POSITION ERROR

In this section, I present a method for estimation of the hit position error that is obtained from the first principles and is independent of measured spatial resolution or simulated residuals (this section is based on [102]). Thus, the developed method does not depend either on the approximations applied in the simulation model, or conditions of the performed measurements. For instance, measured resolution cannot be used if penetrating angle is not known, because the resolution strongly depends on angle.

The method focuses on the intrinsic detector resolution that has two main contributors:

$$\sigma^2 = \sigma_{\text{CPFA}}^2 + \sigma_{\text{meas}}^2; \quad (3.17)$$

$$\sigma_{\text{meas}}^2 = \sum_{i=1}^n \left(\frac{\partial x_{\text{rec}}}{\partial q_i} \right)^2 \Delta q_i^2; \quad (3.18)$$

$$\Delta q_i^2 = \sum_{\text{sources}} \sigma_j^2 = \sigma_{\text{noise}}^2 + \sigma_{\text{discr}}^2 + \sigma_{\text{non}}^2 + \sigma_{\text{thr}}^2 + \dots \quad (3.19)$$

Here, σ_{CPFA} is the error of the CPFA itself, σ_{meas} the error of the charge measurement. q_i is the measured charge in strip i , and index i denotes the strip number in the cluster of n strips and q_i the charge measured on strip i . Among other error sources of σ_j , there is detector noise σ_{noise} , charge discretisation σ_{discr} , non-uniformity of energy loss σ_{non} , threshold σ_{thr} , etc. The derivatives $\partial x_{\text{rec}}/\partial q_i$ in eq. (3.18) depend on the chosen Cluster Position Finding Algorithm (CPFA). I use the unbiased algorithm described in section 3.1.2. This yields for 1-strip clusters $\partial x_{\text{rec}}/\partial q = 0$, because the reconstructed position does not depend on the registered charge (see eq. (3.11)). For 2-strip cluster with fired strips i and $i + 1$ the derivative for eq. (3.12) is

$$\left| \frac{\partial x_{\text{rec}}}{\partial q_k} \right| = \frac{p}{3} \frac{q_i q_{i+1}}{\max(q_i, q_{i+1})^2} \frac{1}{q_k}, \quad k = i, i + 1. \quad (3.20)$$

Thus, eq. (3.18) for a 2-strip cluster can be rewritten as

$$\sigma_{\text{meas, 2s}} = \frac{p}{3 \max(q_i, q_{i+1})^2} \sqrt{q_i^2 \Delta q_{i+1}^2 + q_{i+1}^2 \Delta q_i^2}. \quad (3.21)$$

For bigger clusters, according to eq. (3.16),

$$\left| \frac{\partial x_{\text{rec}}}{\partial q_{i,j}} \right| = \frac{p}{2} \times \frac{1}{q};$$

$$\left| \frac{\partial x_{\text{rec}}}{\partial q} \right| = \frac{p}{2} \times \frac{|q_j - q_i|}{q^2}. \quad (3.22)$$

For the average charge, eq. (3.19) reads $\Delta q^2 = \frac{1}{n-2} \sum_{k=i+1}^{j-1} \Delta q_k^2$ and for each Δq_k^2 eq. (3.19) can be directly used. Thus, eq. (3.18) for an n-strip cluster reads

$$\sigma_{\text{meas, Ns}} = \frac{p}{2q} \sqrt{\Delta q_i^2 + \Delta q_j^2 + \frac{(q_i - q_j)^2}{q^2} \frac{1}{n-2} \sum_{k=i+1}^{j-1} \Delta q_k^2}. \quad (3.23)$$

3.3.2.2 ERROR OF THE CLUSTER POSITION FINDING ALGORITHM

To calculate σ_{CPFA} , I consider the simplest model of an ideal detector response: the charge distribution is proportional to the geometrical projection of an incident particle trajectory onto the readout plane. As an estimate of σ_{CPFA} , I use the dispersions calculated in section 3.1.2 for the unbiased CPFA. For different cluster sizes, these are

$$\sigma_{\text{CPFA, 1s}} = \frac{p}{\sqrt{24}}, \quad \sigma_{\text{CPFA, 2s}} = \frac{p}{\sqrt{72}} \left(\frac{|q_{i+1} - q_i|}{\max(q_i, q_{i+1})} \right), \quad \sigma_{\text{CPFA, Ns}} = 0. \quad (3.24)$$

3.3.2.3 ERROR DUE TO NON-UNIFORMITY OF ENERGY LOSS

An incident particle loses its energy non-uniformly when crossing a silicon sensor. If the trajectory of the particle is not perpendicular to the sensor plane, a multi-strip cluster can be created. In this case, the measured charge on each strip is not simply proportional to the respective trajectory projection. This makes an additional term to the error of the measured charge in eq. (3.19).

The contribution from the non-uniformity of the energy loss is difficult to take into account because both the actual energy loss and the path length of the incident particle within the sensor are not known. The following approximations, however, allow a straightforward solution:

- the energy loss is described with the Landau distribution, the most probable energy loss being [110]

$$\Delta_p = \xi \left[\ln \frac{2mc^2\beta^2\gamma^2}{I} + \ln \frac{\xi}{I} + j - \beta^2 - \delta(\beta\gamma) \right], \quad (3.25)$$

where $\xi = (K/2)\langle Z/A \rangle (x/\beta^2)$ MeV for a detector of thickness x (in g/cm²), Z and A the atomic number and the atomic mass of the absorber, $K = 0.307075$ MeV mol⁻¹ cm², $j = 0.200$, m the electron mass, $\delta(\beta\gamma)$ the density

correction, I the mean excitation energy, $\beta = v/c$ and $\gamma = (1 - \beta^2)^{-1/2}$ for an incident particle. Parameter ξ relates to FWHM with $w = 4.018\xi$ [111].

- the measured charge in a strip is the MPV (Δ_p) for the trajectory segment, which is projected onto this strip;
- the incident particle is ultrarelativistic. This assumption allows to relate uniquely the MPV and the distribution width ξ as [110]:

$$\Delta_p = \xi[\text{eV}] \times (\ln(1.057 \times 10^6 \xi[\text{eV}]) + 0.2), \quad (3.26)$$

The unique relation between the MPV and the Landau distribution width is not possible in general case because the energy of the incident particle is not known a priori.

Assuming the charge measured on the strip being the MPV, one can solve equation (3.26) with respect to ξ . Then, the half of the FWHM of the Landau distribution approximates the error due to the non-uniform energy loss:

$$\sigma_{\text{non}} = w/2 = 4.018\xi/2.$$

3.3.2.4 ADDITIONAL SOURCE OF ERRORS

The noise is modelled by the Gaussian (see chapter 2.2.2.3). The hit error due to the noise is, thus, well described with the same Gaussian width σ as it is used in the simulation that is equal to ENC.

Due to discretisation in the analogue-to-digital converter of the STS-XYTER chip, original information about the measured charge is lost. The STS-XYTER has 5-bit energy resolution (see section 1.4). The uncertainty from charge discretisation can be estimated as

$$\sigma_{\text{discr}} = \frac{Q_{\text{max}}}{\sqrt{12nADC}}, \quad (3.27)$$

where $nADC$ is the number of the ADC channels, Q_{max} the dynamic range.

3.3.3 HIT POSITION ERROR VERIFICATION

The analytic method for the hit position error estimation (presented in section 3.3.2) is an a-priori method that does not use any simulated data. Therefore, simulations can serve for the method verification. There are several verification measures that can be employed. The most natural one is pull distribution that is simulated residuals with respect to the simulated values normalised to the estimated errors (for hit position itself and for track parameters, such as coordinates and angles). Pull distributions characterise quality of the estimation of the diagonal elements of the covariance matrix. Another measure is the track χ^2 that strongly depends on the

estimation of the covariance matrix of tracks, which in its turn depends on the hit covariance matrix: both diagonal and nondiagonal elements.

Thousand minimum bias events of Au+Au collisions at 10 AGeV were simulated for the verification. For the track parameters estimation and particle reconstruction, the KF based track fit and the KF Particle Finder (both implemented in `cbmroot`) were used [98]. Only those effects were included into the simulation of the detector response, which are already accounted for by the hit position estimation procedure, namely: non-uniform energy loss of an incident particle within the sensor, noise, and charge discretisation in the readout chip.

3.3.3.1 HIT POSITION PULL DISTRIBUTION

Pull is a residual normalised to the estimated error: $\text{pull} = \text{residual}/\text{error}$. For a set of hits with an identical error estimate for each hit (for example, the set of all one strip clusters or the set of 2-strip clusters with the same charge ratio), the pull distribution is nothing but the residual distribution divided by a number. The pull shape, therefore, reproduces the residual shape. If the error is estimated correctly, pull distribution width (second central moment) is unity. The developed method of the estimation of the hit position error demonstrates all these features that is illustrated in fig. 3.15.

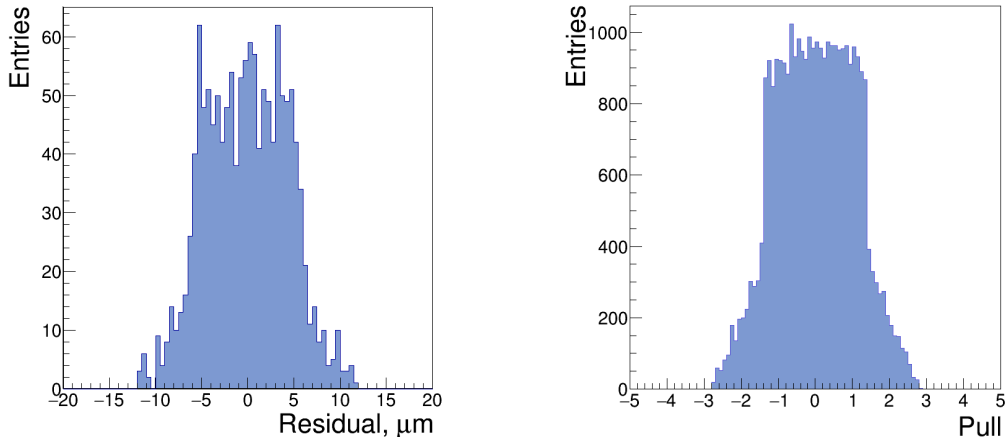


Figure 3.15: Residual distribution for 2-strip clusters at fixed charge ratio q_2/q_1 (*left*) and pull distribution for all 2-strip cluster (*right*). Pull distribution has a width close to unity and reproduces the shape of the residual. For both cases, the ideal detector response model and the uniform energy loss are used.

The width of the pull distribution of hits, simulated and reconstructed taking into account four physical effects one by one, is shown in fig. 3.16. Each of the four data points corresponding to the same label on the x-axis are obtained from the simulation, which accounts for the same processes as included in the determination of the cluster position error. For label “uni”, the error of CPFA for 3-strip and

bigger clusters is defined to be 0, and the residual is equal to the machine accuracy, thus, the pull is defined to be equal 1. For all cluster sizes and level of detail of the detector response (that increases along x-axis), the pull width is about unity that shows correctness of the developed method for estimation of the hit position error.

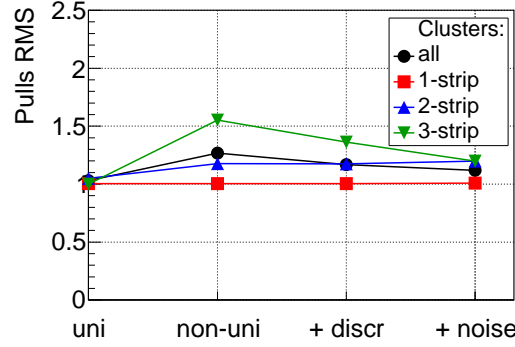


Figure 3.16: RMS of pull distribution when taking into account different physical effects one by one. See labels explanation in section 3.1.3.

3.3.3.2 TRACK RECONSTRUCTION

Parameters of the tracks reconstructed in the STS detector are estimated by the fitting procedure based on the Kalman filter (KF) method. The KF method uses the covariance matrix of the measurement to calculate the gain matrix, which is used to weight the influence of the measurement on the fitted parameters [112]. Thus, correct hit errors are extremely important for high quality estimation of the track parameters including both position and momentum. Moreover, such criterion as χ^2 for the reconstructed track is also strongly depends on the hit errors. In case of correct errors, this criterion is distributed according to the χ^2 -distribution and can be used for the selection of tracks.

Figure 3.17 shows the quality of the track reconstruction for both methods of the hit position error estimation: the simple one (it estimates the hit position error as $\text{pitch}/\sqrt{12}$) and the one developed in this work. Usage of the proper error estimate improves the precision of the track parameters determination: RMS of residual distributions for the coordinates become 5 – 10 % narrower, residuals for the angles stay the same, since they are mainly defined by the relative position of hits on a track.

Track pull distributions estimate correctness of the diagonal matrix of the covariance matrix. Figure 3.18 presents the pull distributions and their Gaussian fits for:

- x- and y-coordinates of a track at the last station in the track fitter procedure;
- track angle in x- and y-directions (t_x and t_y) at the last station.

Residual distributions

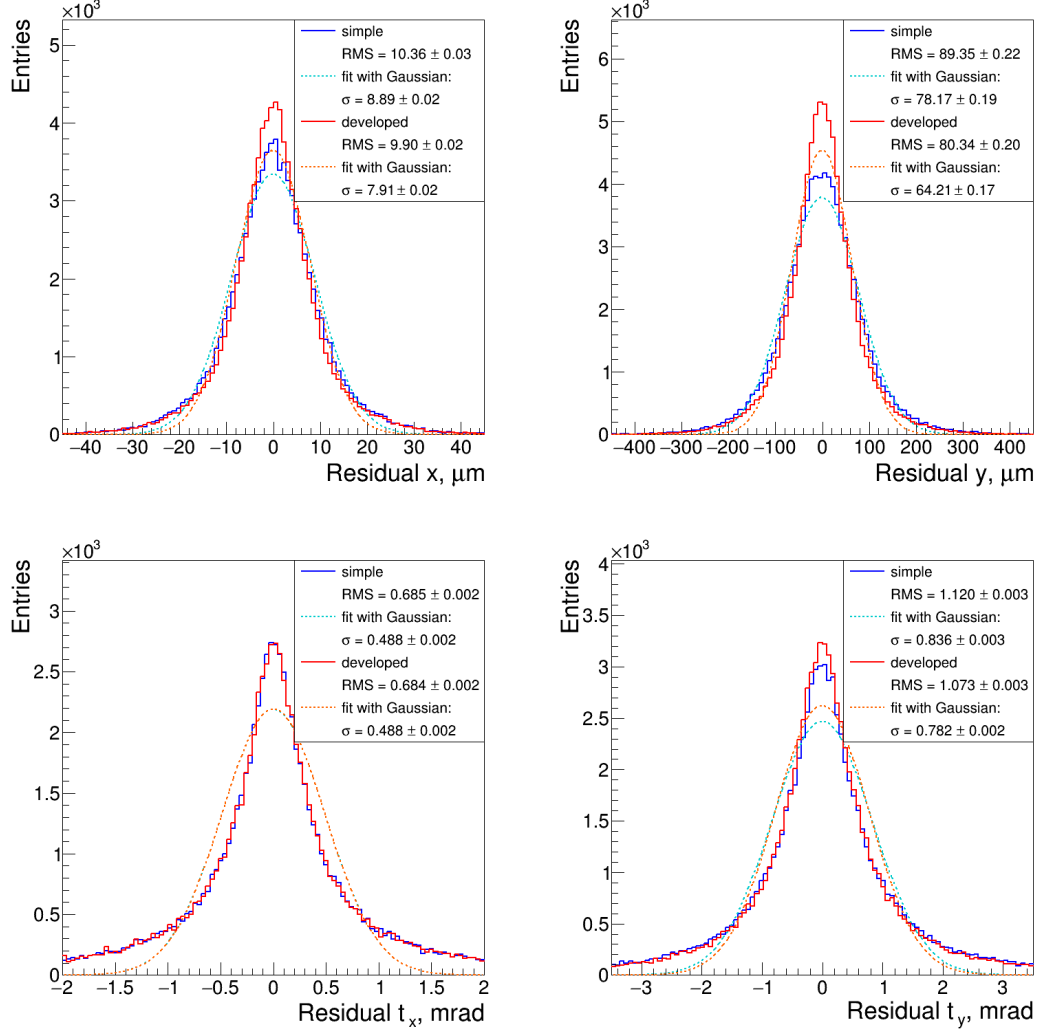


Figure 3.17: Residual distributions for x- and y-coordinates (*top-left* and *top-right*) of tracks and residual distributions for track angle in x- and y-directions (*bottom-left* and *bottom-right*) at the last station in the track fitter. The simple procedure of estimation of the hit position error (*blue*), the developed procedure (*red*) and their Gaussian fits (*cyan* and *orange*, respectively). RMS of the pull distributions and width of the Gaussian fit are given in the legends. Au+Au minimum bias collisions at 10 AGeV were simulated. The cbmroot framework was used for the simulation and the reconstruction.

Pull distributions

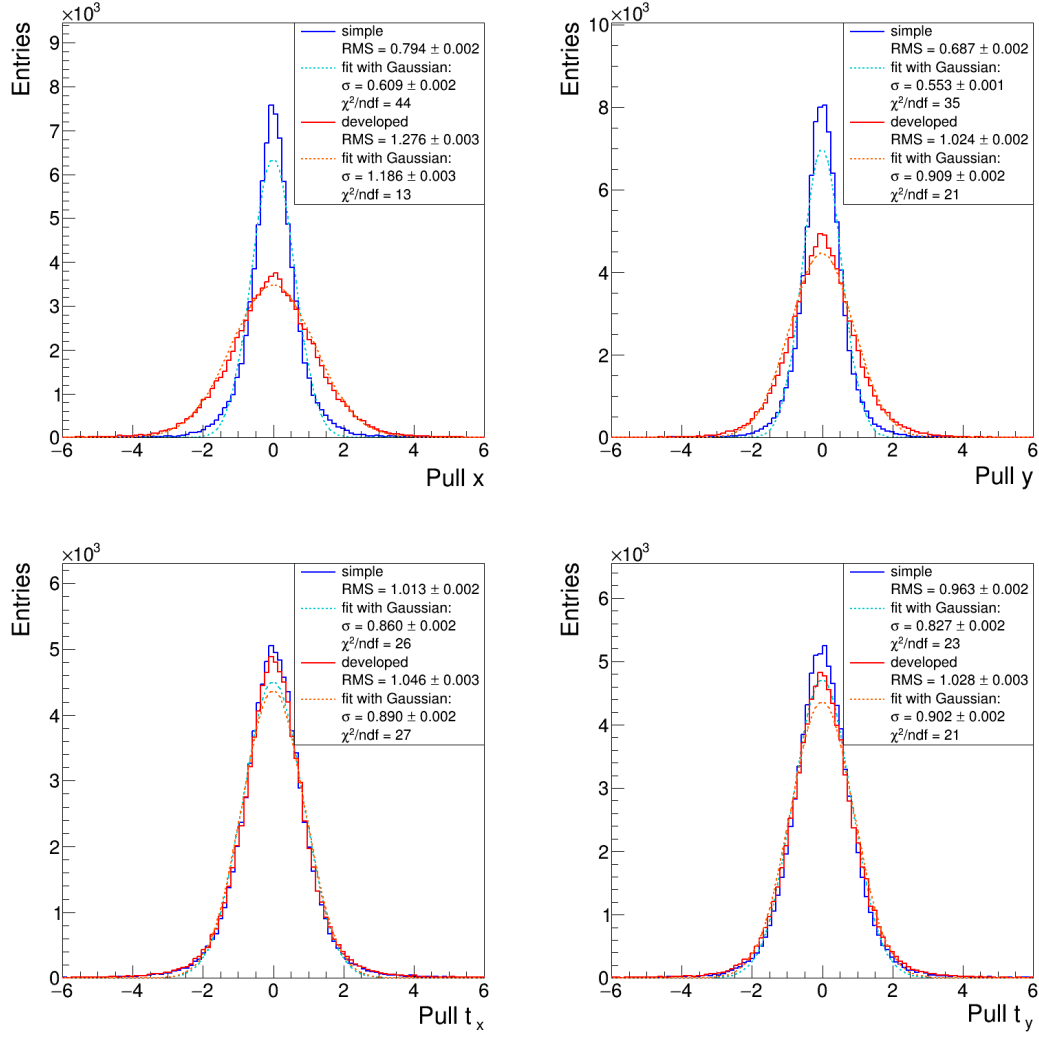


Figure 3.18: Pull distributions for x- and y-coordinates (*top-left* and *top-right*) of tracks and pull distributions for track angles in x- and y-directions (*bottom-left* and *bottom-right*) at the last station in the track fitter procedure. The simple procedure of estimation of the hit position error gives *blue* curves, its fit with the Gaussian is shown in *cyan*. The developed procedure gives *red* curves, its fit with the Gaussian — *orange*. In the legends, RMS of distributions, width of the Gaussian distribution, χ^2/ndf of the fit are mentioned. Au+Au minimum bias collisions at 10 AGeV were simulated. The cbmroot framework was used for the simulation and the reconstruction.

Using the developed procedure gives the following improvements in comparison with the simple procedure:

- RMS of the pull distributions are about unity;
- the pull distributions show better agreement with the Gaussian fit (χ^2/ndf of the fit are smaller). The pull distributions for the track parameters are expected to be Gaussian because there are many independent contributions to residuals of the track parameters and, thus, according to the central limit theorem, the residual distribution has the Gaussian shape. The total residual distributions shown in fig. 3.17 are an integral over the big ensemble of tracks with different parameters, thus, each of them is a sum of a big number of Gaussians with different widths. With the correct estimation of the covariance matrix, pulls are normalised to unity, thus an integral over the same ensemble of tracks should give a sum of standard normal distributions, that is a standard normal distribution. The obtained width of the Gaussian fit is also close to unity.

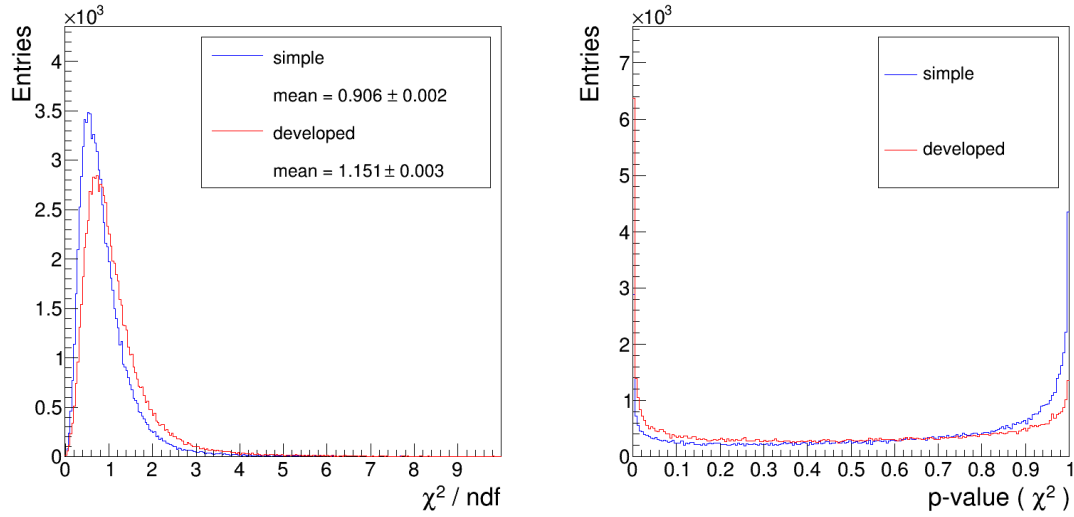


Figure 3.19: Track χ^2/ndf distribution (*left*) and p-value distribution (*right*) for all tracks from Au+Au minimum bias collisions at 10 AGeV. The cbmroot framework was used for the simulation and the reconstruction.

The χ^2/ndf of tracks and its p-value verifies the correctness not only of the diagonal elements of the track covariance matrix but the non-diagonal elements as well. P-value is defined as

$$\text{p-value} = 1 - \int_{-\infty}^{\chi^2} f(t) dt = 1 - \text{CDF},$$

with CDF being cumulative distribution function and f probability density function of χ^2 . P-value distribution is flat if the covariance matrix is well estimated [113].

Both, the simple and the developed, procedures of the estimation of the hit position errors yield the mean of the χ^2/ndf distribution to be about unity (see the left panel of fig. 3.19). The simple method underestimates the hit errors, that is reflected in smaller χ^2 values than expected according to the χ^2 -distribution and, as a result, p-value distribution tends to the higher values. The developed method results in more flat p-value distribution in comparison to the simple method (see the right panel of fig. 3.19). The peak at zero p-value is due to improper accounting for the multiple scattering in the detector material with Gaussian approximation [53, 112, 114].

3.3.3.3 PARTICLE RECONSTRUCTION

Tracks are used as input for reconstruction of short-lived particles. Thus, the estimate of hit errors through track parameters influences reconstruction of the most important physics observables of the CBM experiment.

Table 3.1: RMS of the residual and the pull distributions for the track parameters at the decay point of $J/\psi \rightarrow \mu^+\mu^-$.

Parameter	Method of the hit position error estimation:			
	simple		developed	
	residual	pull	residual	pull
x, cm	0.0113 ± 0.0001	1.035 ± 0.005	0.0114 ± 0.0001	1.139 ± 0.006
y, cm	0.0135 ± 0.0001	1.325 ± 0.006	0.0125 ± 0.0001	1.393 ± 0.007
z, cm	0.0438 ± 0.0002	0.689 ± 0.003	0.0419 ± 0.0002	0.987 ± 0.005
$p_x, \text{GeV}/c$	0.0290 ± 0.0001	1.296 ± 0.006	0.0295 ± 0.0002	1.403 ± 0.007
$p_y, \text{GeV}/c$	0.0276 ± 0.0001	0.980 ± 0.005	0.0283 ± 0.0001	1.113 ± 0.006
$p_z, \text{GeV}/c$	0.1320 ± 0.0006	1.469 ± 0.007	0.1342 ± 0.0007	1.488 ± 0.008
E, GeV	0.1374 ± 0.0007	1.449 ± 0.007	0.1393 ± 0.0007	1.464 ± 0.008
$M, \text{GeV}/c^2$	0.0407 ± 0.0002	1.347 ± 0.006	0.0419 ± 0.0002	1.351 ± 0.007

The simple method for calculating hit errors provides incorrect estimation, which is reflected in the covariance matrix of the reconstructed short-lived particles. Decay of $J/\psi \rightarrow \mu^+\mu^-$ can serve as an illustration [112, p.106]. Having a small lifetime, J/ψ decays in the region of the collision point at the target position. For its reconstruction, tracks are transported from the STS detector to the target that is at least 30 cm away. When transporting on such a big distance (comparing to the resolution of the detector), the diagonal elements of the covariance matrix, which correspond to the coordinates, are defined by the momentum errors. The momentum errors are defined mainly by the relative position of hits along the particle trajectory and

depend weakly on the hit errors. As a result, pulls of daughter tracks at the decay point and pulls of the reconstructed J/ψ particle have width close to unity. However, non-diagonal elements of the covariance matrices are affected by the incorrect hit errors and this leads to the underestimated χ^2 values of reconstructed J/ψ particles. The developed method for estimation of hit errors was applied in

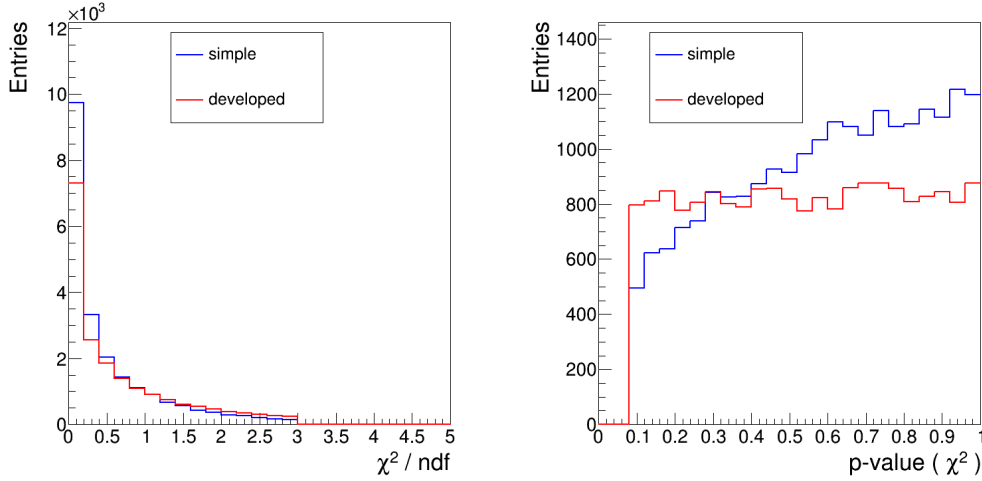


Figure 3.20: Track χ^2/ndf distribution (*left*) and p-value distribution (*right*) of tracks for $J/\psi \rightarrow \mu^+\mu^-$ expected in Au+Au minimum bias collisions at 10 AGeV. The cbmroot framework was used for the simulation and the reconstruction.

reconstruction of 10^5 J/ψ -mesons simulated according to the thermal distribution expected in Au+Au collisions at 10 AGeV and compared to the simple method. As shown in table 3.1, residuals and pulls obtained for $J/\psi \rightarrow \mu^+\mu^-$ reconstruction are similar in case of applying these two methods. However, the developed method allows to obtain correct estimation of the χ^2 value and flat distribution of the p-value, that is shown in fig. 3.20. Thus, obtained χ^2 -value behaves according to the χ^2 -distribution and can be used as the criterion for particle selection.

3.4 SUMMARY

The standard methods for cluster position reconstruction in the silicon microstrip detectors based on the Centre-of-Gravity algorithm gives biased estimate of position for some sets of clusters (for example see fig. 3.12). This adds the systematic error into the measurements, which, in its turn, complicates the procedure of the estimation of hit position. The new cluster position finding algorithm was developed based on the requirement to be unbiased. Being mathematically correct, it provides better resolution for each set of registered clusters (see section 3.1.2). Sources of uncertainties (such as noise, threshold, and others mentioned in fig. 3.13) worsen the position resolution such that the residual distribution alone does not favour the

unbiased algorithm over the Centre-of-Gravity (see section 3.1.3). However, the unbiased algorithm is computationally simpler and allows for an analytic estimate of the hit position error.

For correct estimation of the track parameters in such a low-material tracking system as STS, both terms in the error of parameters are significant: the multiple scattering and the detector intrinsic resolution (the hit position error). Also, a reliable estimate of the error effects the track χ^2 that is used to select correct track candidates and, as a result, affects the signal-to-background ratio of the reconstructed physical signals. The method to estimate the intrinsic resolution was developed (see section 3.3.2). It includes different independent sources of uncertainty, which are switchable: cluster position finding algorithm itself, non-uniform energy loss of incident particle, electronic noise, and discretisation of charge. The developed method requires as an input neither measured spatial resolution nor information about an incident particle track. It is an a priori method and employs only the measured charges at fired strips. Thus, the estimated error is a direct input for the track reconstruction algorithms.

The developed method of estimation of the hit position error yields correct errors, that was verified (see section 3.3.3) with:

- correct hit position pull distributions (width is about unity and shape represents the shape of the residual distribution);
- correct track covariance matrix calculated by the KF track fitter, which is confirmed with:
 - better quality of the track reconstruction (5 – 10 % narrower residual distributions for the track parameters);
 - correct pull distributions for the track parameters (the width is about unity and the shape has the Gaussian shape) that shows the correctness of the diagonal elements of the covariance matrix;
 - expected track χ^2/ndf distribution with the average value 1.151 ± 0.003 and flatter p-value distribution (in comparison with using $\text{pitch}/\sqrt{12}$ as an error estimate). This confirms the correctness of the estimation of the diagonal and the non-diagonal elements of the covariance matrix.

The developed method of the estimation of the hit position error improves the particle reconstruction: the p-value distribution for the reconstructed J/ψ particles, decaying into the $\mu^+\mu^-$ channel, is flat, unlike in [112, p.106], where $\text{pitch}/\sqrt{12}$ was used as a hit position error estimate.

Including of further sources of uncertainty is the next step in the method development. The threshold in the readout electronics is expected to have the most significant effect.

4

Evaluation of detector response in a relativistic proton beam

For evaluation of the performance, various tests of the prototypes of STS detector module were performed. The most comprehensive tests are the ones with a beam of minimum ionizing particles, which provides the best achievable approximation of the real experimental conditions.

The current chapter has the following structure: section 4.1 describes the experimental setups for the in-beam tests; section 4.2 presents the main results obtained during the in-beam tests; while section 4.3 provides the verification of the chosen detector response model described in section 2.2.2.

The in-beam tests performed at the COSY (COoling SYnchrotron) [115] accelerator in Jülich (Germany) in December 2013 and in December 2014 are of the highest relevance to this work. The experiments were performed by a collaborative effort of the STS and the GEM groups. For the STS group, the major goals of the experiments were: to characterise the latest detector prototypes. In December 2013, several module prototypes were tested: the sensors connected to the front-end electronics with a micro-cable. In December 2014, the overall performance of irradiated sensors and their radiation tolerance were evaluated.

4.1 EXPERIMENTAL SETUP

The experimental study of prototype modules was carried out in a proton beam extracted from COSY (COoling SYnchrotron) [115], Research Center Jülich (Germany). The experiments were performed in December 2013 and in December 2014

by a collaborative effort of the STS and the GEM groups. For the STS group, the major goal of the experiments was to characterise the latest detector prototypes. In December 2013, several module prototypes were tested having the sensors connected to the front-end electronics with a micro-cable. In December 2014, the overall performance of irradiated sensors was evaluated. The experimental setups of the in-beam tests in December 2013 and 2014 are in many respects similar. The schematic representation of the setups, along with the photographs, are shown in figs. 4.1 and 4.2 (2013 and 2014, respectively). The setups included the following detectors, aligned along the beam axis:

- scintillating fibre hodoscopes;
- reference STS stations: STS0 and STS1;
- STS detectors under test (different in 2013 and 2014): STS2 and STS3;
- GEM detectors.

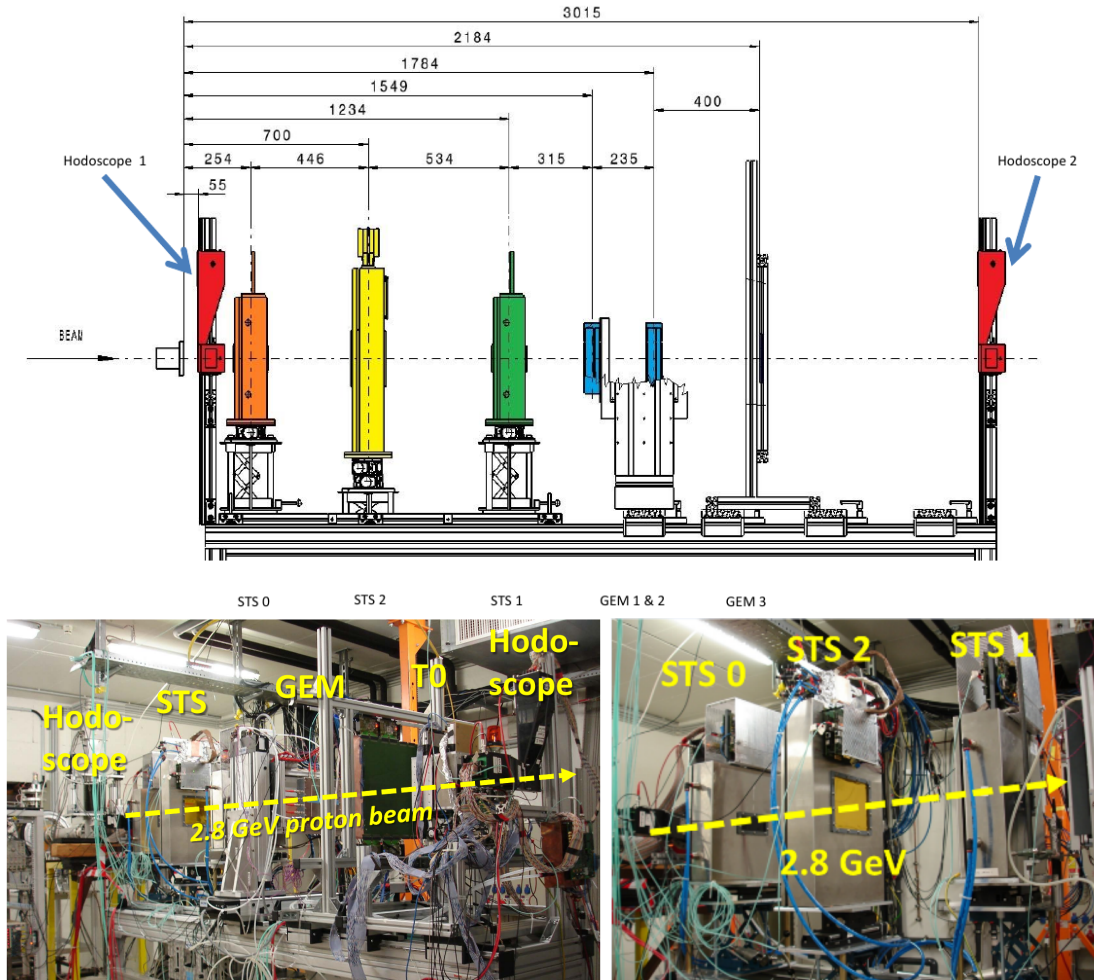


Figure 4.1: Setup of the in-beam test in 2013 at COSY: the geometry (*top*) and the photo of the whole setup (*bottom-left*) [116] and only the STS setup (*bottom-right*) [117, p.32].

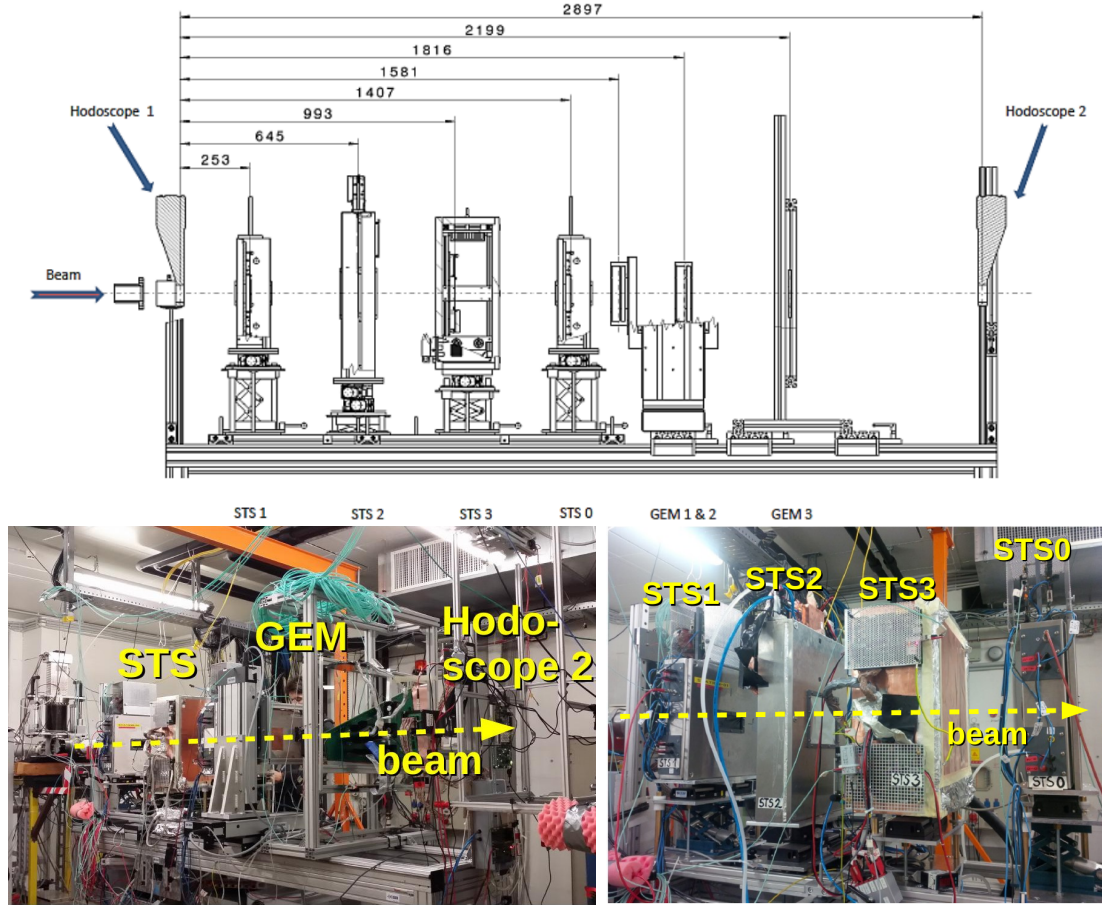


Figure 4.2: Setup of the in-beam test in 2014 at COSY: the geometry (*top*) and the photo (*bottom*) [51, p.8].

The COSY accelerator provided 2.8 GeV/c proton beam with adjustable intensities between $10^4 - 10^6 \text{ s}^{-1}$ and spill length 10 – 60 s. The fibre hodoscopes (built at Wuppertal University) provided a fast trigger signal for the detector under test and coarse spacial information [118]. Each hodoscope has 64×64 effective pixels, each pixel consists of 4 layers of optical fibres. The diameter of a fibre is 1 mm that provides spatial resolution of about 0.3 mm. The reference stations, STS0 and STS1, provided accurate spacial information about the track. They were based on miniature sensors of type CBM02 with size $1.5 \times 1.5 \text{ cm}^2$, strip pitch $50.7 \mu\text{m}$ and 90° stereo-angle (see fig. 4.3). The STS detector under test, STS2, hosted a module — a full-sized sensor ($6.2 \times 6.2 \text{ cm}^2$, $58 \mu\text{m}$ strip pitch, 7.5° stereo angle, type CBM05 from CiS [119]) connected to the readout electronics with a 30 cm long micro-cable.

Four prototype modules were involved in the beam tests (see fig. 4.4):

- M1: single sensor with the central part connected (tested in 2013);
- M2: single sensor with the edge strips connected (tested in 2014);

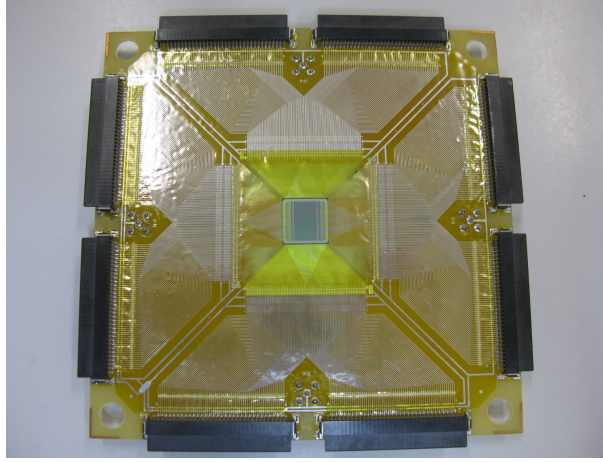


Figure 4.3: Baby sensor CBM02B2 fanned out on the flex-rigid board (micro-cable on the PCB carrier board). Such sensors were used in the references stations at the beam test in 2013 and 2014 [120].

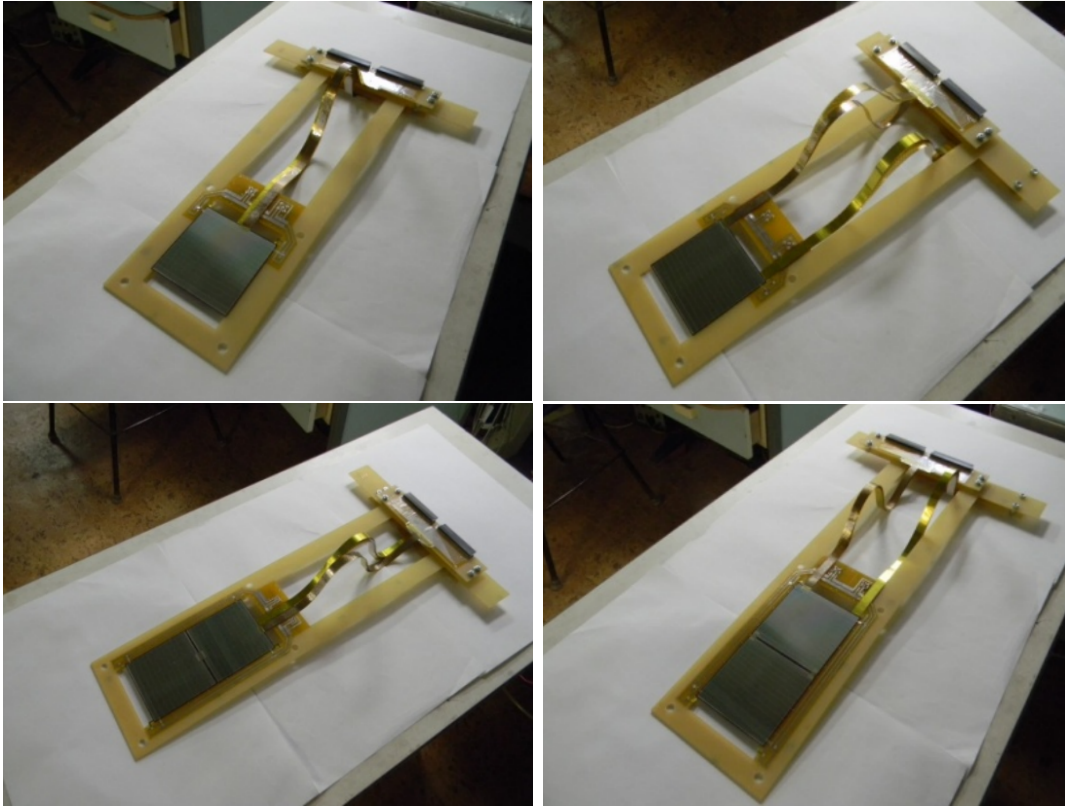


Figure 4.4: Modules tested during beamtimes. *Left-top* panel: module 1, single sensor $6.2 \times 6.2 \text{ cm}^2$, central strips connected to the micro-cable. *Right-top* panel: module 2, single sensor $6.2 \times 6.2 \text{ cm}^2$, edge strips connected to the micro-cable. *Left-bottom* panel: module 3, two daisy-chained sensors $6.2 \times 6.2 \text{ cm}^2$, central strips connected to the micro-cable. *Right-bottom* panel: module 4, two daisy-chained sensors $6.2 \times 6.2 \text{ cm}^2$, edge strips connected to the micro-cable [117].

- M3: two daisy-chained sensors with the central part connected (2013);
- M4: two daisy-chained sensors with the edge strips connected (2013).

STS2 was mounted on a rotatable table to study the sensor response at different inclination angles. Station STS3 was dedicated to the test of irradiated sensors. It was cooled down to -8°C with glycol circulating through the heat exchanger. The station was thermally insulated and pre-cooled nitrogen was constantly blown inside in order to decrease humidity and prevent condensation on the inner surfaces. Four sensors ($6.2 \times 4.2 \text{ cm}^2$, $58 \mu\text{m}$ strip pitch, 7.5° stereo-angle, type CBM05 from Hamamatsu [121]) were tested. Two of them had been irradiated at the KIT (Karlsruhe Institute of Technology) irradiation facility to $2 \times 10^{14} \text{ 1 MeV } n_{\text{eq}}/\text{cm}^2$ fluence before the beam test. This fluence corresponds to twice the integrated lifetime exposure expected for the innermost part of the tracker at the CBM running conditions [54].

Four sensors of two different types were under test (two sensors of each type: non-irradiated and irradiated):

- with integrated routing lines: a second metal layer made during detector fabrication (Double Metallisation, DM);
- with no routing line (Single Metallisation, SM).

In 2014, two stations under test were mounted on the beam table, but only one of them could be read out at a given time.

Because the STS-XYTER chip was still at design stage, our team used the front-end chips n-XYTER to read out sensors. The main STS-XYTER chip characteristics are expected to be inherited from those of n-XYTER. The chip is capable of measuring signal amplitude and arrival time. Originally, n-XYTER was developed for neutron detectors, but now it is used to read out silicon and gaseous detectors, and photo-multipliers in many projects. The chip has high rate capability, a bipolar front-end, and high gain. It can work in two modes: the self-triggering and the external-triggering mode. More details on the n-XYTER design and performance can be found in [59].

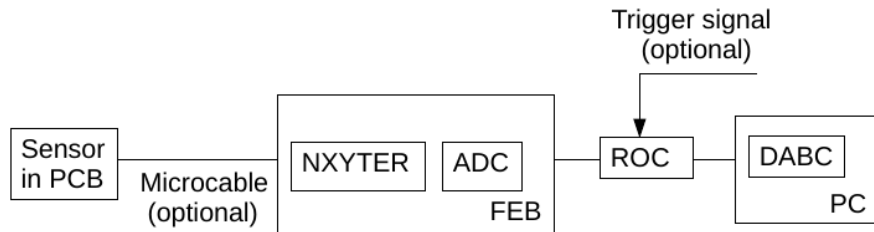


Figure 4.5: Scheme of the DAQ chain employed during the in-beam tests 2013 and 2014. Abbreviations are explained in the text.

The read-out chain, conceived for prototype detector tests, consists of the n-XYTER chip, an external 12-bit analog-to-digital converter chip ADC AD9228, placed on the same front-end board as the n-XYTER, and readout controller (ROC)

SysCore v2 (see fig. 4.5). The n-XYTER reads a current pulse directly from a sensor, and converts it to an amplified voltage pulse [122, p.53]. If the signal amplitude is higher than the reference value (threshold), the chip passes it to the analogue output, providing information of the time when the signal arrived. The ADC converts voltage signal into digital data. It is operated in 12-bit mode. Then, the ROC transfers the data to the PC. Also, it controls the functional behaviour of n-XYTER and ADC. The Data Acquisition Backbone Core (DABC) provides the data acquisition [123].

N-XYTER CALIBRATION. The charge calibration of the chip defines a charge conversion from electrons to the ADC LBS (“least significant bit”, it is equal to “ADC” value in sections 2.1.4 and 2.2.2.3). The calibration in [95, p.14], [78, 124] has been performed for the charge ranging from about 0.5 fC up to 30 fC. This calibration lacks an important region of yet lower charges, where non-linear effects can affect the noise interpretation. Because of this issue, the fit in this region is poorly constrained so that the input charge of 0 fC does not correspond to 0 LBS. This offset persists for a fit with a polynomial function of higher orders [78], the absolute value of the offset ranges in 0.1 – 0.4 fC depending on the signal polarity and the polynomial order (fig. 4.6, left panel). If the constraint 0 fC = 0 LBS is imposed, the fit does not reproduce the data in the region of low input charges (fig. 4.6, right panel).

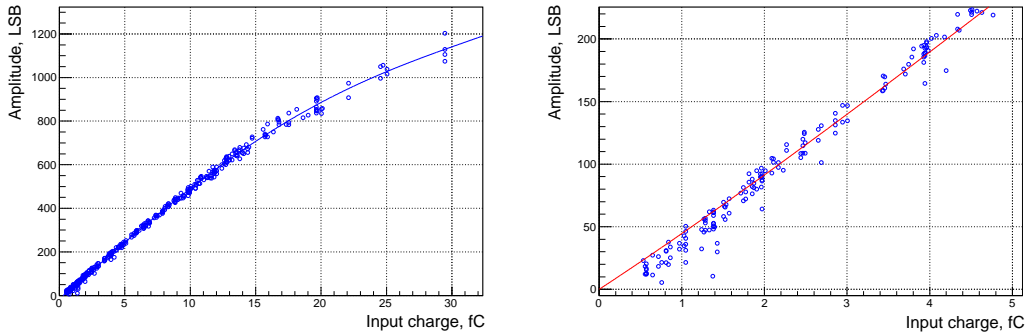


Figure 4.6: n-XYTER calibration results for both polarities [78]. Measured data are shown with markers and the line presents the fit. *Left:* fit with 4th order polynomial, *right:* fit with 4th order polynomial with the constraint: 0 fC = 0 LBS.

A decision was made to perform a new charge calibration with data points in the low charge region. This is only possible using the external-trigger mode in which case no threshold is applied. A procedure of calibration described in [78] requires a large effort: an external pulser, an attenuator and an external capacitor to convert a voltage step into a charge pulse were used; precise measurements of the capacitor value, coupling capacitance and the attenuation factor were performed.

n-XYTER chip has an internal pulser that can be used for calibration. The generated test pulse may be injected into every channel and the value of probe charge

is controlled via register *cal* (reg#24) [125]. The channel is additionally connected to its coupling capacitor of $C = 100$ fF. A voltage step is applied to the test capacitor that inducts the charge $Q = C\Delta V$. The step height may be programmed through reg#24 *cal* in a range from 0 to 1.137 V. To convert the register value into the injected charge, the DAC (Digital-to-Analogue Converter) gain is used. For positive test charges: $Q[C] = 44.63 \text{ aC} \times \text{reg24}$, for negative: $Q[C] = -44.55 \text{ aC} \times \text{reg24}$ [125].

The test pulse mode is not designed for the charge calibration, thus, the cross-check with the differently performed calibration [95, p.14], [78, 124] is necessary. Figure 4.7 shows a small difference between calibration results that were obtained with external and internal pulsers. This difference can be partially explained by different chips that were used for calibration.

Figure 4.8a compares calibrations using the self-trigger and external trigger mode. Although being done for different data sets, the fits are consistent with each other within the uncertainties of the fit parameters (see legends in fig. 4.8a). Figure 4.8b presents the calibration for one particular channel in the self-trigger mode for different thresholds. It shows that the calibration does not depend on the threshold. Thus, the calibration with internal pulser and the sophisticated calibration with external pulser both yield consistent fits.

The n-XYTER calibration with an internal pulser was done for the range from 0.05 to about 11 fC. Positive and negative polarity data were fitted separately because of a small difference in gain at high input charge (> 7 fC). A parabola was chosen for fitting the data. Higher order polynomials are redundant: χ^2/ndf improves by 4 % at most, but coefficients at higher orders get $\gtrsim 100$ % of uncertainty. Figure 4.8c compares fits with and without 0 fC = 0 LBS condition imposed. The difference in χ^2/ndf is not greater than 2 %. For a further analysis of experimental data in this work, the following calibration curves will be used:

$$\begin{aligned} A_- &= 51.37Q - 0.38Q^2, \\ Q_- &= 194.2 \times 10^{-4}A + 33.4 \times 10^{-7}A^2, \end{aligned} \quad (4.1)$$

$$\begin{aligned} A_+ &= 51.53Q - 0.62Q^2, \\ Q_+ &= 191.5 \times 10^{-4}A + 63.6 \times 10^{-7}A^2, \end{aligned} \quad (4.2)$$

where Q is charge in fC and A is amplitude in LBS. The uncertainties of measured charge, which originate from the calibration, can be estimated as:

$$\Delta Q_- = 1.1 \times 10^{-4}A + 2.5 \times 10^{-7}A^2, \quad (4.3)$$

$$\Delta Q_+ = 1.3 \times 10^{-4}A + 3.1 \times 10^{-7}A^2. \quad (4.4)$$

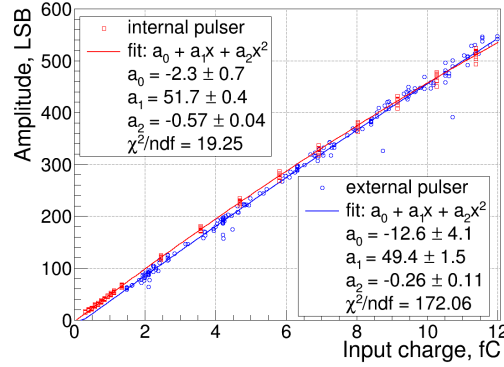
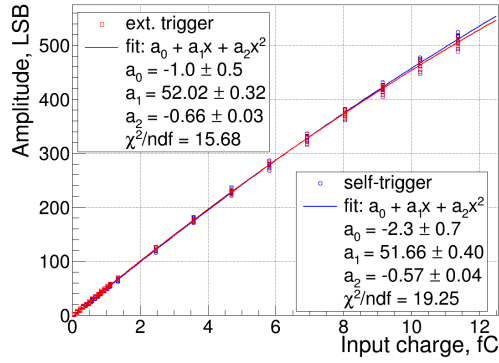
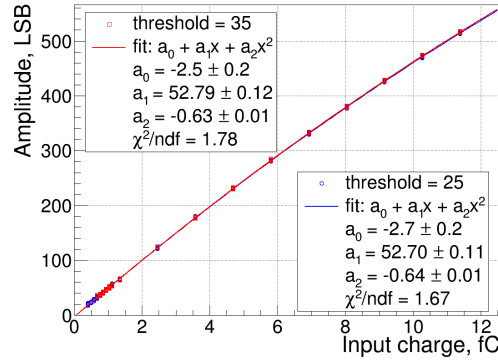


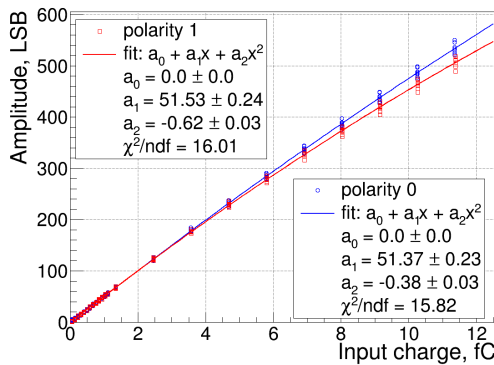
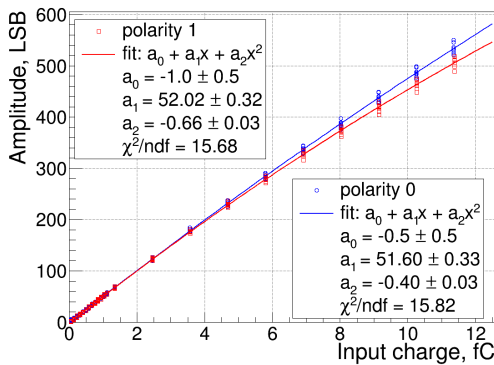
Figure 4.7: N-XYTER calibration in self-trigger mode: external (blue) [78] vs internal (red) pulser (the same value of the threshold and the signal polarity). The internal calibration is done for one particular chip, and external — for three other chips.



(a) Self-trigger (blue) vs external-trigger (red) modes (the same signal polarity and the same chip, several channels).



(b) Self-trigger mode with different thresholds: 25 (blue) and 35 (red) in register values (the same signal polarity and one particular channel).



(c) External-trigger mode for different polarities: positive (red) and negative (blue) (the same chip). Left: fit function: $a_0 + a_1x + a_2x^2$, right: $a_1x + a_2x^2$.

Figure 4.8: Calibration of the n-XYTER with the internal pulser. The markers present measured data and lines fits with parabolas.

4.2 BEAMTIME DATA ANALYSIS

During the in-beam tests, the data were collected in two modes of the n-XYTER chip: the self-triggered mode that reproduces the STS performance in the real experiment; and the external-triggered mode that allows the detailed studies of the detector performance. In the self-triggered mode, a level of the threshold was kept relatively high because in the accelerator hall, the noise level was much higher than in the laboratory. Therefore, for the data analysis, the data collected in the external-triggered mode were used. The front hodoscope (see the top panel of fig. 4.2) provided trigger signals. Then the logical signals were sent to the ROCs of each module as an “aux” input (auxiliary general purpose input).

EVENT SELECTION AND CORRECTION. To simplify the interpretation of data, an event selection and an event correction were done. At first, the baseline correction was applied. At the time of the in-beam test, the available version of n-XYTER (v1.0) was sensitive to temperature fluctuations. This issue was solved by performing the baseline calibration every 15 s during the data acquisition.

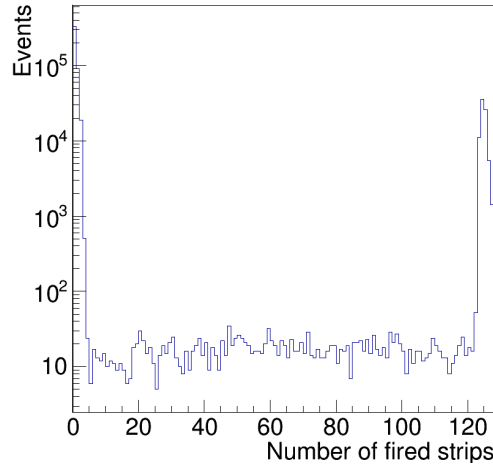


Figure 4.9: Number of fired strips at the p-side of module 2 per event.

An event was defined as a set of data within a time frame of 500 ns. Such a definition was chosen because it works for both the self- and the external-trigger modes. For beam rates of $10^4 - 10^6$ Hz, event overlap occurred rarely. Figure 4.9 displays typical distribution of the number of fired strips per trigger signal. This distribution has two distinct peaks at 0 and 125 and a relatively flat plateau in between. This indicates several types of events. Events with zero fired strips are events without data. The peak at 125th histogram bin can be explained by such events, in which signal from several channels are delayed. These delayed signals come later in time and create events with one-three channels fired (the peak at 2nd

histogram bin). Only the events with 120-127 fired strips were considered as “good” events and were included into the analysis. Some examples of the events are shown in fig. 4.10.

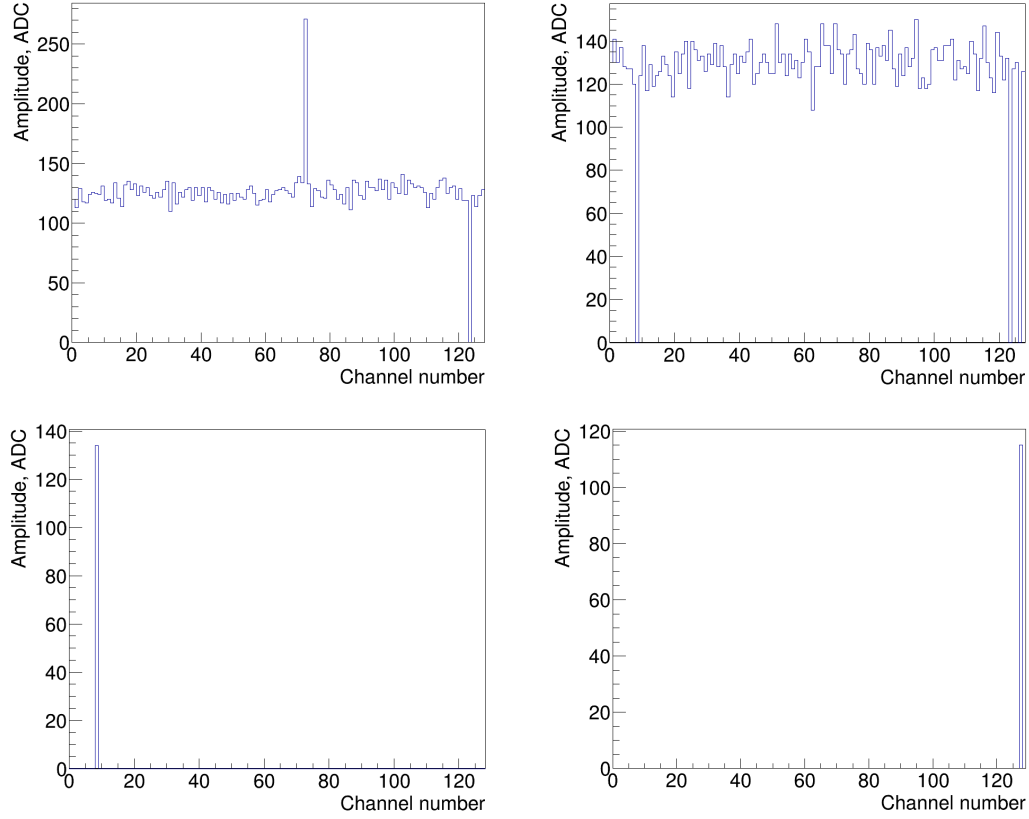


Figure 4.10: Types of events. P-side of module 2. Channel #124 is masked. For all plots, channel number is shown at the abscissas, and signal amplitude in ADC units at the ordinates. *Top-left:* “good” event with one particle penetrated the sensor. *Top-right:* “good” event with no particle, channels #9, 127 get no signal. *Bottom-left* and *bottom-right:* events with only one channel fired: these signals are delayed from the previous event shown in *top-right* panel.

To clean up cluster charge spectra, the common mode correction had been applied. For this procedure, all channels were used, excluding a channel with the maximum signal amplitude and its neighbouring channels, two from each side (these 5 channels were considered as possible channels with signal). The same set of non-signal channels was used to estimate the noise in each event.

To reject events with either no or several particles impinging onto the sensor in the same time frame, the events with only one cluster per reference sensor per side were selected for the analysis.

CLUSTER FINDER STRATEGY. To be combined into a cluster, digis have to pass certain selection criteria (see section 3.1 for more details about the cluster finders

in the STS).

The first approach is to compare the amplitude of the signal candidate to the noise level in the event. In each event, a channel with the maximum signal amplitude is a seed for the cluster candidate. The neighbouring channels are added to the cluster candidate if the signal amplitude exceeds $Q_{\text{digi}}^{\text{min}} = 3\sigma$ of the noise in this event. A cluster is introduced if the total cluster charge exceeds $Q_{\text{cl}}^{\text{min}} = 5\sigma$. This approach was used in the data analysis.

Another approach is to select a constant threshold $Q_{\text{digi}}^{\text{min}}$ for the amplitude of the digi to be added into the cluster and a constant threshold $Q_{\text{cl}}^{\text{min}}$ for the total cluster charge. This approach was employed for a comparison between simulated and experimental data. A typical baseline width for the modules was about 8 ADC. For a digi to be added to a cluster, a threshold of $Q_{\text{digi}}^{\text{min}} = 20$ ADC (2.5σ of noise) for the digi amplitude was applied. And for the minimum cluster charge, a threshold of $Q_{\text{cl}}^{\text{min}} = 90$ ADC was applied.

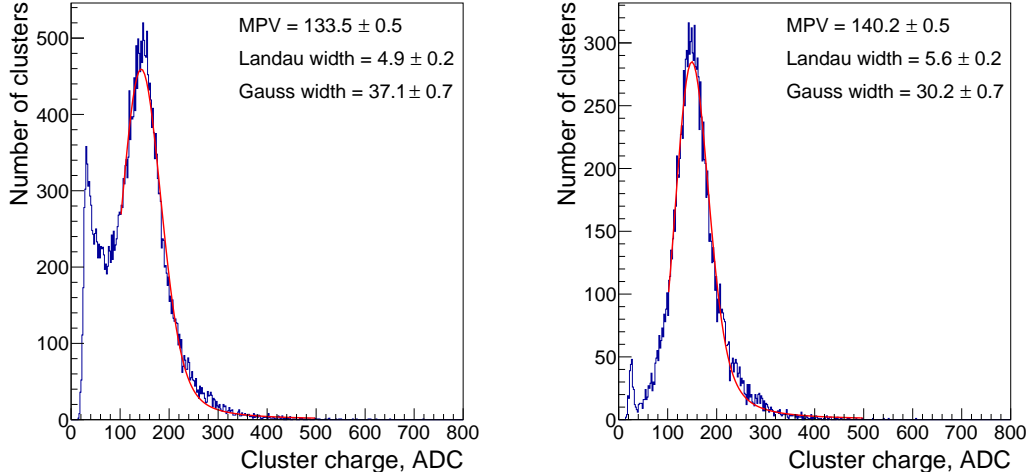


Figure 4.11: Distribution of 1-strip cluster charge in ADC units for the Hamamatsu double-metal irradiated sensor, n-side. *Left* panel: “open” clusters included into analysis. *Right* panel: “open” clusters removed from the analysis. Same cuts $Q_{\text{digi}}^{\text{min}} = 3\sigma$ and $Q_{\text{cl}}^{\text{min}} = 5\sigma$ were applied in both cases. “Open” clusters contribute to the noise region. Removing these clusters results in significantly cleaner distributions.

Some of the found clusters are “open” clusters. An “open” cluster is a cluster at the edge of connected strips area, thus the created charge carriers are only partially collected on the connected strips. Such clusters distort the cluster charge distribution, thus, they were removed from further analysis. Removing the “open” clusters yields significantly cleaner cluster amplitude distributions, especially if there are many unconnected or masked channels (see fig. E.1 in Appendix E for maps of connected and unmasked channels for sensors under the test). Figure 4.11 shows the influence of “open” clusters on the cluster charge distribution: they distort the shape of the distribution and affect the fitting parameters.

4.2.1 SIGNAL-TO-NOISE RATIO

The signal-to-noise ratio (S/N) is one of the key parameters for the evaluation of the detector performance. An estimation of this parameter requires the fully integrated system: the sensor, the micro-cable, and the readout electronics can interfere in a complex way leading to hardly predictable results. Since the STS-XYTER chip was not yet available for the data acquisition at that time, I decided to concentrate on the relative measurements. This way one can avoid some systematic effects, related to the readout electronics. An example of such measurements can be comparing the signal-to-noise ratio between irradiated and non-irradiated sensors, or between modules of different types.

In the simplest approach, a signal amplitude spectrum of a silicon sensor can be approximated with Landau-Gaussian convolution [111]. The typical cluster charge distribution of 1-strip clusters is shown in fig. 4.12. As an estimate of signal value I chose the most probable value of the Landau distribution. It was obtained by fitting a spectrum of signal amplitudes with selection criteria of $Q_{\text{digi}}^{\text{min}} = 3\sigma$ and $Q_{\text{cl}}^{\text{min}} = 5\sigma$ of noise.

Distributions for all sensors and modules can be found in figs. E.3 and E.8, Appendix E. The signal error bars include the statistical and the systematic errors. The systematic error was estimated with the variation of the thresholds $Q_{\text{digi}}^{\text{min}}$ and $Q_{\text{cl}}^{\text{min}}$, and comparing the resulting signal values. The distribution with selection criteria $Q_{\text{digi}}^{\text{min}} = 5\sigma$ and $Q_{\text{cl}}^{\text{min}} = 7\sigma$ can be found in figs. E.4 and E.9, Appendix E.

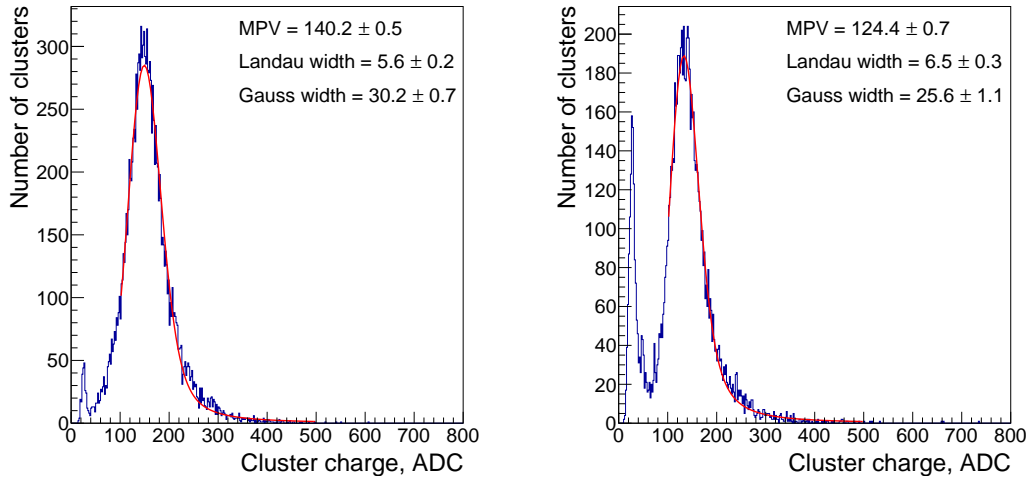


Figure 4.12: Distribution of 1-strip cluster charge in ADC units. Hamamatsu sensor with the second metal layer (DM), irradiated, n-side (*left*) and p-side (*right*). In the legends, the parameters of fit with the Landau-Gaussian convolution are mentioned.

The estimation on the noise contribution is performed in a multistep procedure:

1. perform the baseline correction;

2. omit the common mode correction, because the final readout will be employed in the self-trigger mode, where this correction is impossible to apply (the common mode correction reduces noise roughly by a factor of 2);
3. calculate the FWHM of the amplitude distribution for each connected not masked channel. Since the external trigger mode was used and connected not masked channel numbers were from 14 to 125, the amplitude distribution comprises mostly noise digis. Maps of channels for each tested sensor and module can be found in figs. E.1 and E.6 in Appendix E. The distribution of half width at half maximum ($1/2$ FWHM) was plotted;
4. estimate the noise value as mean value of the $1/2$ FWHM distribution;
5. calculate the error of the noise as the RMS of this distribution.

Distribution of $1/2$ FWHM for all sensors and modules can be found in figs. E.2 and E.7, Appendix E.

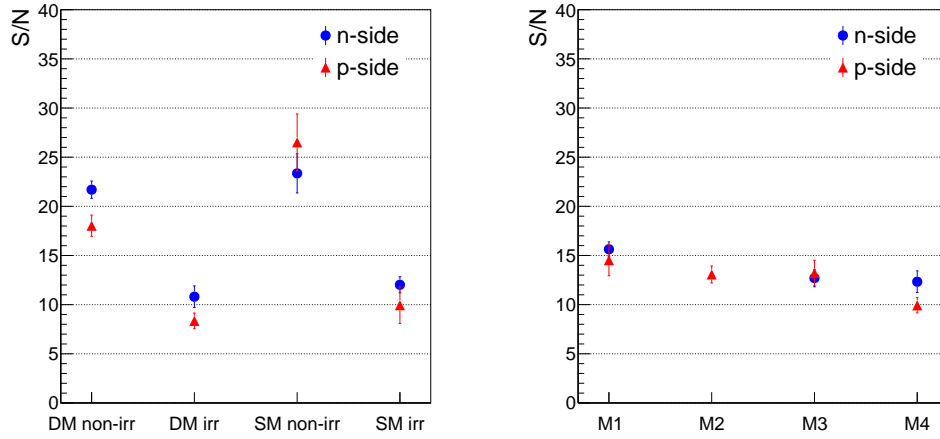


Figure 4.13: Signal-to-noise ratios for all the Hamamatsu sensors in PCBs (*left* panel) and for all the modules, which contains CiS DM sensor (*right* panel). Labels on the abscissas present the type of the sensor or the module. DM denotes the double-metal sensor technology, and SM single-metal.

The obtained values for the noise and for the signal were converted from ADC units to charge units (ke) using the calibration relations presented in section 4.1. Signal-to-noise ratios were calculated for all sensors and modules (see fig. 4.13). For all modules, the obtained ratio stays within 10 – 16.

The bias voltage of 101 V applied for the measurements of M2, though higher than the full depletion voltage 80 V, was insufficient for the complete charge collection [78]. Hence, an interpretation of results for M2 is not trivial. Additionally, there were only 10 readout channels connected to the n-side, thus, the number of events was quite low for signal fitting procedure to extract the signal value (see the second-top left panel of fig. E.8). All other modules were measured at 140 V.

Two daisy-chained sensors (M3) have the ratio of about 10 – 20 % lower than one sensor (M1), which is mainly because of the lower signal obtained (see fig. E.10, Appendix E). Comparison of p-sides of M3 and M4 shows the effect of the second metal layer. The signal in the channels, which are connected to the edge strips of the p-side and are connected to the second metal layer (green lines in fig. 3.2), is lower and the noise is higher than in the channels, which are connected to the central strips of p-side and have no connection to the second metal layer. That leads to a lower S/N: 13.2 ± 1.3 and 9.9 ± 0.8 for M3 and M4 respectively. The difference in S/N for the n-side of M3 and M4 is within the uncertainties: 12.7 ± 0.9 and 12.3 ± 1.1 . A more detailed study of the effect of the second metal layer requires one sensor to have edge and middle strips connected to one read-out chip to access their simultaneous measurement.

Non-irradiated Hamamatsu sensors have higher S/N in comparison to modules that comprise CiS sensors. This is explained by the direct connection of the Hamamatsu sensors to the PCB (no signal reduction in the micro-cable), and by their larger thickness (more charge is created in the sensor bulk). For non-irradiated sensors, the signal-to-noise ratios obtained for the n-side of the DM and the SM sensors are consistent with each other: 21.7 ± 0.9 and 23.3 ± 2.0 , respectively. This is expected because the structure of the n-side is the same for each sensor technology. On the p-side, the SM sensor shows higher S/N ratio (26.5 ± 2.9) in comparison to the DM sensor (18.0 ± 1.1). The higher value for one particular SM sensor does not yet favour the single-metal technology in general. More sensors are to be tested for the robust results. After irradiation to the double lifetime dose for operation at SIS300, the signal-to-noise ratio drops to about 10 (see section 4.2.2 for more details).

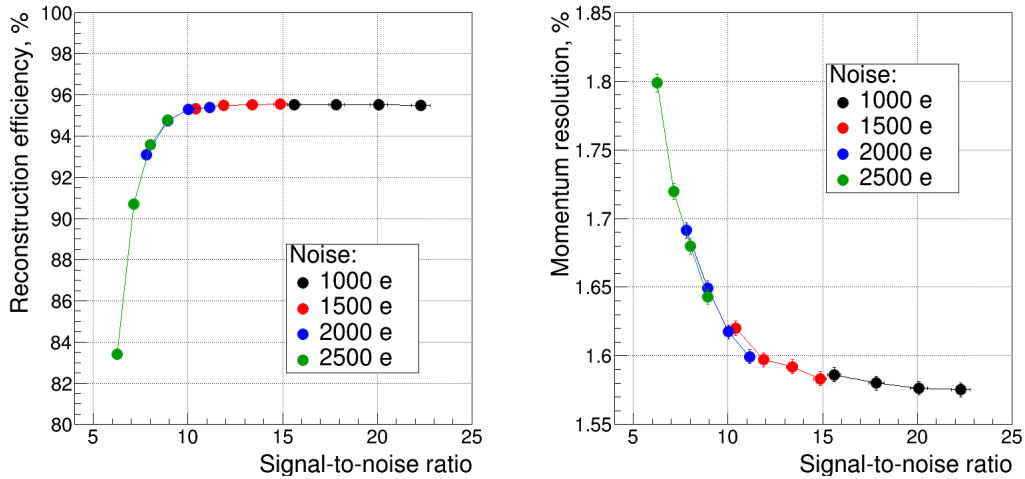


Figure 4.14: Track reconstruction efficiency (*left*) and momentum resolution (*right*) for fast tracks ($p > 1$ GeV) at different S/N values (Au+Au collisions at 10 AGeV simulated with cbmroot). Vertical error bars represent statistic uncertainty, horizontal — precision of the signal definition (see text).

To evaluate whether the obtained value of S/N is sufficient, simulations are required. Here, I present the first simulations of the STS performance, which were done for different values of S/N set uniformly for all the sensors of the STS. Because the threshold was always set to 3 ENC and the performance depends on the threshold value, simulations were done for different values of noise: 1000 e, 1500 e, 2000 e, and 2500 e. The MPV of 1-strip cluster charge created by a MIP defines the signal, its value is $22300 \pm 500 \text{ e}^1$. Different values of S/N at the same noise level were achieved by varying of the CCE from 100 % to 70 %. The STS performance at different S/N is presented in fig. 4.14. The reconstruction efficiency stays the same ($95.4 \pm 0.1 \%$) for S/N more than 10 but at lower S/N significantly deteriorates: down to 83 % at S/N = 6. The momentum resolution has even stronger dependence on the signal-to-noise ratio: it degrades slowly already with the S/N decreasing from 22 to 10 and show more pronounced degradation when S/N becomes less than 10. Thus, S/N should be more than 10 to maintain the track reconstruction quality sufficient for the physics analysis.

4.2.2 RADIATION HARDNESS OF THE SENSORS

After irradiation, a deterioration of the sensor performance is expected. The obtained signal-to-noise ratios for the sensors irradiated to $2 \times 10^{14} \text{ 1 MeV } n_{\text{eq}}/\text{cm}^2$ are shown in the left panel of fig. 4.13 (see section 4.2.1). The drop of the signal-to-noise ratio is mainly due to the noise increase by 50 – 75 %, while the signal itself drops by 17 – 27 % (see fig. 4.15).

To evaluate whether such a radiation hardness is sufficient, I perform a simulation of the irradiated sensors. The first simplistic simulations, presented here, set the charge collection efficiency and the noise level uniformly for all sensors in the STS. This simplification does not reflect the real particle fluence distribution. Under the real experiment conditions, the highest dose will be achieved only in the innermost part of the stations. Thus, such an estimate of the STS performance can be considered as a conservative estimate for the STS overall performance. The track reconstruction efficiency and the momentum resolution obtained with these simulations are presented in fig. 4.16. The reconstruction efficiency does not depend on the charge collection efficiency (CCE) if the noise level is sufficiently low (below 1500 e). However, it degrades even at 100 % CCE if the noise level increases to 3000 e (from $95.5 \pm 0.1 \%$ at 1000 e to $91.9 \pm 0.1 \%$ at 3000 e). This effect can be explained by the partial signal cutoff with the hardware threshold; it is always set to 3σ of the noise

¹2 GeV protons crossing the STS perpendicularly were simulated with `cbmroot`. Such a particle and its energy were chosen in order to reproduce the conditions during the in-beam tests. The obtained signal value was $22300 \pm 500 \text{ e}$. This simulation included all the effects implemented in the realistic detector response model (see section 2.2.2) but does not include detailed effect of the parasitic capacitances (see section 2.2.2.3). As shown in Appendix F, the parasitic capacitances (of the sensor and the micro-cable) effectively reduce signal by 10 – 18 % depending on the micro-cable length.

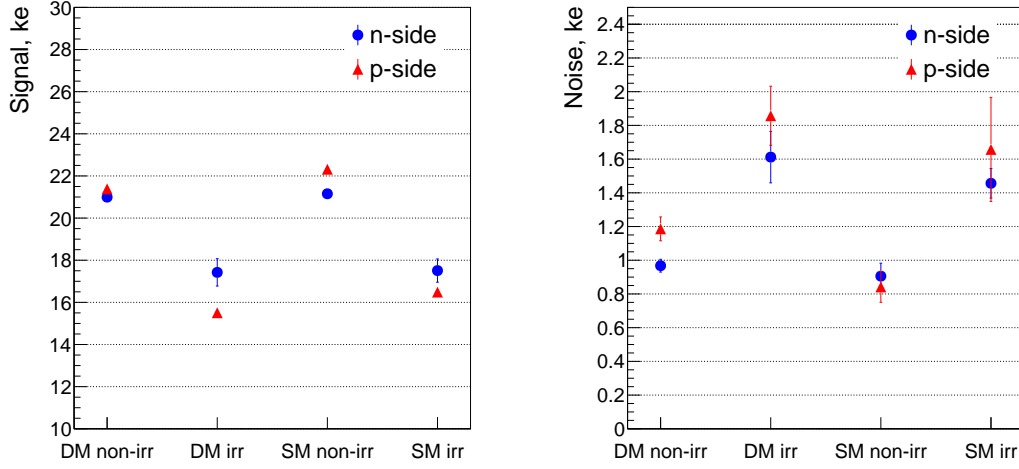


Figure 4.15: Signal (*left*) and noise (*right*) for the Hamamatsu sensors. Labels on the abscissas represent the type of the sensor.

in the present simulations. Higher threshold, thus, worsens the hit reconstruction efficiency, which results in a decrease of the track reconstruction efficiency. Hence, the noise level is the key quantity that defines the STS performance.

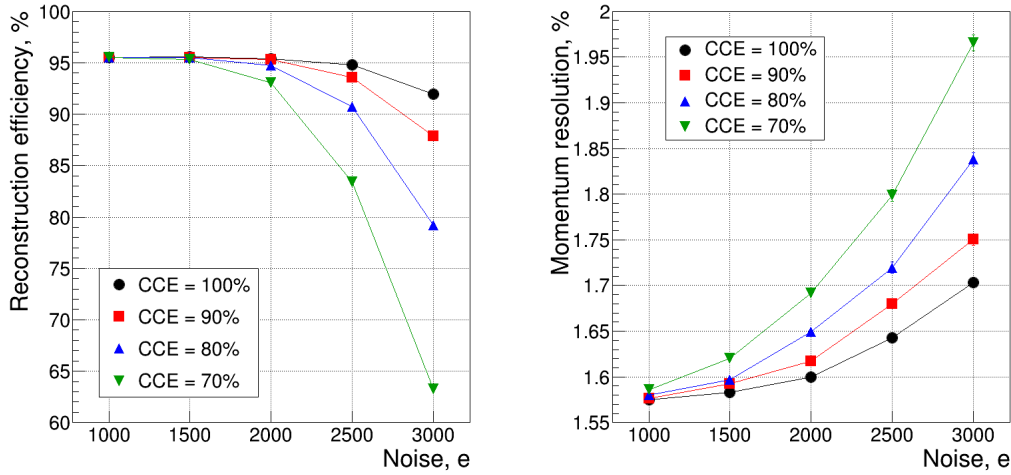


Figure 4.16: Reconstruction efficiency and momentum resolution for fast tracks ($p > 1$ GeV). Simulation with different values of charge collection efficiency (CCE, the values are given in the legends) and noise (on the abscissas).

During the in-beam test, the CCE was found to degrade down to 80%² and the noise level — to increase to about 2000 e for the irradiated sensors. The parasitic capacitances of the micro-cables effectively worsen the CCE further (see Appendix F). The STS performance, taking into account micro-cables and irradiation effects, can

²100% CCE is defined as the charge obtained with the non-irradiated sensor

be estimated using the simulation with 70 % of the CCE and 2000 e of the noise. For these values, the reconstruction efficiency decreases from 95.5 ± 0.1 % to 93.2 ± 0.1 % and the momentum resolution degrades from 1.58 ± 0.01 % to 1.69 ± 0.01 %.

Regarding the results of the simulations given above, I do not expect any significant degradation of the tracking quality if the initial noise level of the system with non-irradiated sensors does not exceed 1000 e. A performance simulation with a detailed map of irradiation dose is required. As an input for such a simulation, measurements of the CCE and the noise should be done for intermediate doses.

4.3 VERIFICATION OF THE DETECTOR RESPONSE MODEL

The ultimate verification of a simulation is its comparison against experimental data. The verification of the realistic detector response model (see section 2.2.2 for the model description) and comparison with the simple model are presented below.

The data from the proton beam tests are used because the monochromatic well-focused beam of MIPs facilitates the comparison with the detector response model. To favour one of the detector response models, it was important to minimise the threshold during the data acquisition. Otherwise, the difference between simulated results obtained with different detector response models will vanish due to the imposed threshold. Thus, the data collected in the external-trigger mode were used. Two modules (tested at the beamtimes in 2013 and 2014, see section 4.1) were chosen for the verification. Module M1 with the simplest construction (see the left-top panel of fig. 4.4) was tested in 2013 with different incidence angles of the proton beam. The bias voltage applied to the sensor was 140 V, which allowed to operate the sensor in the over-depleted mode. At that time, there were no precise angle adjustment tools available: an uncertainty of the angle reached 3° for these tests leading to the additional systematic uncertainty in data. In December 2014, a set of tests was performed with module M2 (see the right-top panel of fig. 4.4). M2 was tested at different angles with the angle uncertainty of about 0.5° . The initial angle alignment was performed manually, with the uncertainty of 2° . Due to technical reasons, the bias voltage was only 101 V, making the complete charge collection impossible, especially for the n-side of the sensor [78].

The event selection procedure and the event correction, described in section 4.2, were applied to the data. As a cluster finding strategy, the second approach (described in section 4.2) was used, namely, constant thresholds were selected for the amplitude of the digi to be added into the cluster and for the total cluster charge. A typical baseline width during the in-beam measurements was about 8 ADC. For the digi amplitude to be added into a cluster, a threshold of the $Q_{\text{digi}}^{\text{min}} = 20$ ADC (2.5σ of noise) was applied. And for the minimum cluster charge, the threshold of $Q_{\text{cl}}^{\text{min}} = 90$ ADC was applied (the most probable cluster charge for a MIP is about 125 ADC). Although stringent, such selection criteria have the same impact on the cluster size distribution and the cluster charge in both the experimental data and

the numerical modelling. Therefore for the verification of the method it is sufficient that the value of the threshold in the simulations is the same as for the experimental data.

The proton beam was simulated with the Gaussian distribution of the polar angle with the central value of 0 and the variation of $\pm 1^\circ$.

I compare two different detector response models against the experimental data. The two models are:

1. simple model that includes only the uniform energy loss, the noise, and the threshold;
2. realistic model that additionally accounts for the non-uniform energy loss, the diffusion, and the cross-talk.

Both models were adjusted for the comparison with the in-beam test data as follows:

- The noise was simulated for all connected channels in each event because the data were obtained with the n-XYTER chip in the external-trigger mode.
- The actual map of dead, unconnected, masked strips/channels was taken into account for each module under the test.
- The measured charge calibration of n-XYTER chip (see section 4.1) was used.
- Signal decrease due to the trigger delay of 50 ns was estimated as 5 % [126, p.25] and implemented in simulations.
- No hardware threshold was applied for the signal, but the same software thresholds as for the experimental data were used in the simulation for cluster building.

The realistic model, additionally, includes the sophisticated analysis of the cross-talk effect described in section 2.2.2.3, which accounts for the parasitic capacitances.

The cluster size distribution is sensitive to the charge sharing effects. This observable was chosen for the comparison. Figure 4.17 shows the cluster size distributions for the p-side at different incidence angle obtained with module 2 during the in-beam test in 2014. The cluster size distribution for the n-side obtained with module 1 during the in-beam test in 2013 can be found in Appendix E.

To analyse the results, it is convenient to divide them into the following categories:

- Perpendicular tracks. If there is no charge sharing, all the clusters are 1-strip clusters. Presence of the noise leads to small fraction of 2-strip clusters. This is represented by the simple detector response model (*blue* points in the *top-left* panel of fig. 4.17). Such effects as the diffusion and the cross-talk increase the cluster size. Since they are included into the realistic response model (*red* points), it appears that the number of 1-strip clusters decreases. But there is still difference between the realistic model and the data. It can be explained by the noise modelling: in the simulation noise is assumed to have a Gaussian shape with the same width for all the channels. In a real module, the noise shape in each channel can be described with the Gaussian only in the first

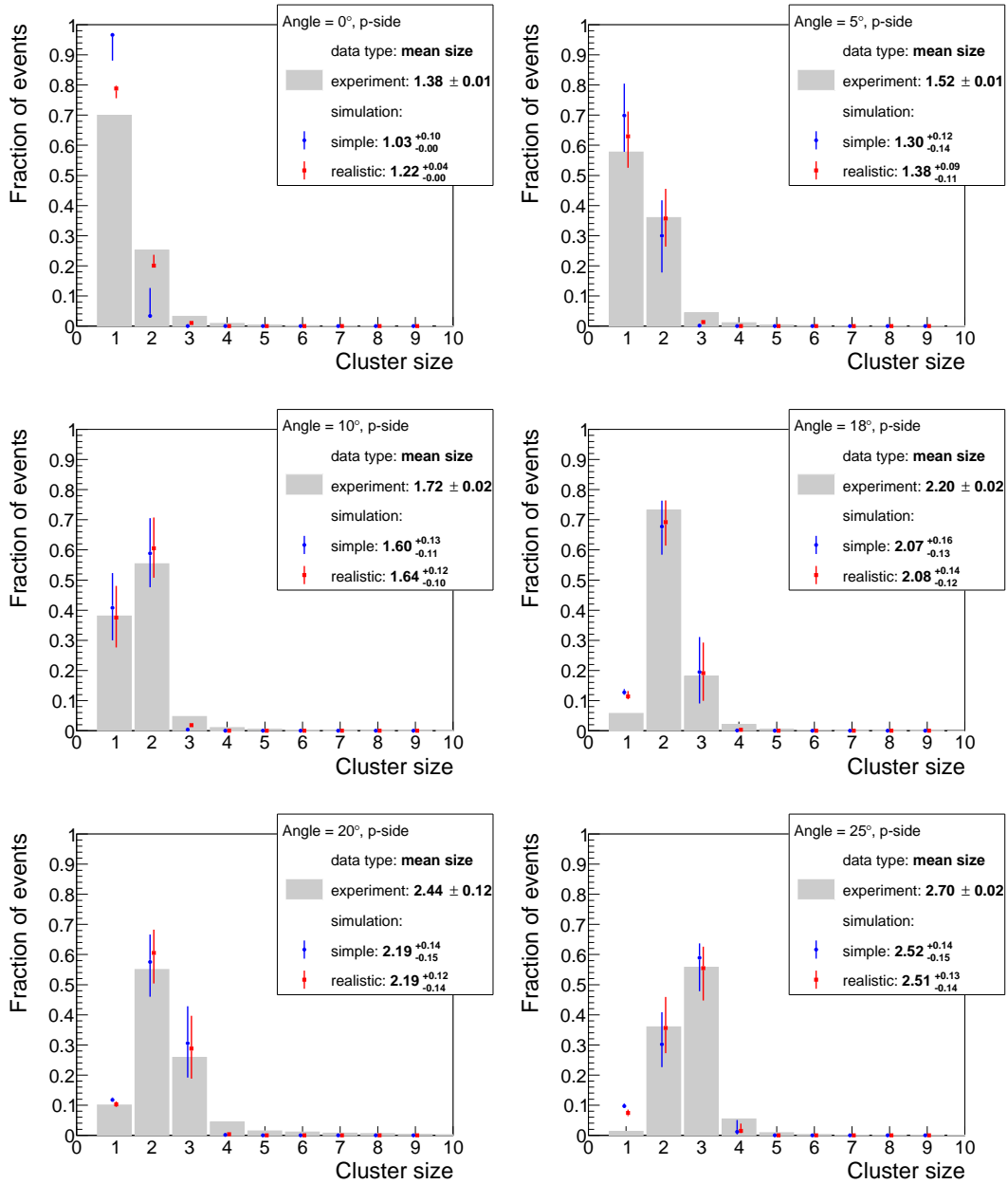


Figure 4.17: Cluster size distributions for different incidence angles on the p-side of the sensor (module 2). Experimental (grey filled histograms) and simulated data with two models: simple (blue points) and realistic (red). The average cluster sizes are in the legends. Error bars include statistical errors, uncertainty of the incidence angle measurement, capacitance variation and capacitance measurement error. Statistical errors for the experimental data are not shown because they are negligible (except the *bottom-left* panel).

approximation; moreover, the width of the Gaussian varies from channel to channel. Furthermore, some events are more noisy than the others: FWHM of the noise distribution is larger. All these effects lead to a larger fraction of two-strip clusters at expense of one-strip clusters.

- Slightly inclined tracks ($< 10^\circ$). Even without charge sharing, fraction of 1-strip clusters is only about 70 % (*blue* points, for 5° see the *top-right* panel of fig. 4.17). Charge sharing effects lead to even lower amount of 1-strip clusters of about 63 % (*red* points, for 5° see the *top-right* panel). Two-strip clusters are caused partially by the track inclination and the noise (this is represented by the simple model) and, additionally, by charge sharing effects (the realistic model). Three-strip clusters cannot be the result of the track inclination for the track angle $< 10^\circ$ (see fig. 4.18). They are rarely caused by the cross-talk: the absolute value of a signal in each channel of a two-strip cluster, in most cases, is not enough to create the signal in a neighbouring channel that overcomes the threshold $Q_{\text{digi}}^{\text{min}}$. Thus, the difference between the data and the simulation with the realistic model can be explained in the same way, as the difference for two-strip clusters in case of perpendicular tracks, namely, imperfect noise description in the simulation. Thus, some of the one-strip clusters become two-strip clusters (by incorporating a neighbouring noisy channel into a cluster) and some two-strip clusters become three-strip clusters: this leads to the overestimation of the amount of one-strip clusters and the underestimation of the amount of three-strip ones.
- Heavily inclined tracks ($\geq 10^\circ$). The track inclination is already so large that the minimal cluster size is two, three, or even four strips (depending on the angle, see fig. 4.18). Smaller clusters are created due to the fluctuations that stochastically decrease the charge in one of the fired channels. The resulting charge in this channel may become smaller than the threshold $Q_{\text{digi}}^{\text{min}}$. Thus, there is mainly overestimation of the amount of small clusters in both the simple and the realistic simulations, which account for the noise in the simplistic way. The difference between two models almost vanishes, because the cross-talk already does not play a significant role in creation of larger clusters: absolute values of signal in each channel of a multi-strip cluster are mostly insufficient to create a signal in the neighbouring channel that overcomes the $Q_{\text{digi}}^{\text{min}}$.

Figure 4.19 summarises the cluster size distributions and shows the mean cluster size depending on the track inclination angle for two different modules and sensor sides. From the presented results, one can see that the experimental data favour the realistic detector response model against the simple one. The analysis of the simulation parameters shows that accounting for the parasitic capacitances (the cross-talk) is the main reason for the better agreement of the cluster size distributions.

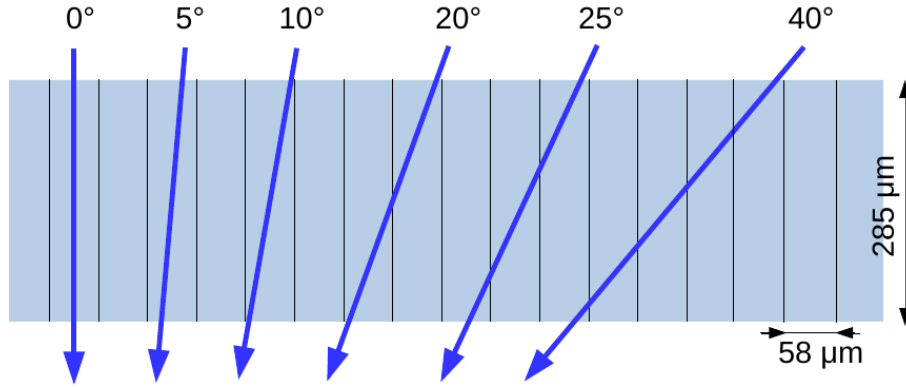


Figure 4.18: Schematic view of particle tracks (*blue arrows*), which cross the sensor at different angles. Sensor thickness and strip pitch are shown in the proper scale.

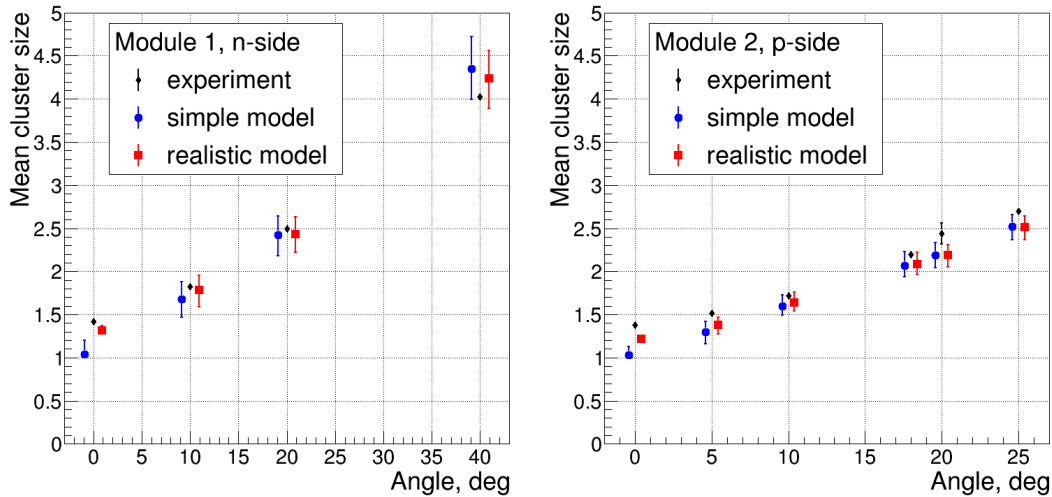


Figure 4.19: Mean cluster size versus incidence angles for the n-side (*left*) and for the p-side (*right*). Experimental data (*black markers*) and simulation with two models: the simple (*blue*) and the realistic (*red*). Error bars for the simulations include statistical errors, uncertainty of the angle measurement, capacitance variation and capacitance measurement error. Experimental data include only statistical error, and corresponding error bars are smaller than the marker size.

ERROR ESTIMATION. It is non-trivial task to estimate the influence of systematic uncertainties of the measured distributions. Therefore, the systematic errors are included into the simulations. The simulations accounted for the uncertainty of the measurements of the incident angle and the error due to the strip-by-strip capacitance variation and the capacitance measurement uncertainties (see section 2.2.2.3 for the values). Systematic errors from different sources (angle and capacitances) and the statistical error were treated as independent uncertainties and therefore added quadratically.

To estimate the error introduced by the angle measurement, two additional cluster size distributions are simulated for angle values $\alpha + \Delta\alpha$ and $\alpha - \Delta\alpha$ with $\Delta\alpha$ being the error of the angle measurement. The value in each bin of the cluster size is compared with the central value, obtained in the simulation with angle α . The positive difference between the central bin value at α and the bin value at $\alpha \pm \Delta\alpha$ is considered as a positive error, and the negative difference as a negative one. If both differences have the same sign (for example, plus), the asymmetric error for the bin value is assigned: the maximum of both differences is taken as an error in one direction (positive), and in another direction (negative) the zero error is set.

The error due to uncertainty of capacitance measurement and its channel-by-channel variations was estimated in a similar way as the error due to the angle measurement. Uncertainties of the interstrip, the coupling, the bulk, the cable, and the CSA capacitance are considered to be independent. The cluster size distributions are simulated at the fixed central values for every capacitance except one. For example, values for the interstrip, the coupling, the bulk, and the CSA capacitances are fixed at the central values of each and the cluster size distribution is simulated for $C_{\text{cable}} \pm \Delta C_{\text{cable}}$. Then, the positive and the negative errors due to C_{cable} are estimated in the same way as for the angle error. For each capacitance, the positive and the negative error is calculated and added quadratically to form a total positive and negative error (respectively) introduced by all the capacitance uncertainties.

The errors for the simulated value of the mean cluster size were calculated in the same way as the error for each bin in the cluster size distributions. The error of the mean cluster size obtained in the experiment contains only statistical error.

4.4 SUMMARY

During the in-beam test in December 2013 and December 2014, performance of the STS prototypes was studied. The measurements of the full-sized module prototypes probe the performance of the whole module made of 30 cm long micro-cable and of either one or two daisy-chained $6.2 \times 6.2 \text{ cm}^2$ CiS sensors. The measurements of the irradiated $6.2 \times 4.2 \text{ cm}^2$ Hamamatsu sensors probe the performance of the sensors connected to the readout electronics without any micro-cable.

The signal-to-noise ratios (S/N) for all the tested modules, which comprise CiS sensors, give S/N from 10 to 15 (see section 4.2.1). This is sufficient for the track reconstruction with high efficiency ($> 95\%$) and high momentum resolution ($< 1.6\%$). But one has to take into account that the irradiation will deteriorate the sensor performance.

Radiation hardness of the Hamamatsu sensors was studied (see section 4.2.2 for details). For the module configuration during the in-beam test (the sensor mounted in the PCB was connected to the n-XYTER readout chip through ERNI connec-

tors), the charge collection efficiency (CCE)³ drops to 83% for the n-side and to 75% for the p-side, and the noise increases by 50 – 75% after irradiation to 2×10^{14} 1 MeV $n_{\text{eq}}/\text{cm}^2$ (this value corresponds to the double lifetime fluence expected for the CBM operation at SIS300). The first simulation shows that if all the sensors in the STS setup are exposed to such a fluence, the track reconstruction efficiency drops from 95.5% to 93.2% and the momentum resolution degrades from 1.6% to 1.7%. These values were obtained with the an assumption that the micro-cables decrease the CCE by 10% uniformly for all the STS modules (see Appendix F). This estimate can be considered as the lower limit of the STS performance.

The simulation of the STS performance reveals that the reconstruction quality strongly depends on the detector S/N. Since there is no way to increase the signal at fixed sensor thickness, main effort should be put into the noise reduction and decreasing of the charge loss in the micro-cables. Detailed simulation with proper values of the dose and the micro-cable length for different modules of the STS is required to assure the reliable performance quality.

The detector response model described in section 2.2.2 was verified against the experimental data. Based on the obtained results, one can see that the experimental data favours the realistic detector response model (with additional accounting for the parasitic capacitances) against the simple one, which is more idealistic. This leads to the necessity of detailed measurements of the parasitic capacitances, which, together with the noise value, should be later put in the database for different flavors of modules. This way they can be involved into the proper detector response simulations.

³100% CCE is defined as charge measured with the non-irradiated sensor of the same type: SM or DM.

5

Summary and conclusions

Within this work, a realistic detector response model for a double-sided microstrip detector was designed, implemented, and verified against the experimental data. The verification shows significantly improved agreement in comparison to the previous simple detector response model that does not include charge sharing effects (see section 4.3). The detector response model has an influence on the detector performance, which is deteriorated by several effects. Some of those are difficult to measure and to disentangle from other effects (for example, diffusion or non-uniformity of the energy loss). Such effects must be included into a model based not only on the measurements but also on their impact on the detector performance. The simulation shows that both the diffusion and the cross-talk enlarge the detector occupancy and the cluster size. Both non-uniformity of the energy loss and the electronics noise worsen the spatial resolution (see section 2.2.2.4). The previous simple model overestimates the detector performance compared to the realistic model by the following factors:

- the digi pile-up effect is underestimated by a factor of 1.8;
- the average detector occupancy is underestimated by a factor of 1.05;
- the hit position resolution in the bending plane is overestimated by $5\,\mu\text{m}$ for clusters of size 3 and more strips;
- the rate of fake hits is underestimated by a factor of 1.1.

On the other hand, the track reconstruction quality, which is mainly defined by the geometry (reconstruction efficiency) and the multiple scattering (momentum resolution), is not affected by the choice of detector response model.

A reliable detector response model can be used to study precision performance of the STS. The developed unbiased cluster position finding algorithm is mathe-

matically correct and gives smaller residuals than the Centre-Of-Gravity algorithm. However, sources of uncertainties like noise, threshold etc. worsen the position resolution such that the residual distribution alone does not favour the unbiased algorithm over the Centre-Of-Gravity (see section 3.1.3). Still, the developed cluster position finding algorithm is computationally simpler and allows for an analytic estimate of the hit position error.

Within this work, an analytic method to estimate the hit position error was developed. The estimated errors are used as input for the Kalman Filter based track fitter, and result in correct fit of the track parameters. The developed method requires as input neither measured spatial resolution nor information about the incident particle track. It includes different independent sources of uncertainty, which are switchable: the cluster position finding algorithm itself, the non-uniform energy loss of incident particle, the electronic noise, and the discretisation of charge. The developed method of estimation of the hit position error yields correct errors, which was verified using the realistic detector response model (see section 3.3.3). The method improves the track reconstruction: residual distributions for the track parameters become 5 – 10 % narrower. The p-value distribution for J/ψ particles (decaying into the $\mu^+\mu^-$ channel), which is sensitive to the hit errors, becomes flat (unlike in [112, p.106]). The next step in the development of the method is to include further sources of uncertainty. The threshold in the readout electronics is expected to be the next significant effect.

The realistic detector response model was used for investigating the detector performance for different cases. It allowed the study of the STS as a particle identification detector involving measurements of the energy loss in the sensor [101]. Also, using the realistic model, the STS performance was tested under different conditions: after irradiation (see section 4.2.2), at high noise level, with some strips/chips/modules being not read out [99], with sensors of different thickness [100]. The first simplistic simulation with the signal-to-noise ratio set uniformly for each module of the STS setup shows that the signal-to-noise ratio should be larger than 10 to achieve an efficiency of track reconstruction larger than 95 % and a momentum resolution of smaller than 1.6 % (see section 4.2.1).

In-beam measurements show, that the non-irradiated prototype modules with a micro-cable length of 30 cm (the average length in the whole STS setup) provide a sufficiently high signal-to-noise ratio between 10 and 15. The sensors irradiated with the double lifetime dose and connected to the readout electronics through the ERNI connectors also give signal-to-noise ratio of about 10. Two possibilities to increase the signal-to-noise ratio for modules are the noise reduction and the signal enhancing. The signal can be increased by decreasing either the micro-cable capacitance or the parasitic capacitances of the sensor, or better both. Adding the micro cable (version of the year 2016) causes an additional signal loss by up to 11 % (see Appendix F). Noise reduction is of high importance for the STS because at a noise level more than 2000 e (which has been measured for the irradiated sensors so far) the signal-to-noise

ratio does not reach the value of 10. Thus, detailed measurements of the parasitic capacitances of the latest sensor and micro-cable versions are required. The results of these measurements have to be stored in the database for the modules in order to be used for proper detector response simulations. The measured values of signal loss and noise for different modules, and the realistic distribution of the accumulated fluence over the whole STS have to be included into the detector simulation for reliable estimate of the STS performance.



Additional plots for comparison of the detector response models

Figures A.1 and A.2 present the simulated occupancy of the STS in detail. They show the fraction of readout channels occupied in one event. Two different detector response models were used: the simple one and the realistic one. The detailed description of the simulation can be found in section 2.3.

Residual distributions obtained using the simple and the realistic detector response models are shown in fig. A.3.

Channel occupancy: simple model

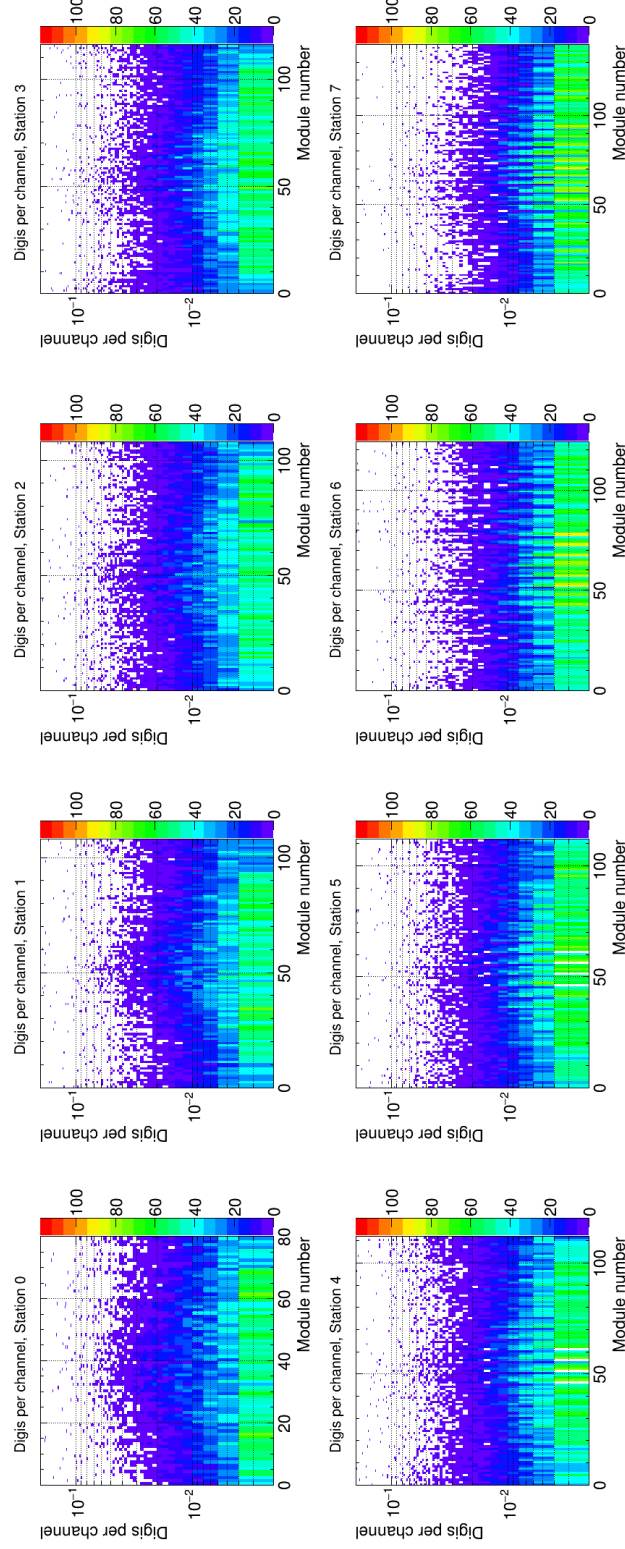


Figure A.1: Occupancy per readout channel. Different panels present stations, each module within a station corresponds to one x-bin. The simple detector response model.

Channel occupancy: realistic model

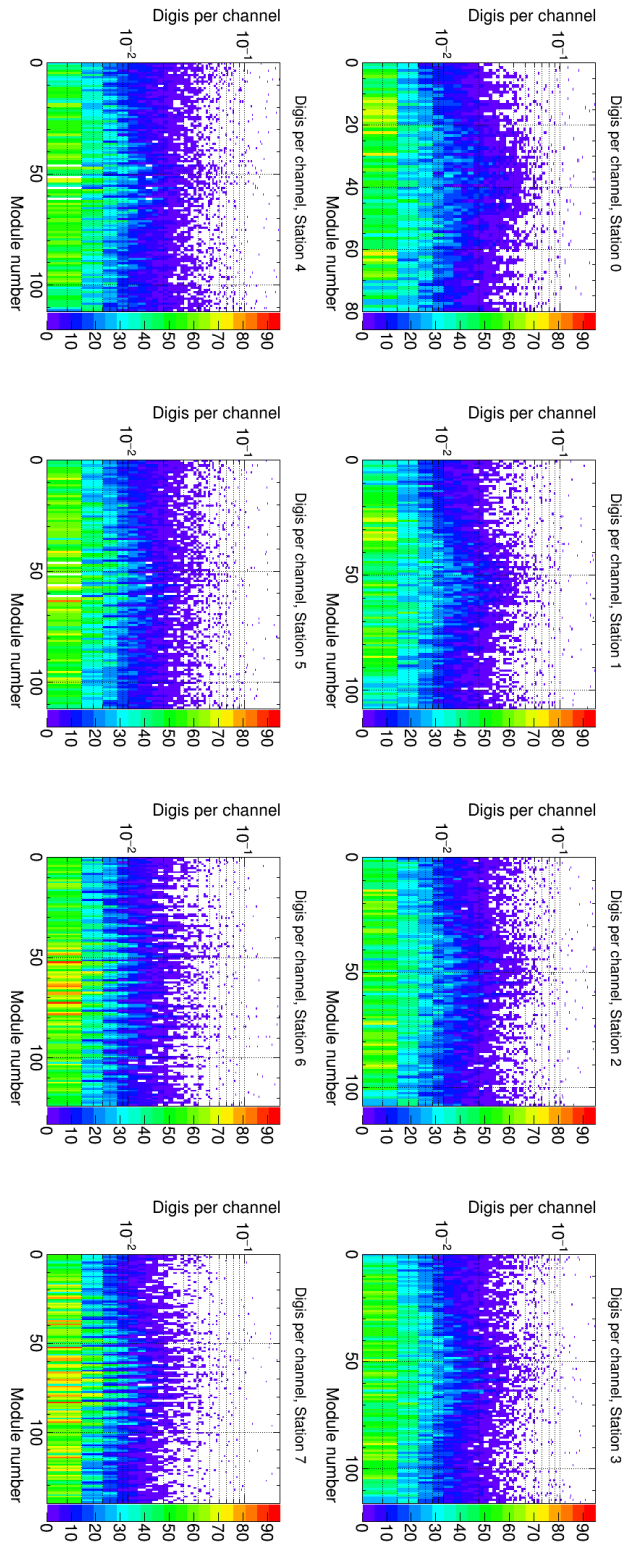
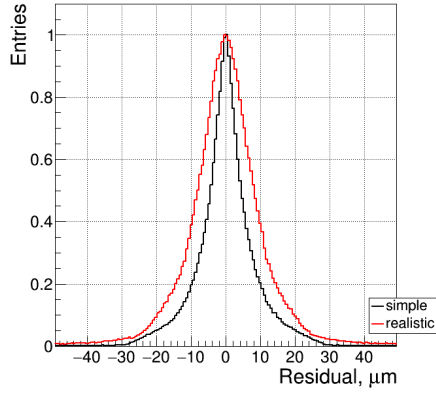
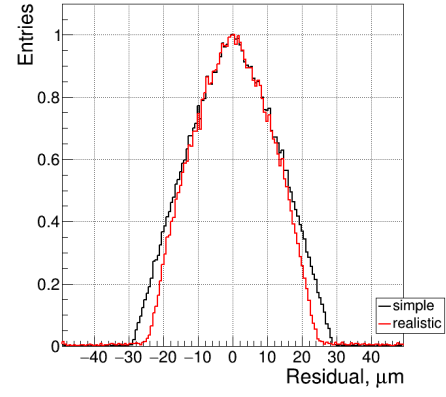


Figure A.2: Occupancy per readout channel. Different panels present stations, each module within a station corresponds to one x-bin. The realistic detector response model.

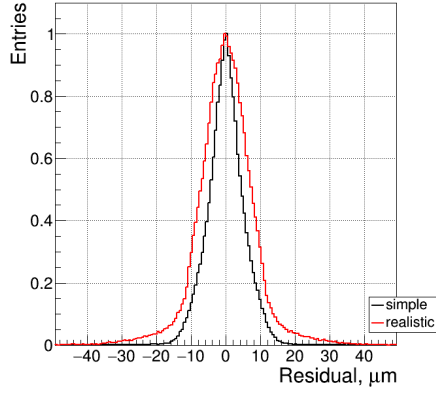
Residuals



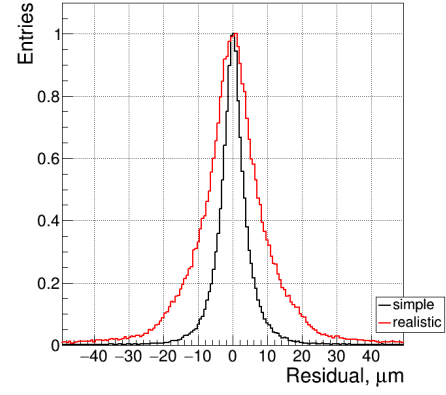
(a) All clusters.



(b) 1-strip clusters.



(c) 2-strip clusters.



(d) 3-strip clusters.

Figure A.3: Residuals distribution obtained using the simple (*black*) and the realistic (*red*) detector response models. The distributions are normalised to the maximum value.

B

Urban method

Urban method is a simple Monte Carlo method that computes energy losses with δ -ray production above some cut-off energy (details can be found in [67, 71]). It is a fast method and can be used for any thickness of medium. The method assumes that the atoms have only two energy levels with binding energies E_1 and E_2 . The particle-atom interaction will then be an excitation with energy loss E_1 or E_2 , or an ionisation with an energy loss distributed according to the function that depends on the particle energy E as

$$g(E) = \frac{(E_{\max} + I)I}{E_{\max}} \frac{1}{E^2},$$

where E_{\max} is the cut-off energy for δ -ray production, or the maximum energy transfer minus mean ionisation energy I , if it is smaller than the cut-off energy. The macroscopic cross-section for excitations for i -th level ($i = 1, 2$) is

$$\Sigma_i = C \frac{f_i}{E_i} \frac{\ln(2m\beta^2\gamma^2/E_i) - \beta^2}{\ln(2m\beta^2\gamma^2/I) - \beta^2},$$

and the macroscopic cross-section for ionisation is

$$\Sigma_3 = C \frac{E_{\max}}{I(E_{\max} + I) \ln((E_{\max} + I)/I)} r.$$

In the last two formulas, m is the mass of the incident particle, $\beta = v/c$ and γ for the incident particle, r and C are free parameters of the model ($0 \leq r \leq 1$), f_i is the oscillator strength. The oscillator strength together with the atomic level energies

E_i should satisfy the constraints

$$\begin{aligned} f_1 + f_2 &= 1, \\ f_1 \ln E_1 + f_2 \ln E_2 &= \ln I. \end{aligned}$$

The parameter C is the mean energy loss dE/dx in a step. The mean energy loss can be estimated as a sum of the excitation and ionisation contributions

$$\frac{dE}{dx} = \Sigma_1 E_1 + \Sigma_2 E_2 + \Sigma_3 \int_I^{E_{\max}+I} E g(E) dE.$$

The following values for the other parameters are used in the Geant framework:

$$\begin{aligned} f_2 &= \begin{cases} 0, & Z \leq 2 \\ 2/Z, & Z > 2 \end{cases} \Rightarrow f_1 = 1 - f_2, \\ E_2 = 10Z^2 \text{ eV} &\Rightarrow E_1 = \left(\frac{I}{E_2^{f_2}} \right)^{1/f_1}, \\ r &= 0.4. \end{aligned}$$

With these values, E_2 corresponds approximately to the K-shell energy of the atoms and Zf_2 to the number of K-shell electrons. Only the parameter r can be tuned freely. It determines the relative contribution of ionisation and excitation to the energy loss.

The cross-section is considered to be constant along the path length, thus the energy loss due to excitation is computed as

$$\Delta E_e = n_1 E_1 + n_2 E_2,$$

where n_1 and n_2 are numbers of collisions in a step Δx sampled from the Poissonian distribution with a mean $\langle n_i \rangle = \Sigma_i \Delta x$. The loss due to the ionisation can be generated from the distribution $g(E)$ by the inverse transformation method:

$$\begin{aligned} u &= F(E) = \int_I^E g(x) dx, \\ E &= F^{-1}(u) = \frac{I}{1 - u \frac{E_{\max}}{E_{\max}+I}}, \end{aligned}$$

where u is a uniform random number between $F(I) = 0$ and $F(E_{\max} + I) = 1$. The

contribution from the ionisations is

$$\Delta E_i = \sum_{j=1}^{n_3} \frac{I}{1 - u_j \frac{E_{\max}}{E_{\max} + I}},$$

where n_3 is the number of ionisations sampled from the Poissonian distribution. The total energy loss in a step is $\Delta E = \Delta E_e + \Delta E_i$.



2-strip clusters

Here, I consider creation of 2-strip clusters in the strip detector with ideal detector response. The detector response is a uniform charge distribution, corresponding to the projection of the particle trajectory on the readout (strip) plane. This charge distribution, which is then integrated on the readout channels, can be characterised by two independent variables: the entry and exit coordinates of the track in the sensor, x_{in} and x_{out} . Since sensor thickness is small, the trajectory within the sensor is approximated by a straight line, and the true coordinate is defined:

$$x_{\text{true}} \stackrel{\text{def}}{=} (x_{\text{in}} + x_{\text{out}})/2. \quad (\text{C.1})$$

Probability density distribution for trajectories that create a 2-strip cluster can be derived from that of x_{in} and x_{out} . I assume that x_{in} and x_{out} are independent, x_{in} is distributed uniformly in $[-p, 0]$ and x_{out} — in $[0, p]$, where p is a strip pitch (the coordinate system is defined in fig. C.1). The unnormalised probability density is $P_2(x_{\text{in}}, x_{\text{out}}) = P(x_{\text{in}}) \times P(x_{\text{out}})$. For clusters with two or more strips, the measured

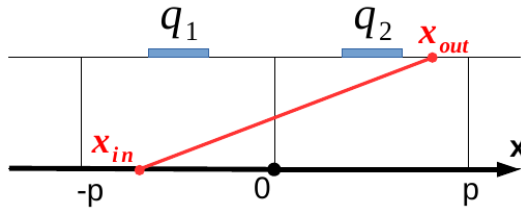


Figure C.1: Schematic draw of 2-strip clusters formation.

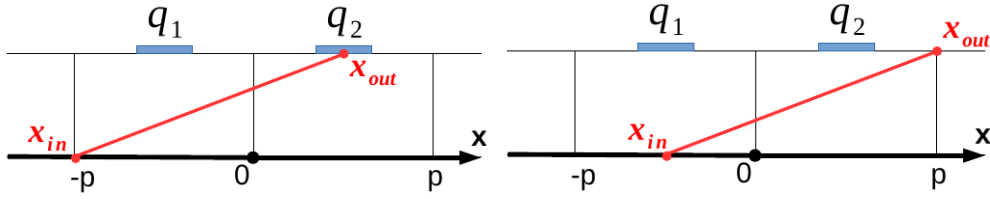


Figure C.2: Schematic draw of extreme cases of 2-strip clusters formation.

charges q_i can be used for the cluster position determination.

The measured charges $q_{1,2}$ put further constraints on possible trajectories. Each track with a given configuration $q_{1,2}$ can be described with only one variable. I choose $(x_{\text{in}} + x_{\text{out}})/2 \equiv x_{\text{true}}$ and fix value of the charge ratio $k = q_2/q_1$. Figure 3.6 shows that fixed k corresponds to some set of particle trajectories. To calculate the probability density of the trajectories, I switch from $(x_{\text{in}}, x_{\text{out}})$ to (x_{true}, k) using the Jacobian:

$$J = \left\| \begin{array}{cc} \frac{\partial x_{\text{in}}}{\partial x_{\text{true}}} & \frac{\partial x_{\text{out}}}{\partial x_{\text{true}}} \\ \frac{\partial x_{\text{in}}}{\partial k} & \frac{\partial x_{\text{out}}}{\partial k} \end{array} \right\|.$$

From the definition of x_{true} (eq. C.1): $x_{\text{out}} = 2x_{\text{true}} - x_{\text{in}}$. If $x_{\text{in}} < 0$, then $x_{\text{in}} = \frac{2x_{\text{true}}}{1-k}$ and $x_{\text{out}} = \frac{-2x_{\text{true}}k}{1-k}$. The case $x_{\text{in}} > 0$ is derived with exchange $x_{\text{in}} \leftrightarrow x_{\text{out}}$. Thus, I describe here only the case $x_{\text{in}} < 0$.

$$J = \left\| \begin{array}{cc} \frac{2}{1-k} & \frac{-2k}{1-k} \\ \frac{2x_{\text{true}}}{(1-k)^2} & \frac{-2x_{\text{true}}}{(1-k)^2} \end{array} \right\| = \frac{1}{(1-k)^3} (-4x_{\text{true}} + 4x_{\text{true}}k) = \frac{-4x_{\text{true}}}{(1-k)^2}.$$

Thus, the probability density of the trajectories is

$$P_2(x_{\text{true}}, k) = P(x_{\text{in}}) \cdot P(x_{\text{out}}) \cdot \left| \frac{-4x_{\text{true}}}{(1-k)^2} \right|. \quad (\text{C.2})$$

NORMALISATION. If $q_1 > q_2$ (critical case is shown on the left panel of fig. C.2), then $x_{\text{true}} \in (x_{\min}, 0)$, where $x_{\min} = \frac{p}{2} \frac{q_2 - q_1}{q_1}$. Then the normalization factor is

$$N = \int_{x_{\min}}^0 P_2(x_{\text{true}}, k) dx_{\text{true}} = \int_{x_{\min}}^0 dx_{\text{true}} \frac{-4x_{\text{true}}}{(1-k)^2} = \frac{4x_{\min}^2}{2(1-k)^2} = \frac{2}{(1-k)^2} \frac{p^2}{4} (k-1)^2 = \frac{p^2}{2}. \quad (\text{C.3})$$

C.1 THE UNBIASED CPFA

MEAN x_{true} . The idea of the unbiased CPFA is to define the x_{rec} in such a way that it reproduces x_{true} with a minimal residual for each fixed $k = q_2/q_1$. Thus, $x_{\text{rec}} \stackrel{\text{def}}{=} \langle x_{\text{true}} \rangle$.

$$\begin{aligned} \langle x_{\text{true}} \rangle &= \frac{1}{N} \int_{x_{\min}}^0 x_{\text{true}} P_2(x_{\text{true}}, k) dx_{\text{true}} = \frac{1}{N} \int_{x_{\min}}^0 x_{\text{true}} dx_{\text{true}} \frac{-4x_{\text{true}}}{(1-k)^2} = \\ &= \frac{1}{N} \frac{4}{(1-k)^2} \frac{x_{\min}^3}{3} = \frac{1}{N} \frac{p^3(k-1)}{6} = \frac{p^3(k-1)}{6} \frac{2}{p^2} = \frac{q_2 - q_1}{q_1} \frac{p}{3} = \frac{p}{3} (k-1). \end{aligned} \quad (\text{C.4})$$

If $q_1 < q_2$ (critical case is shown on the right panel of fig. C.2):

$$\langle x_{\text{true}} \rangle = \frac{q_2 - q_1}{q_2} \frac{p}{3} = \frac{p}{3} (1 - 1/k). \quad (\text{C.5})$$

To generalise:

$$x_{\text{rec}} \stackrel{\text{def}}{=} \langle x_{\text{true}} \rangle = \frac{p}{3} \frac{q_2 - q_1}{\max(q_1, q_2)}. \quad (\text{C.6})$$

DISPERSION. To estimate the position error that is introduced by CPFA itself, I calculate the dispersion

$$\sigma_{\text{CPFA}}^2 = \langle \Delta x^2 \rangle - \langle \Delta x \rangle^2 = \langle \Delta x^2 \rangle = \langle (x_{\text{true}} - x_{\text{rec}})^2 \rangle = \frac{1}{N} \int (x_{\text{true}} - x_{\text{rec}})^2 P_2(x_{\text{true}}, k) dx_{\text{true}}. \quad (\text{C.7})$$

If $q_1 > q_2$:

$$\langle \Delta x^2 \rangle = \frac{1}{N} \int_{x_{\min}}^0 (x_{\text{true}} - x_{\text{rec}})^2 dx_{\text{true}} \frac{-4x_{\text{true}}}{(1-k)^2} = \frac{1}{N} \frac{4x_{\min}^2}{(1-k)^2} \left(\frac{x_{\min}^2}{4} - \frac{2x_{\text{rec}}x_{\min}}{3} + \frac{x_{\text{rec}}^2}{2} \right). \quad (\text{C.8})$$

After taking into account that for $q_1 > q_2$ $x_{\min} = \frac{p}{2}(k-1)$ and $x_{\text{rec}} = \frac{p}{3}(k-1)$:

$$\begin{aligned} \langle \Delta x^2 \rangle &= \frac{(1-k)^2}{4x_{\min}^2} \frac{4x_{\min}^2}{(1-k)^2} \left(\frac{x_{\min}^2}{4} - \frac{2x_{\text{rec}}x_{\min}}{3} + \frac{x_{\text{rec}}^2}{2} \right) = \\ &= 2 \left(\frac{x_{\min}^2}{4} - \frac{2x_{\text{rec}}x_{\min}}{3} + \frac{x_{\text{rec}}^2}{2} \right) = \\ &= \frac{1}{2} \frac{p^2}{4} (k-1)^2 - \frac{4}{3} \frac{p^2}{6} (k-1)^2 + \frac{p^2}{9} (k-1)^2 = \frac{p^2(k-1)^2}{72} = \\ &= \frac{p^2}{72} \left(\frac{q_2 - q_1}{q_1} \right)^2. \end{aligned} \quad (\text{C.9})$$

If $q_1 < q_2$

$$\langle \Delta x^2 \rangle = \frac{p^2(1/k - 1)^2}{72} = \frac{p^2}{72} \left(\frac{q_2 - q_1}{q_2} \right)^2. \quad (\text{C.10})$$

To generalise:

$$\langle \Delta x^2 \rangle = \frac{p^2}{72} \left(\frac{q_2 - q_1}{\max(q_1, q_2)} \right)^2. \quad (\text{C.11})$$

C.2 THE CENTRE-OF-GRAVITY CPFA

MEAN RESIDUAL $\langle x_{\text{true}} - x_{\text{rec}} \rangle$. The COG defines the reconstructed cluster position (the coordinate system is in fig. C.1) for 2-strip clusters as (general formula is eq. 3.4)

$$x_{\text{rec}} \stackrel{\text{def}}{=} \frac{p}{2} \frac{q_2 - q_1}{q_1 + q_2}. \quad (\text{C.12})$$

The mean residual for the case $q_1 > q_2$ is

$$\begin{aligned}
\langle x \rangle &= \langle x_{\text{true}} - x_{\text{rec}} \rangle = \frac{1}{N} \int_{x_{\min}}^0 (x_{\text{true}} - x_{\text{rec}}) P_2(x_{\text{true}}, k) dx_{\text{true}} = \\
&= \frac{1}{N} \int_{x_{\min}}^0 (x_{\text{true}} - x_{\text{rec}}) dx_{\text{true}} \frac{-4x_{\text{true}}}{(1-k)^2} = \\
&= \frac{1}{N} \frac{4x_{\min}^2}{(1-k)^2} \left(\frac{x_{\min}}{3} - \frac{x_{\text{rec}}}{2} \right) = \frac{(1-k)^2}{4x_{\min}^2} \frac{4x_{\min}^2}{(1-k)^2} \left(\frac{x_{\min}}{3} - \frac{x_{\text{rec}}}{2} \right) = \\
&= \frac{2}{3} x_{\min} - x_{\text{rec}} = \frac{2}{3} \frac{p}{2} \frac{q_2 - q_1}{q_1} - \frac{p}{2} \frac{q_2 - q_1}{q_2 + q_1} = \frac{p}{2} \frac{(q_2 - q_1)(2q_2 - q_1)}{3q_1(q_1 + q_2)} \neq 0.
\end{aligned}
\tag{C.13}$$



N-strip clusters in the unbiased algorithm

Here, I consider creation of n-strip clusters in the strip detector with ideal detector response. The detector response is a uniform charge distribution, corresponding to the projection of the particle trajectory on the readout (strip) plane. This charge distribution, which is then integrated on the readout channels, can be characterised by two independent variables: the entry and exit coordinates of the track in the sensor, x_{in} and x_{out} . Since the thickness of the sensors is small, the trajectory within the sensor is approximated by a straight line, and the true coordinate is defined:

$$x_{\text{true}} \stackrel{\text{def}}{=} (x_{\text{in}} + x_{\text{out}})/2. \quad (\text{D.1})$$

Since the energy loss is uniform, the trajectory length within one strip is proportional to the registered charge (see fig. D.1 for the c.s. definition):

$$\frac{p - x_{\text{in}}}{q_i} = \frac{p}{q} = \frac{x_{\text{out}} - p}{q_j}, \quad (\text{D.2})$$

where p is a strip pitch, q_i and q_j are the registered charge in the first and the last strip of the cluster, q is the registered charge in each of the middle strips of the cluster. From eq. (D.2) the entry and exit coordinate are derived as

$$x_{\text{in}} = p - \frac{q_i p}{q}, \quad x_{\text{out}} = \frac{q_j p}{q} - (n - 1)p. \quad (\text{D.3})$$

Then x_{true} can be rewritten as

$$x_{\text{true}} = \frac{1}{2} \left[p - \frac{q_i p}{q} + \frac{q_j p}{q} - (n-1)p \right] = \frac{1}{2} \left[p \frac{q_j - q_i}{q} + np \right]. \quad (\text{D.4})$$

The centres of the first and the last strip of the cluster have coordinates: $x_i = p/2$

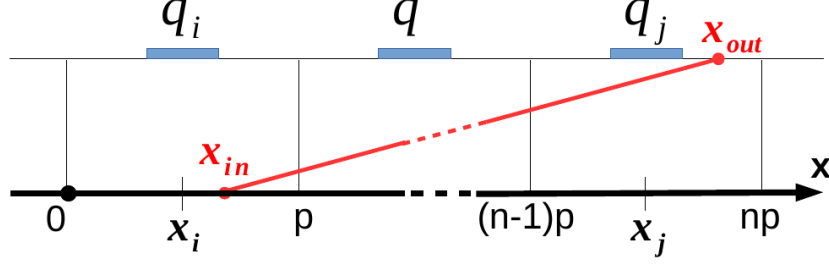


Figure D.1: Schematic draw of n-strip clusters formation.

and $x_j = np - p/2$. They can be used in eq. (D.4)

$$x_{\text{true}} = \frac{1}{2} \left[p \frac{q_j - q_i}{q} + x_i + x_j \right] = \frac{1}{2} (x_i + x_j) + \frac{p}{2} \frac{q_j - q_i}{q}. \quad (\text{D.5})$$

Thus, the reconstructed position for n-strip clusters can be defined as

$$x_{\text{rec, Ns}} \stackrel{\text{def}}{=} \frac{1}{2} (x_i + x_j) + \frac{p}{2} \frac{q_j - q_i}{q}. \quad (\text{D.6})$$

E

Data from the in-beam tests

E.1 TEST OF IRRADIATED SENSORS

In December 2014, four different sensors produced by Hamamatsu were measured in a beam test (see section 4.1 and 4.2.1). One sensor of each type, single-metal (SM, without second metal layer) and double-metal (DM, with second-metal layer), had been irradiated prior to the test (“irr” on the plots) to 2×10^{14} 1 MeV n_{eq}/cm^2 . As a reference, one sensor of each type (SM and DM) was not irradiated (“non-irr”). Some data are presented in this section.

The maps of connected and not masked channels for sensors under the test are shown in fig. E.1. Only 40 strips per side for each sensors were bonded to the PCB. Some of the bonds were broken during transportation, because size of sensors did not fit perfectly to the size of opening in PCB and sensors were not glued into the PCB. Some channels were masked at the software level due to very high noise.

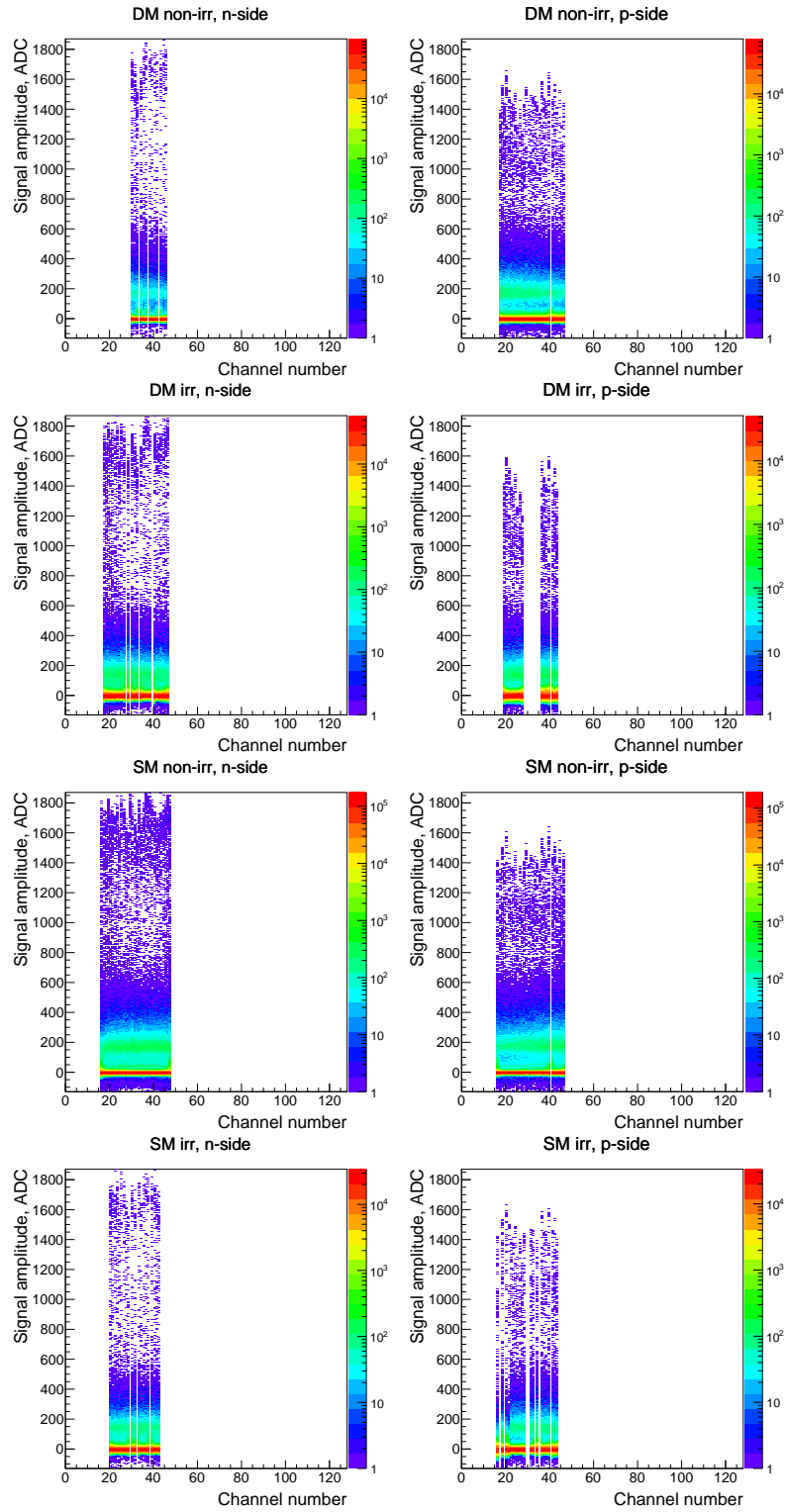


Figure E.1: Maps of channels which were taken into the analysis. Types of sensor and sensor sides are mentioned on top of each histogram.

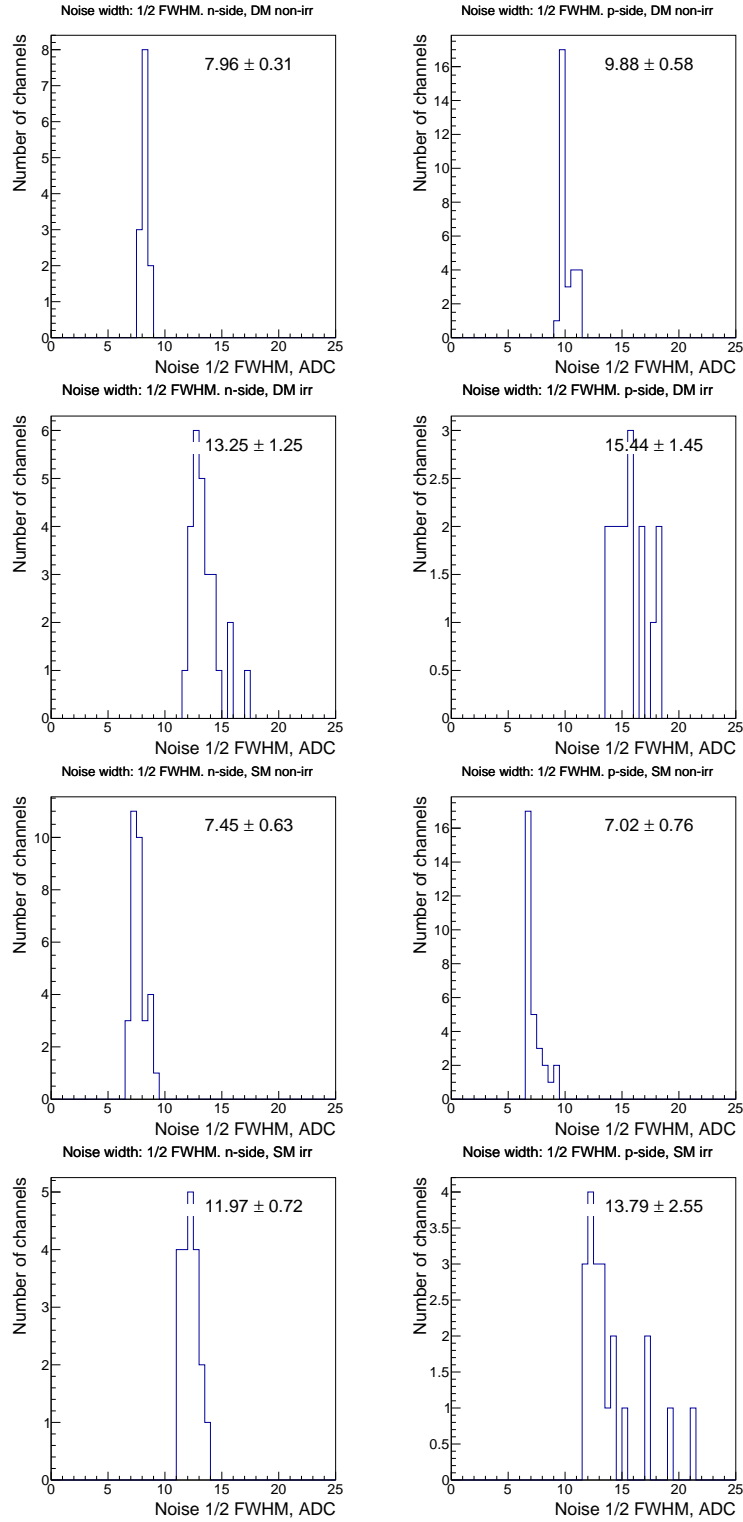


Figure E.2: Distribution of 1/2 FWHM of noise. Types of sensor and sensor sides are mentioned on top of each histogram.

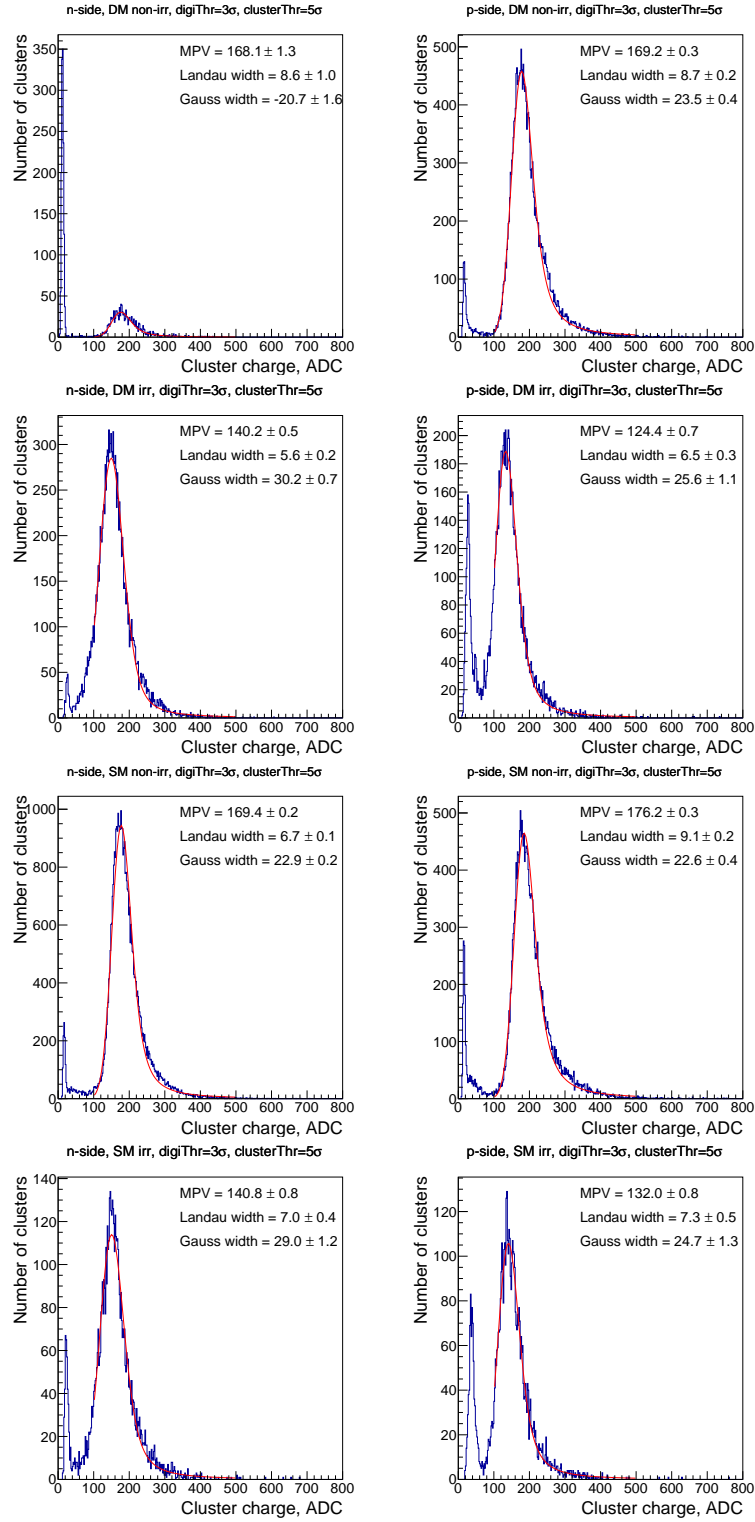


Figure E.3: Distribution of 1-strip cluster charge, $Q_{\text{digi}}^{\min} = 3\sigma$ and $Q_{\text{cl}}^{\min} = 5\sigma$, where σ is the width of noise distribution in the current event. Types of sensor and sensor sides are mentioned on top of each histogram.

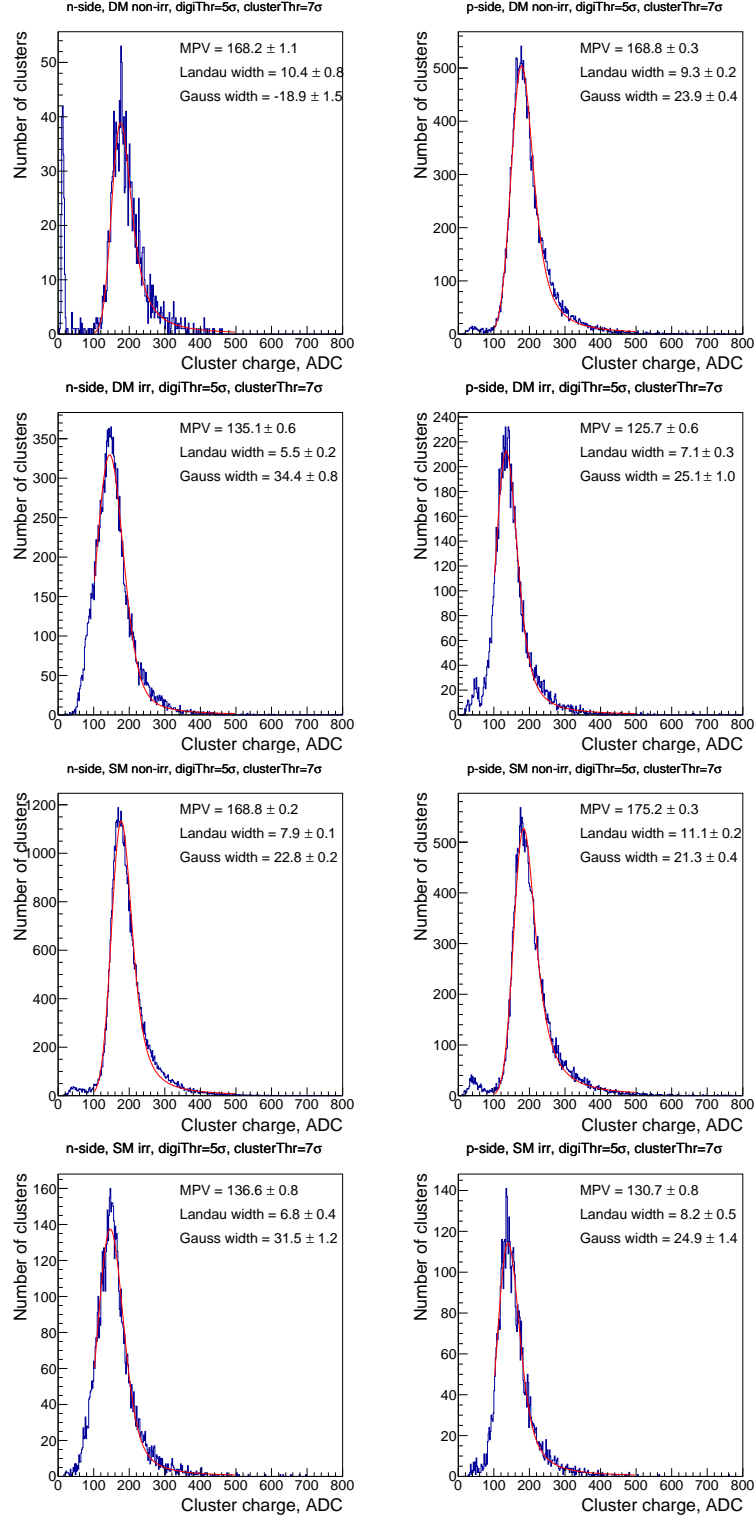


Figure E.4: Distribution of 1-strip cluster charge, $Q_{\text{digi}}^{\min} = 5\sigma$ and $Q_{\text{cl}}^{\min} = 7\sigma$, where σ is the width of noise distribution in the current event. Types of sensor and sensor sides are mentioned on top of each histogram.

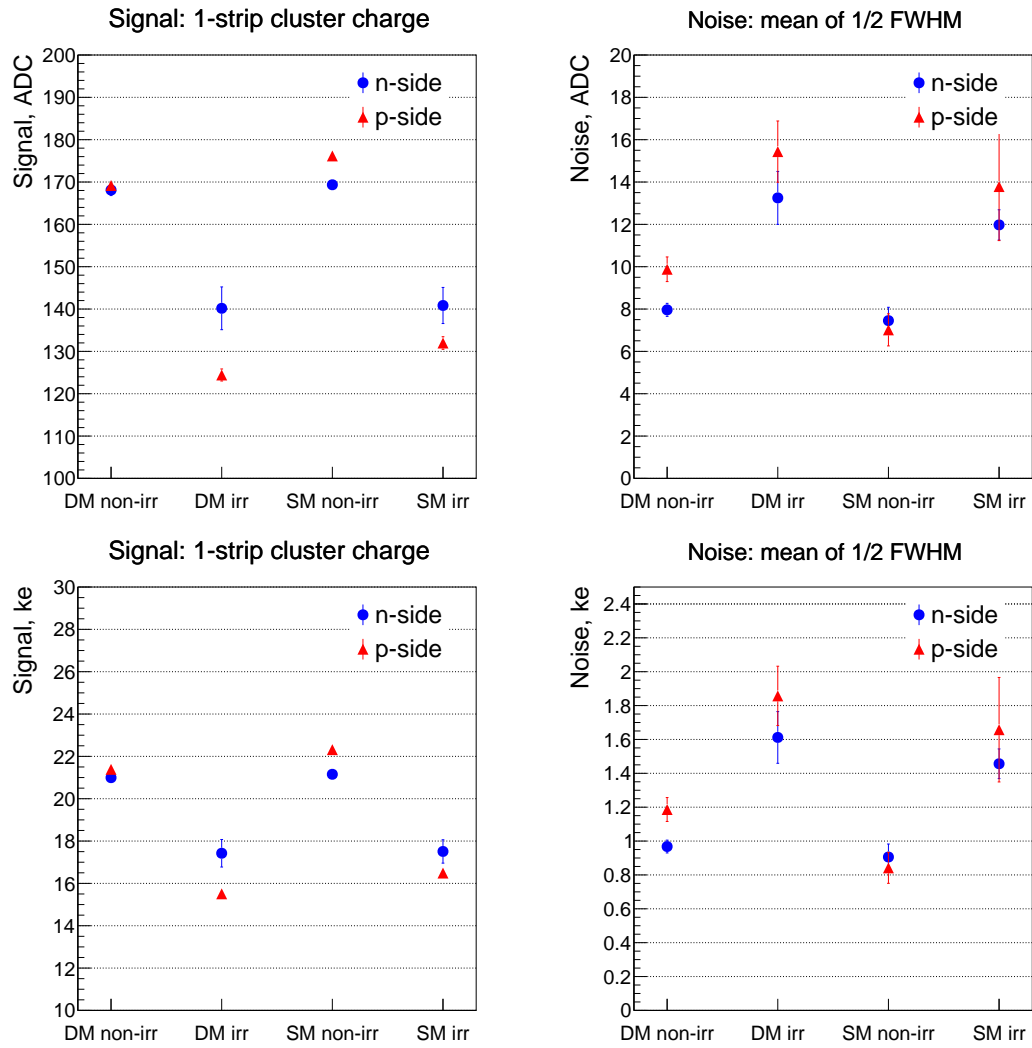


Figure E.5: Signal (*left* panels) and noise (*right* panels) for all sensors in ADC units (*top* panels) and ke (*bottom* panels). Labels on the abscissas present the type of the sensor.

E.2 TEST OF MODULES

Four different module prototypes were measured during the in-beam tests. Each comprises of 1 or 2 daisy-chained sensors produced by CiS and a 30 cm long micro-cable that connects 128 channels (see section 4.1 and 4.2.1):

- M1: single sensor with central part connected (tested in 2013);
- M2: single sensor with edge strips connected (tested in 2014);
- M3: two daisy-chained sensors with central part connected (2013);
- M4: two daisy-chained sensors with edge strips connected (2013).

Some data are presented in this section.

The maps of connected and not masked channels for sensors under the test are shown in fig. E.6. 128 strips per side for each sensor were bonded to the PCB. Some of the bonds were broken and some channels were masked at the hardware or software level due to very high noise.

The *top-left* panel of fig. E.6 is a clear presentation of the signal. It shows the signal amplitude for each channel of the n-side of module M1. The light blue band between 100 and 150 ADC corresponds to 1-strip clusters. The orange band at about 50 ADC corresponds to fired strips of 2-strip clusters: each strip gets only a fraction of the total cluster charge. Position of this band varies for each channel because the signal distribution “sits” on the noise distribution of different width for each channel. For other modules, the regions of 2-strip clusters are completely hidden by the baseline (the red regions at 0 ADC) because other modules have higher noise: ≥ 9 ADC for all modules, except n-side of module M1, which has the baseline width of 8 ADC (see fig. E.7).

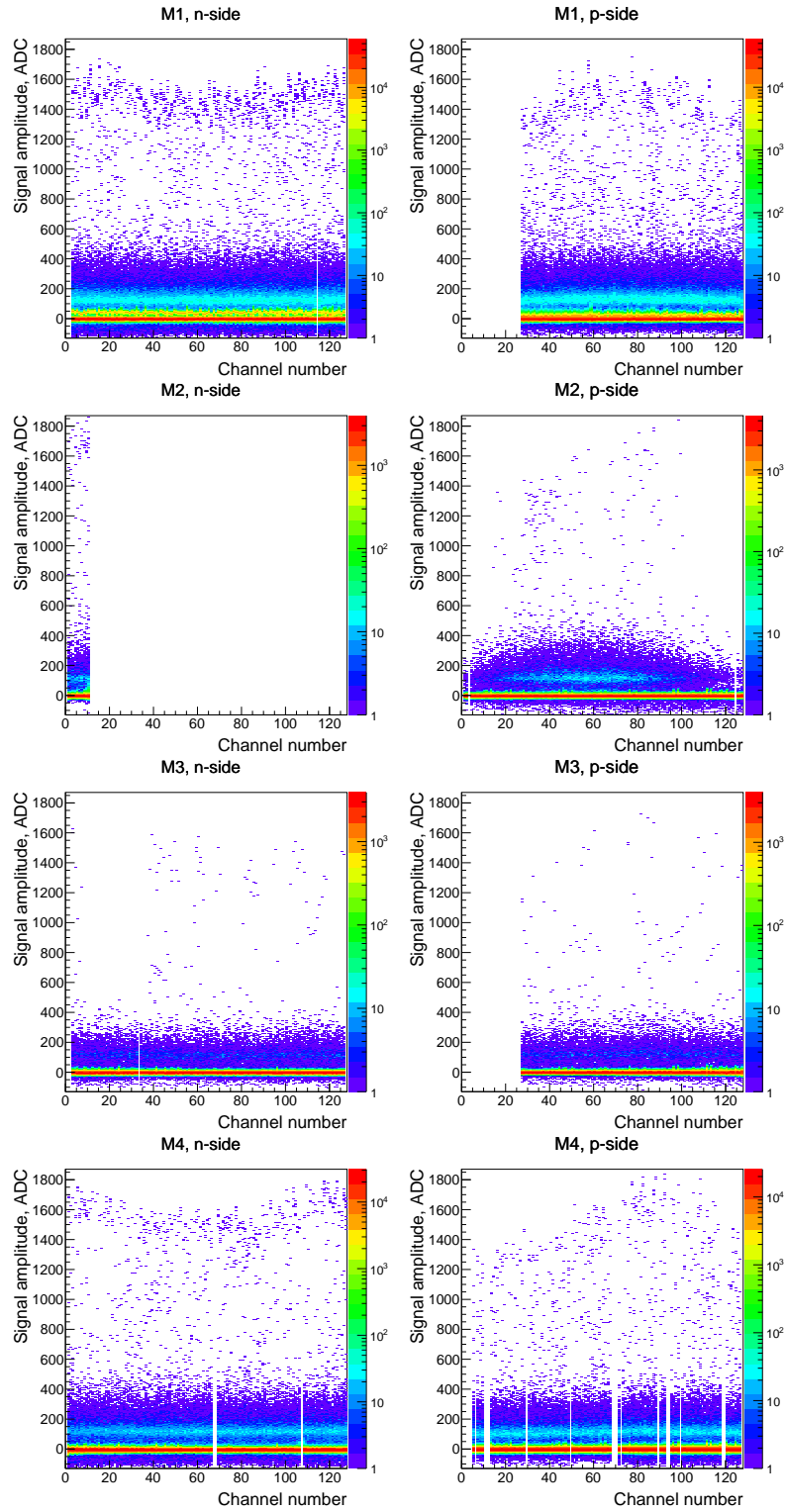


Figure E.6: Maps of channels which were taken into the analysis. Types of module and sensor sides are mentioned on top of each histogram.

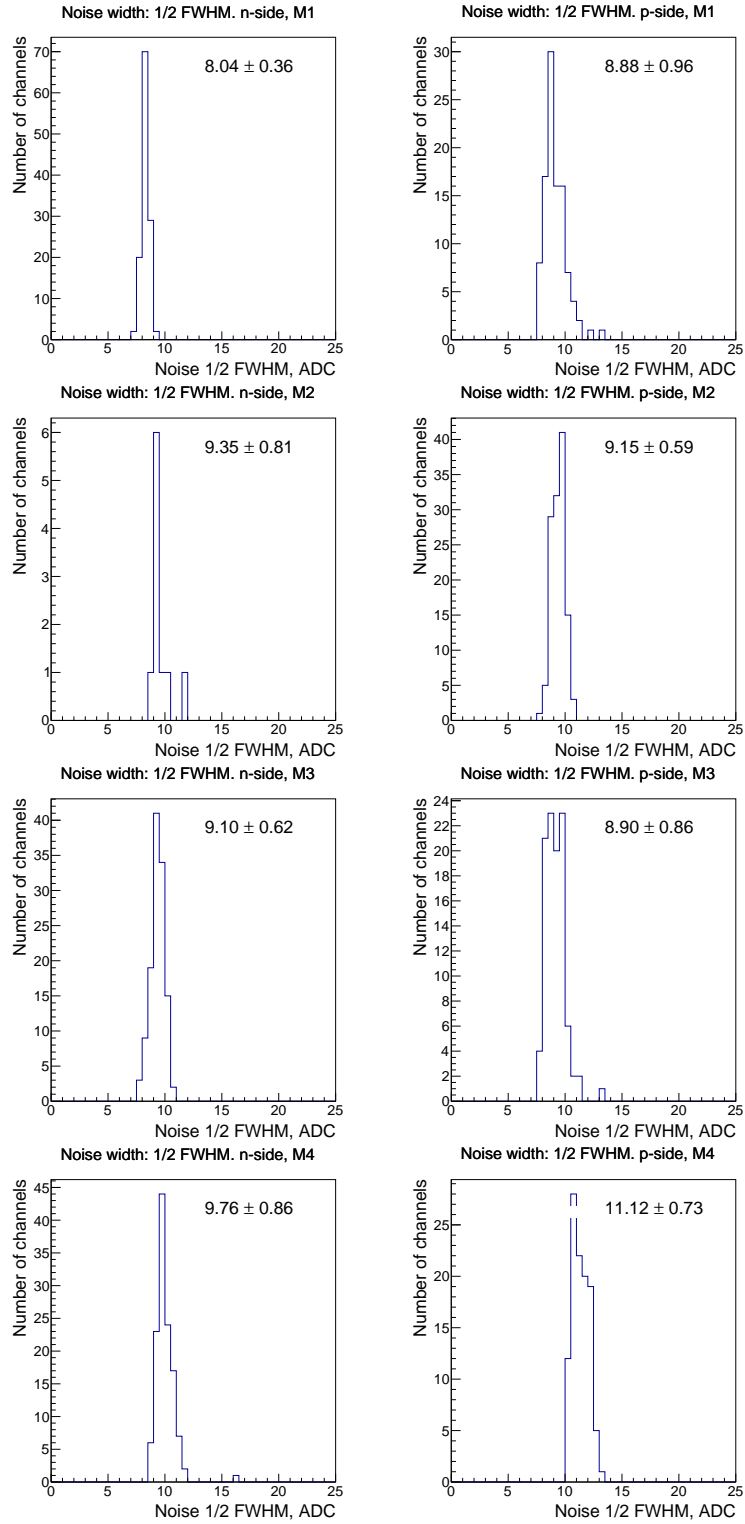


Figure E.7: Distribution of 1/2 FWHM of noise. Types of module and sensor sides are mentioned on top of each histogram.

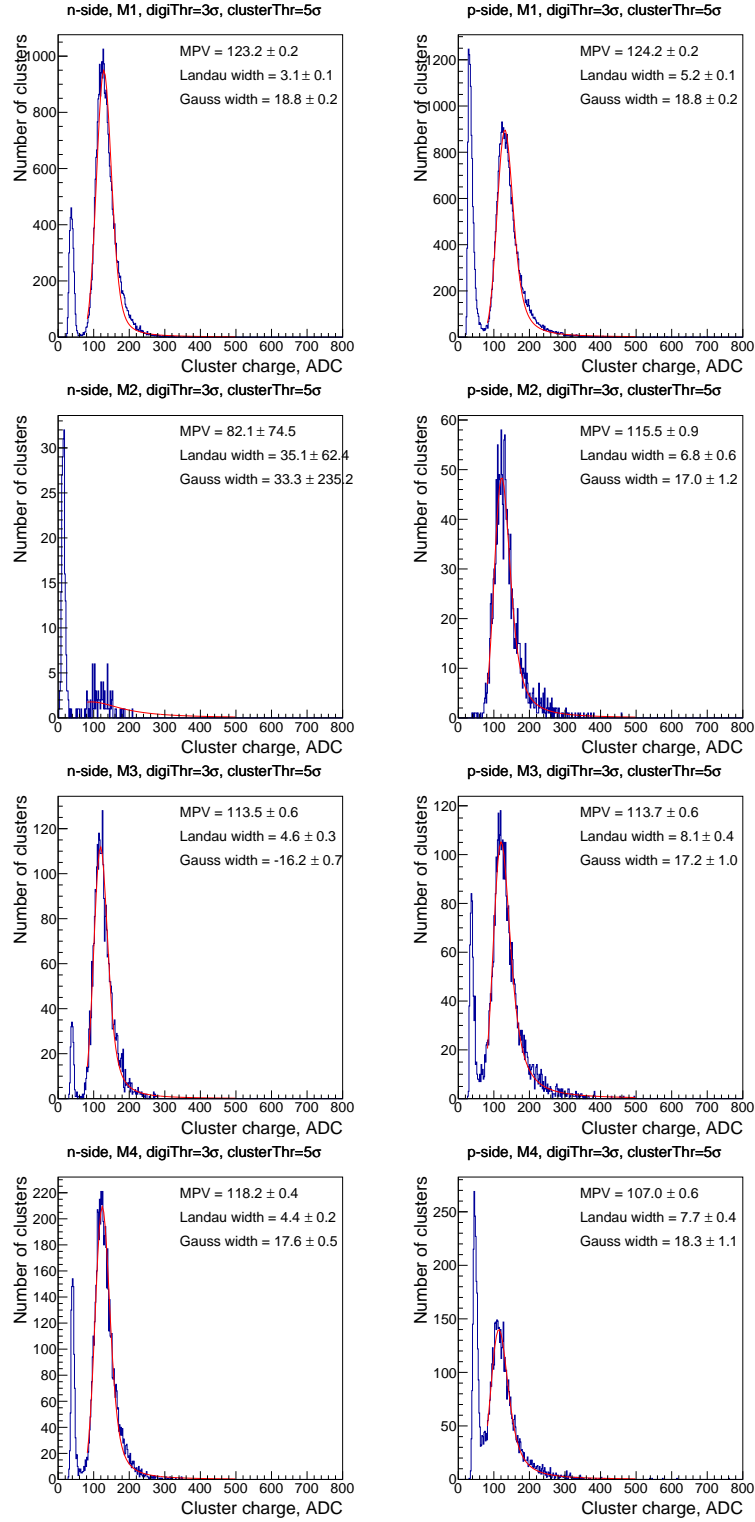


Figure E.8: Distribution of 1-strip cluster charge, $Q_{\text{digi}}^{\min} = 3\sigma$ and $Q_{\text{cl}}^{\min} = 5\sigma$, where σ is the width of noise distribution in the current event. Types of module and sensor sides are mentioned on top of each histogram.

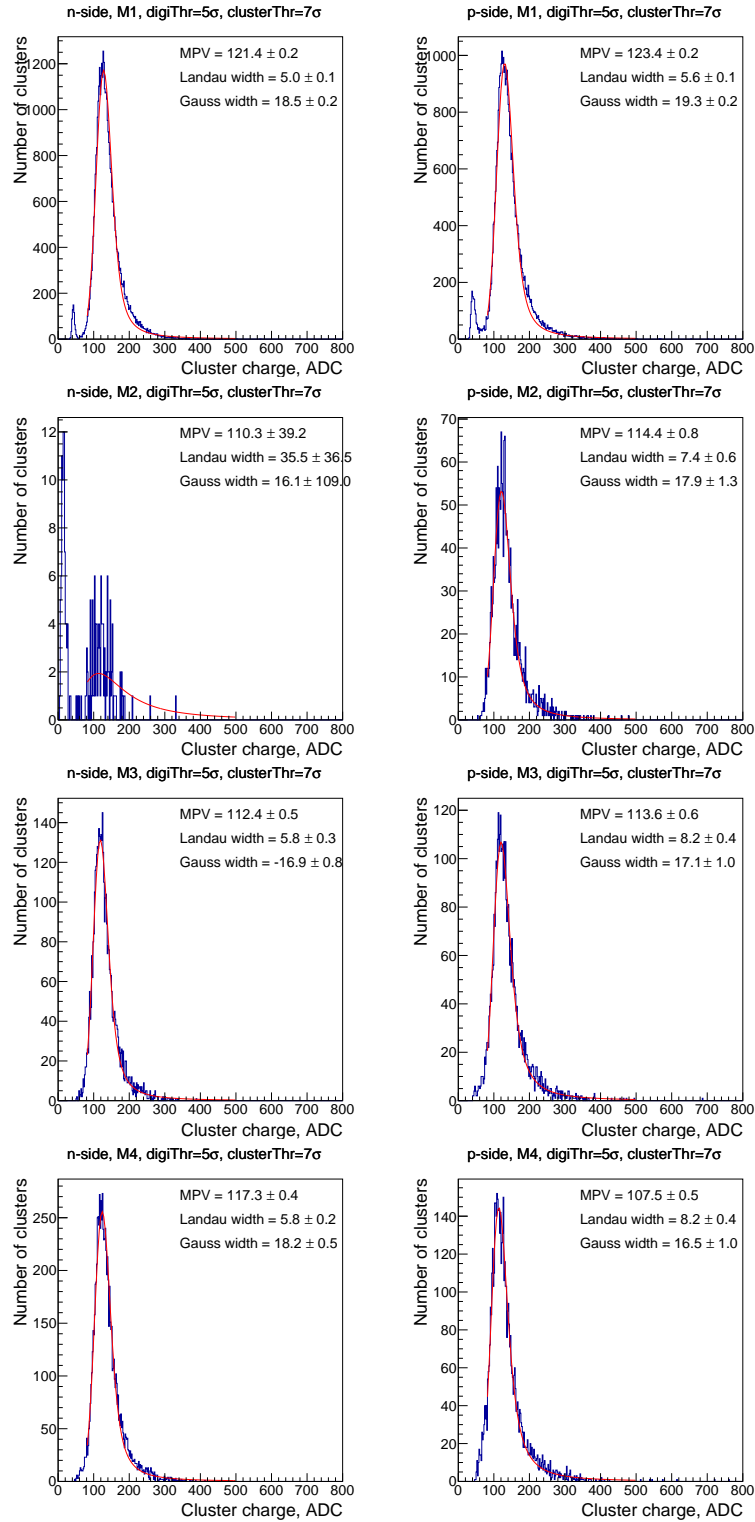


Figure E.9: Distribution of 1-strip cluster charge, $Q_{\text{digi}}^{\min} = 5\sigma$ and $Q_{\text{cl}}^{\min} = 7\sigma$, where σ is the width of noise distribution in the current event. Types of module and sensor sides are mentioned on top of each histogram.

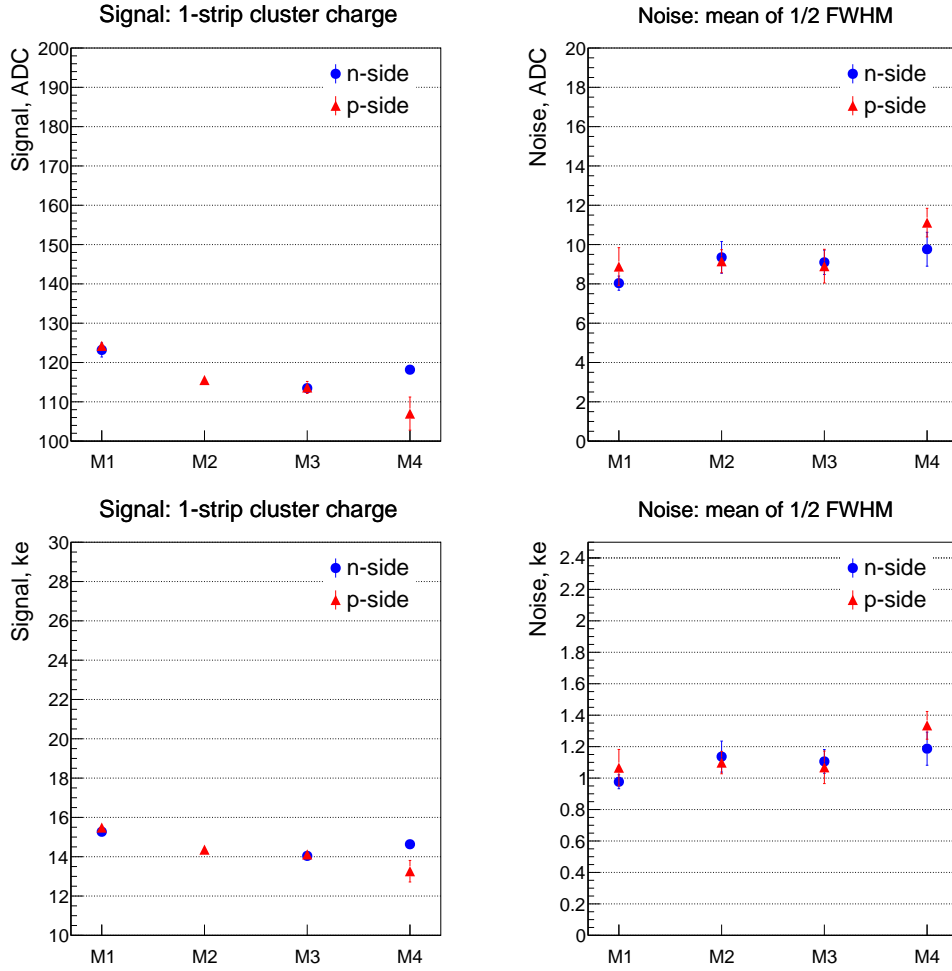


Figure E.10: Signal (*left panels*) and noise (*right panels*) for all modules in ADC units (*top panels*) and ke (*bottom panels*). Labels on the abscissas present the type of the module.

E.3 CLUSTER SIZE DISTRIBUTION

Figure 4.17 presents some of the cluster size distributions for the n-side obtained with module 1 during the beam test in 2013 in comparison with two detector response models: the simple one and the realistic one (see section 4.3 for details).

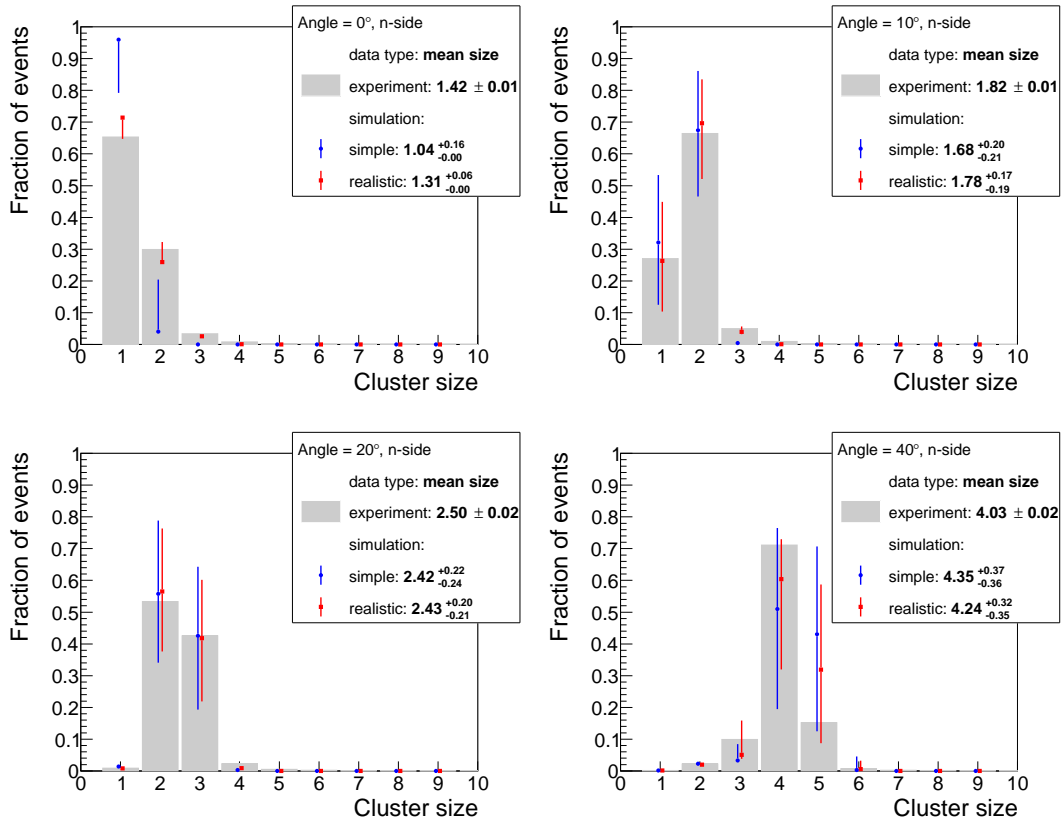


Figure E.11: Cluster size distributions for different incidence angles on the n-side of the sensors (module 1). Experimental (grey filled histograms) and simulated data with two models: simple (blue points) and realistic (red). The average cluster sizes are mentioned in the legends. Error bars include statistical errors, uncertainty of the incidence angle measurement, capacitance variation and capacitance measurement error. Statistical errors for the experimental data are not shown because they are very small and would be not visible on the plots

F

Influence of the micro-cables on the charge collection

The total charge integrated in the readout electronics is not equal to the charge collected on the implant due to parasitic capacitances. The sophisticated analysis to estimate the ratio of the charges is described in section 2.2.2.3. Formula (2.14) estimates the integrated charge in the CSA. Using the values of all the capacitances (C_{iAC} , C_{iDC} , C_{iACDC} , C_c , C_{bulk} , C_{CSA} , C_{cable}) given in section 2.2.2.3, the obtained ratios are presented in table F.1. The presense of the micro-cable (version of year 2016) effectively decreases the CCE by 2 – 11 % depending on the length. As an average estimate for the whole STS, I will assume that the presense of the micro-cable (version of year 2016) effectively worsen the CCE at most by 11 %.

Table F.1: Ratios of the integrated charge in the CSA to the charge collected on the respective implant $Q_{\text{CSA}}^{\text{centr}}/Q_{\text{implant}}$ and with the ratios of the integrated charge in one of the neighbouring CSA to the charge collected on the implant $Q_{\text{CSA}}^{\text{neib}}/Q_{\text{implant}}$ micro-cable of different length or without micro-cable for both sides of the sensor. Results for the micro-cable version used during in-beam tests 2013 and 2014: $C_{\text{cable}} = 1.06 \pm 0.2 \text{ pF/cm}$; and for the micro-cable version of year 2016: $C_{\text{cable}} = 0.38 \pm 0.02 \text{ pF/cm}$.

	p-side		n-side	
	$Q_{\text{CSA}}^{\text{centr}}/Q_{\text{implant}}$	$Q_{\text{CSA}}^{\text{neib}}/Q_{\text{implant}}$	$Q_{\text{CSA}}^{\text{centr}}/Q_{\text{implant}}$	$Q_{\text{CSA}}^{\text{neib}}/Q_{\text{implant}}$
w/o micro-cable	0.927 ± 0.008	0.028 ± 0.003	0.901 ± 0.013	0.038 ± 0.006
Micro-cable version of the year 2013				
11 cm micro-cable	0.893 ± 0.010	0.026 ± 0.003	0.868 ± 0.014	0.037 ± 0.005
30 cm micro-cable	0.840 ± 0.017	0.024 ± 0.003	0.816 ± 0.019	0.034 ± 0.005
52 cm micro-cable	0.786 ± 0.024	0.022 ± 0.003	0.764 ± 0.025	0.031 ± 0.005
Micro-cable version of the year 2016				
11 cm micro-cable	0.914 ± 0.007	0.027 ± 0.003	0.889 ± 0.013	0.038 ± 0.006
30 cm micro-cable	0.894 ± 0.008	0.026 ± 0.003	0.869 ± 0.013	0.037 ± 0.005
52 cm micro-cable	0.817 ± 0.008	0.026 ± 0.003	0.846 ± 0.013	0.035 ± 0.005

List of acronyms

ADC	Analogue-to-Digital Convertor
ASIC	Application-Specific Integrated Circuit
c.s.	coordinate system
CA	Cellular Automaton
CBM	Compressed Baryonic Matter
CCE	charge collection efficiency
CDF	Cumulative Distribution Function
CiS	Forschungsinstitut für Mikrosensorik GmbH
COG	Centre-Of-Gravity
COSY	COoling SYnchrotron
CPFA	Cluster Position Finding Algorithm
CSA	Charge Sensitive Amplifier
DABC	Data Acquisition Backbone Core
DAQ	Data Acquisition
DM	Double Metallisation
ECAL	Electromagnetic Calorimeter
ENC	Equivalent Noise Charge
FAIR	Facility for Antiproton and Ion Research
FEB	Front-End-Board
FLES	First-Level-Event-Selection
FWHM	Full Width at Half Maximum
GSI	GSI Helmholtzzentrum für SchwerIonenforschung
KF	Kalman Filter
LBS	Least Significant Bit
LHC	Large Hadron Collider
MAPMT	Multianode Photomultiplier Tube
MC	Monte-Carlo

MIP	Minimum Ionizing Particle
MPV	Most Probable Value
MUCH	Muon CHamber
MVD	Micro Vertex Detector
n-XYTER	Neutron-X-Y-Time-Energy Read-out
PCB	Printed Circuit Board
PMT	Photomultiplier Tube
PSD	Projectile Spectator Detector
QCD	Quantum Chromodynamics
QGP	Quark-Gluon Plasma
RHIC	Relativistic Heavy Ion Collider
RICH	Ring Imaging CHerenkov detector
ROC	Read-Out Controller
SIS100/300	Heavy ion synchrotron, SchwerIonenSynchrotron
SM	Single Metallisation
STS	Silicon Tracking System
STS-XYTER	STS-X-Y-Time-Energy Read-out
TOF	Time-Of-Flight wall
TRD	Transition Radiation Detector

Zusammenfassung

Das Phasendiagramm stark wechselwirkender Materie ist Gegenstand von erheblichem wissenschaftlichem Interesse [1]. Untersuchungen bei hohen baryonischen chemischen Potentials erlauben insbesondere, den in diesem Bereich erwarteten Phasenübergang erster Ordnung zwischen freien und in Nukleonen gebundenen Quarks zu entdecken. Dieser endet in einem Phasenübergangspunkt zweiter Ordnung, dem Kritischen Endpunkt [11]. Dichte Kernmaterie bei niedrigen Temperaturen wird für die Kernregionen von kompakten Sternen, wie Neutronensternen, vorausgesagt [11, 13]. Modellrechnungen zeigen, dass hohe baryonische Dichten auch in Schwerionenkollisionen bei moderaten Strahlenergien erreicht werden. In den letzten drei Jahrzehnten wurden verschiedene Experimente in diesem Energiebereich an Beschleunigeranlagen weltweit durchgeführt. Bisher jedoch begrenzten Beschleuniger- und Detektortechnologien insbesondere den Zugang zu Observablen, die mit sehr geringen Raten produziert werden [12]. Weitere neue Experimente sind derzeit geplant oder im Aufbau begriffen, welche die Grenzen zu signifikant höheren Wechselwirkungsraten ausweiten.

DAS COMPRESSED BARYONIC MATTER EXPERIMENT. Das Compressed Baryonic Matter (CBM) Experiment ist eine der wissenschaftlichen Säulen am zukünftigen Beschleunigerzentrum Facility for Antiproton and Ion Research (FAIR) in Darmstadt. Das CBM-Forschungsprogramm beschäftigt sich mit der Untersuchung des QCD Phasendiagramms im Bereich hoher netto-baryonischer Dichten und moderaten Temperaturen. Im Labor wird der Materiezustand durch Kollisionen von beschleunigten hochenergetischen Atomkernen erzeugt. Die Projektilenergien werden bis zu 11, in einer möglichen Ausbauphase bis zu 45 GeV/Nukleon betragen. Die aus den Kernwechselwirkungen des Schwerionenstrahls mit einem Target stammenden neuen Teilchen werden mit dem CBM-Experiment, einem Detektorsystem aus mehreren spezialisierten Nachweisgeräten in Vorwärts-Geometrie (Fixed-Target) registriert und können auf die Bedingungen bei den Kernkollisionen selbst hin analysiert werden. Das CBM-Projekt hat ein umfangreiches Physikprogramm. Es umfasst insbesondere die Beobachtung von seltenen diagnostischen Proben, welche Informationen über die dichte Phase der Kernwechselwirkung betreffen. Um Messungen mit genügend hoher Statistik zu erreichen, sind hohe Strahl-Target Wechselwirkungsraten notwendig bis zu 10 MHz, was mit einem intensiven kontinuierlichen Strahl

aus dem SIS100, später dem SIS300 Synchrotron erzielt werden kann. Die meisten Observablen weisen eine komplexe Trigger-Signatur auf. Daher kann das CBM Experiment nicht mit einem klassischen Datentransport durchgeführt werden, sondern baut konsequent auf data streaming, bei dem die Detektorsysteme zeitmarkierte Messwerte an eine Computerfarm schicken, sobald sie aufgezeichnet wurden, um dort in Echtzeit zu kernphysikalischen Ereignissen rekonstruierten zusammengesetzt zu werden. Die hohen Wechselwirkungsraten führen zu einem hohen Datenfluss bis zu 1 TB/s. Da praktische Datenspeicherraten geringer sind, müssen die komplexen Algorithmen schnellen sein und zu einem reduzierten selektiven Datensatz führen.

DAS SILICON TRACKING SYSTEM. Das Silicon Tracking System (STS) ist der zentrale Detektor des CBM-Experiments. Es vermisst die Spuren geladener Teilchen mit hoher Effizienz und bestimmt als einziger CBM-Detektor die Teilchenimpulse; dabei ist eine Auflösung von etwa 1,5% für $p > 1 \text{ GeV}/c$ zu erzielen. Um diese Anforderungen zu erreichen, muss der Detektor mit schneller Auslese ausgestattet sein, die die hohen Detektorraten von mehreren hundert Teilchenspuren in zentralen Ereignissen bei bis zu 10^7 Strahl-Target-Wechselwirkungen pro Sekunde getrennt voneinander erfassen kann. Des weiteren muss der STS Detektor mit hoher Granularität und geringer Materialdicke realisiert sein, um die Impulsauflösung leisten zu können. Das Detektorsystem wurde so konzipiert, dass es diese Anforderungen mit doppelseitig segmentierten und strahlungstoleranten Silizium-Mikrostreifensensoren und schneller selbst-triggernder Elektronik erzielt. Der Detektor umfasst 8 Messtationen in 30 bis 100 cm Entfernung vom Target. Sie decken die Polarwinkel von 2,5 bis 25 Grad ab. Das Materialbudget pro Station beträgt zwischen 0,3 und 1 Prozent Strahlungslänge. Die Sensoren sind etwa $300 \mu\text{m}$ stark und aus hoch-resistivem n-Typ Siliziumwafern gefertigt. Die Streifen-Elektroden haben Abstände von $58 \mu\text{m}$ und sind unter einem Stereowinkel von 7,5 Grad angeordnet. Die Sensoren wurden bis zur doppelten Strahlendosis getestet, die im Betrieb erwartet wird ($2 \times 10^{14} \text{ 1 MeV } n_{\text{eq}}/\text{cm}^2$). Die Detektormodule verwenden besonders dünne Kabel, um Sensoren und Elektronik so zu verbinden, dass im Detektorvolumen selbst eine möglichst geringe Masse verbaut wird. Zur schnellen Auslese wurde ein spezifischer ASIC entwickelt, der die zu erwartenden Spurdaten von bis zu 47 Mhit/s registrieren und in einem mit Zeitmarken versehenen Datenstrom weiterleiten kann. Jeder Kanäle eines ASICs, der einen Streifen ausliest, beinhaltet Schaltkreise zur Signalauflösung mit 5 Bit und Zeitstempel alle 3,125 ns.

MOTIVATION UND UMFANG DER VORLIEGENDEN ARBEIT. Simulationsstudien und effiziente Rekonstruktionsalgorithmen sind erforderlich, um die Leistungsfähigkeit und Präzision des STS-Systems zu verstehen und voll auszunutzen. Eine detaillierte Modellierung des Detektors in Simulationen ist Schlüsselkomponente dazu. Dies ermöglicht auch, Designentscheidungen zu treffen und den Detektor bestmöglich zu realisieren, unter Berücksichtigung von verschiedenen Randbedingungen wie

späteren Strahlungsschäden, hohem Rauschen, defekten Komponenten, oder aber verschiedenen Varianten von Sensordicken im Einsatz. Ebenso kann ein realistischer Digitizer dabei helfen, das Potential des STS-Detektors zur Teilchenidentifikation aufzuzeigen, was durch die Messung des Energieverlustes der Teilchen in den Sensoren erfolgt.

Eine genauer Rekonstruktionsalgorithmus der signalführenden Detektorzellen ist erforderlich, der sowohl die Hit-Clusterformung mit Bestimmung der Zentralposition und des zugehörigen Fehlers unter Berücksichtigung der Vielfachstreuung und der intrinsischen Detektorauflösung durchführt. Die Spurrekonstruktion baut auf die Clusterinformationen auf. Deren genaue Fehlerbestimmung ist wichtig, um die Spurparameter korrekt zu berechnen und falsche Spurkandidaten zu verwerfen.

REALISTISCHES DETEKTORMODELL. Die bisherige Detektorsimulation des STS [62, p.7] berücksichtigte die folgenden physikalischen Effekte: Uniformen Energieverlust der Teilchen in den Siliziumsensoren, Rauschen durch Kapazitäten und Ströme, die Signalschwelle der Ausleseelektronik, und die Lorentzverschiebung der deponierten Ladung im magnetischen Feld. Der Vergleich mit experimentell gewonnenen Daten (siehe Kapitel 4.3) zeigte jedoch Abweichungen zum Modell. Um diese zu verringern, wurde ein verbessertes Detektormodell implementiert. Es verwendet einen nicht-uniformen Energieverlust nach dem Urban-Modell, Diffusion der Ladungen im Silizium, Signalübersprechen aufgrund von Zwischenstreifenkapazitäten und eine verbesserte Beschreibung der Lorentzverschiebung (siehe Kapitel 2.2.2). Das Detektormodell wurde so in die Simulationssoftware `cbmroot` eingebaut, dass sich die einzelnen physikalischen Effekte separat aktivieren und untersuchen lassen. Dabei ergibt sich, daß sowohl Diffusion als auch Signalübersprechen die Zahl der ansprechenden Detektorsegmente und auch die Clustergröße erhöht. Nicht-uniformer Energieverlust und Elektronikrauschen verschlechtern die räumliche Auflösung) siehe Kapitel 2.2.2.4).

Das neue Detektormodell wurde wiederum mit experimentellen Daten überprüft; dabei wurden Prototypdetektoren im Teilchenstrahl unter Variierung des Strahldurchtrittswinkels betrieben und die resultierenden Clustergrößen betrachtet. Das realistische Modell stimmt besser mit den Teststrahldaten überein als das vorige Modell. Die Berücksichtigung der parasitischen Kapazitäten hat dabei den größten Einfluss (siehe Kapitel 4.3). Das realistische Modell ist seit 2017 Standard in `cbmroot`. Ein Vergleich des STS-Verhaltens mit dem einfachen und dem realistischen Modell wird in Kapitel 2.3 diskutiert. Das einfache Modell unterschätzt den Pile-up-Effekt mit 1,6 % digis, entsprechend zwei oder mehr Monte Carlo-Punkten, gegenüber 2,9 % vom realistischen Modell. Die Zahl der aktivierten Streifen wird ebenfalls vom einfachen Modell unterschätzt: Im Durchschnitt liefert es 7040 Streifen per Ereignis, gegenüber 7360 beim realistischen Modell. Diese Größen sind wichtig für die korrekte Auslegung des Datenaufnahmesystems DAQ, und natürlich auch für die Qualität der erzielten räumlichen Auflösung; sie wird sonst bei großen Clustern von 3 und

mehr Streifen um $5\,\mu\text{m}$ überschätzt. Die Rate von falschen kombinatorischen Treffern vergrößert sich von 33,4 % auf 36,5 % bei Berücksichtigung der realistischen Effekte. Gleichzeitig ändert sich die Spurrekonstruktionsleistung des STS nur leicht. Die Impulsauflösung bleibt gleich, da sie vom Effekt der Vielfachstreuung dominiert wird.

Ein einfaches Detektormodell führt daher zu einer falschen Einschätzung des Detektorvorhaltens. Die Wahl des korrekten Modells muss experimentellen Daten standhalten, wobei verschiedene Effekte auseinander gehalten werden müssen.

CLUSTER- UND HIT-REKONSTRUKTION. Der neue Algorithmus zur Clusterbestimmung wurde so konzipiert, dass er unvoreingenommen arbeitet, also im Durchschnitt Null-Residuen für jeden Satz von registrierten Clustern liefert (siehe Kapitel 3.1.2). Das führt zu kleineren Residuen im Vergleich mit dem weitverbreiteten Schwerpunkt-Algorithmus. Verschiedene Effekte wie Rauschen, Schwelleneinstellungen und andere, die in Fig. 3.13 gezeigt sind, verschlechtern die Ortsauflösung, so dass die Residuenverteilung alleine den unvoreingenommenen Algorithmus nicht bevorzugt (siehe Kapitel 3.1.3). Jedoch ist dieser Algorithmus mathematisch korrekt, kann besser rechnerisch implementiert werden und liefert ein analytisches Resultat des Positionsfehlers.

Zur korrekten Abschätzung der Fehler der Spurparameter im STS sind zwei Komponenten besonders wichtig: die Vielfachstreuung im Detektormaterial und die intrinsische Auflösung des Detektors (der Positionsfehler der Hits). Das geht auch in die χ^2 -Kenngröße der Spurrekonstruktion ein, die wichtig für die Auswahl korrekter Spurkandidaten in der Datenanalyse ist. Die entwickelte Methode wird in Kapitel 3.3.2 vorgestellt. Sie verbindet verschiedene unabhängige Komponenten: den Cluster-Positionsalgorithmus selbst, den nicht-uniformen Energieverlust, das Elektronikrauschen und die Diskretisierung der Ladung. Die Methode arbeitet a priori und benötigt nur die auf den Streifen gemessenen Ladungen. Der so bestimmte Positionsfehler kann direkt vom Spurrekonstruktionsalgorithmus verwendet werden. Die Methode zur Bestimmung der Positionsfehler wurde wie folgt validiert (siehe Kapitel 3.3.3):

- korrekte Pull-Verteilungen der Hits (Breite von etwa 1 und Form wie die der Residuenverteilung) erzielt;
- korrekte Kovarianzmatrix vom Kalman Track Fitter berechnet:
 - 5 – 10 % schmalere Residuenverteilung der Spurparameter;
 - korrekte Pull-Verteilungen der Spurparameter (Breite von etwa 1 und gaussische Form), was auf korrekte Diagonalelemente der Kovarianzmatrix deutet;
 - χ^2/ndf -Verteilung der Spuren mit Durchschnittswert $1,151 \pm 0,003$ und einer flacheren p-Verteilung im Vergleich zur vereinfachten Annahme mit $\text{pitch}/\sqrt{12}$. Dadurch wird die Abschätzung der Diagonal- und Nichtdiagonalelemente der Kovarianzmatrix als korrekt bestätigt.

Die Methode zur Bestimmung der Hitpositionsfehler verbessert die Teilchenrekonstruktion: die Verteilung der p-Werte für rekonstruierte $J/\psi \rightarrow \mu^+\mu^-$ -Zerfälle ist flach und nicht wie in [112, p.106], wo ein Fehler $\text{pitch}/\sqrt{12}$ verwendet wurde. Weitere Quellen zur Fehlerbestimmung werden im folgenden hinzugefügt. Die Schwelle der Ausleseelektronik ist dabei die nächst wichtige.

ERGEBNISSE DES TESTS IM PROTONENSTRAHL. Erste Prototypen der STS Detektormodule wurden 2013 und 2014 im relativistischen Protonenstrahl des COSY am Forschungszentrums Jülich, Deutschland, getestet. Ein Satz Module besaßen Sensoren in voller Größe ($6,2 \times 6,2 \text{ cm}^2$, Hersteller CiS) und Mikrokabel von 30 cm Länge. Die Ausleseelektronik wurde auf externen Karten angesteckt. Ein anderer Satz benutzte Sensoren des Herstellers Hamamatsu in $6,2 \times 4,2 \text{ cm}^2$ Größe, die vorher mit einer neutronen-äquivalenten Strahlungsdosis über die Lebensdauer im CBM-Experiment hin gealtert worden waren. Die Module mit CiS-Sensoren zeigten ein Signal-zu-Rauschen-Verhältnis von 10 – 15, was ausreichend für Spurrekonstruktion im CBM-Experiment mit hoher Effizienz ($> 95\%$) und einer Impulsauflösung $< 1,6\%$ ist. Strahlungsschädigung der Sensoren wird jedoch diese Leistung verschlechtern. Die Auswirkung der Strahlungsschädigung der Sensoren auf die Rekonstruktion ist in Kapitel 4.2.2 detailliert. Im Teststrahl wurde die Ladungssammungseffizienz (CCE)¹ bestimmt. Sie reduziert sich nach Bestrahlung der Sensoren zu $2 \times 10^{14} \text{ 1 MeV } n_{\text{eq}}/\text{cm}^2$, dem zweifachen des maximalen erwarteten Wertes im CBM-Experiment, auf 83 % (n-Seite) und 75 % (p-Seite).

Dabei wurde angenommen, dass die Mikrokabel die Sensorsignale uniform um 10 % verkleinern. Dies kann als eine untere Grenze der STS-Leistung interpretiert werden. Das Rauschen verstärkt sich um 50 – 75 %. Simulationen für den stark vereinfachenden Fall, dass alle Sensoren im STS derart gleich geschädigt sein sollten, die Spurrekonstruktionseffizienz von 95,5 % auf 93,2 % sinkt und die Impulsauflösung sich leicht von 1,6 % auf 1,7 % verschlechtert. Die Studie zeigt, dass die Leistungsfähigkeit des STS Detektors kritisch vom erzielten Signal-zu-Rausch-Verhältnis abhängt. Da die Signalgrößen der Sensoren durch ihre Dicke festgelegt sind, kommt der Verminderung des Rauschens eine hohe Bedeutung zu. Dies ist in der Hauptsache ein systembezogenes Problem und involviert optimierte das Design der einzelnen elektrischen Komponenten und ihre genaue Abstimmung aufeinander.

¹100 % CCE entspricht der Ladung gemessen mit nicht-bestrahlten Sensoren gleichen Typs.

*I do not mind if you think slowly, but I do object
when you publish more quickly than you think.*

Wolfgang Pauli

Bibliography

- [1] J. Schukraft, “QM2017: Status and Key open Questions in Ultra-Relativistic Heavy-Ion Physics,” *Nuclear Physics A*, vol. 967, no. Supplement C, pp. 1 – 10, 2017, the 26th International Conference on Ultra-relativistic Nucleus-Nucleus Collisions: Quark Matter 2017. [Online]. Available: <http://www.sciencedirect.com/science/article/pii/S0375947417301537>
- [2] M. Harrison, T. Ludlam, and S. Ozaki, “RHIC project overview,” *Nuclear Instruments and Methods in Physics Research A*, vol. 499, pp. 235–244, Mar. 2003.
- [3] G. Brianti, “Large Hadron Collider in the LEP Tunnel,” in *12th IEEE Particle Accelerator Conference*, 1987, p. 2008.
- [4] T. Gunji, “Overview of recent ALICE results,” *Nuclear Physics A*, vol. 956, pp. 11 – 18, 2016, the XXV International Conference on Ultrarelativistic Nucleus-Nucleus Collisions: Quark Matter 2015. [Online]. Available: <http://www.sciencedirect.com/science/article/pii/S0375947416001251>
- [5] A. Angerami, “Recent highlights from the ATLAS heavy-ion program ,” *Nuclear Physics A*, vol. 956, pp. 19 – 26, 2016, the XXV International Conference on Ultrarelativistic Nucleus-Nucleus Collisions: Quark Matter 2015. [Online]. Available: <http://www.sciencedirect.com/science/article/pii/S0375947416301427>
- [6] B. Hong, “Overview of recent heavy-ion results from CMS ,” *Nuclear Physics A*, vol. 956, pp. 27 – 34, 2016, the XXV International Conference on Ultrarelativistic Nucleus-Nucleus Collisions: Quark Matter 2015. [Online]. Available: <http://www.sciencedirect.com/science/article/pii/S0375947416000397>
- [7] A. Drees, “Highlights from PHENIX,” *Nuclear Physics A*, vol. 956, pp. 35 – 42, 2016, the XXV International Conference on Ultrarelativistic Nucleus-Nucleus Collisions: Quark Matter 2015. [Online]. Available: <http://www.sciencedirect.com/science/article/pii/S0375947416000312>

- [8] M. Mustafa, “Overview of recent results from the STAR experiment ,” *Nuclear Physics A*, vol. 956, pp. 43 – 50, 2016, the XXV International Conference on Ultrarelativistic Nucleus-Nucleus Collisions: Quark Matter 2015. [Online]. Available: <http://www.sciencedirect.com/science/article/pii/S037594741600110X>
- [9] F. Becattini, M. Bleicher, T. Kollegger, T. Schuster, J. Steinheimer, and R. Stock, “Hadron Formation in Relativistic Nuclear Collisions and the QCD Phase Diagram,” *Physical Review Letters*, vol. 111, no. 8, p. 082302, Aug. 2013.
- [10] Y. Aoki, G. Endrődi, Z. Fodor, S. D. Katz, and K. K. Szabó, “The order of the quantum chromodynamics transition predicted by the standard model of particle physics,” *Nature*, vol. 443, pp. 675–678, Oct. 2006.
- [11] K. Fukushima and T. Hatsuda, “The phase diagram of dense QCD,” *Reports on Progress in Physics*, vol. 74, no. 1, p. 014001, Jan. 2011.
- [12] P. Senger, “The heavy-ion program of the future FAIR facility,” in *Journal of Physics Conference Series*, ser. Journal of Physics Conference Series, vol. 798, Jan. 2017, p. 012062.
- [13] H. Heiselberg and M. Hjorth-Jensen, “Phases of dense matter in neutron stars,” *Phys. Rep.*, vol. 328, pp. 237–327, May 2000.
- [14] K. Ackermann, N. Adams, C. Adler, Z. Ahammed, and et al., “STAR detector overview,” *Nuclear Instruments and Methods in Physics Research Section A: Accelerators, Spectrometers, Detectors and Associated Equipment*, vol. 499, no. 2, pp. 624 – 632, 2003, the Relativistic Heavy Ion Collider Project: RHIC and its Detectors. [Online]. Available: <http://www.sciencedirect.com/science/article/pii/S0168900202019605>
- [15] STAR Collaboration, M. M. Aggarwal, Z. Ahammed, A. V. Alakhverdyants, I. Alekseev, and et al., “An Experimental Exploration of the QCD Phase Diagram: The Search for the Critical Point and the Onset of De-confinement,” *ArXiv e-prints*, Jul. 2010.
- [16] A. László, Z. Fodor, and G. Vesztegombi, “New Results and Perspectives on R_{AA} Measurements Below 20 GeV Cm-Energy at Fixed Target Machines,” *International Journal of Modern Physics E*, vol. 16, pp. 2516–2521, 2007.
- [17] G. Trubnikov, “Heavy ion collider facility NICA at JINR (Dubna): status and development,” in *Proceedings of the 36th International Conference on High Energy Physics (ICHEP2012)*, 2012, p. 554.

- [18] G. Agakichiev, C. Agodi, H. Alvarez-Pol, E. Atkin, and et al., “The high-acceptance dielectron spectrometer HADES,” *European Physical Journal A*, vol. 41, pp. 243–277, Aug. 2009.
- [19] BM@N Conceptual Design Report 2012. [Online]. Available: http://bmshift.jinr.ru/wiki/lib/exe/fetch.php?media=bmn_cdr.pdf
- [20] FAIR Baseline Technical Report 2006. [Online]. Available: http://www.fair-center.eu/fileadmin/fair/publications_FAIR/FAIR_BTR_1.pdf
- [21] B. Friman, C. Höhne, J. Knoll, S. Leupold, J. Randrup, R. Rapp, and P. Senger, “The CBM physics book: Compressed baryonic matter in laboratory experiments,” *Lect. Notes Phys.*, vol. 814, pp. pp.1–980, 2011.
- [22] I. C. Arsene, L. V. Bravina, W. Cassing, Y. B. Ivanov, A. Larionov, J. Randrup, V. N. Russkikh, V. D. Toneev, G. Zeeb, and D. Zschesche, “Dynamical phase trajectories for relativistic nuclear collisions,” *Phys. Rev. C*, vol. 75, no. 3, p. 034902, Mar. 2007.
- [23] M. D’Agostino, M. Bruno, F. Gulminelli, F. Cannata, P. Chomaz, G. Casini, E. Geraci, F. Gramegna, A. Moroni, and G. Vannini, “Nuclear Liquid-Gas Phase Transition: Experimental Signals,” *Nuclear Physics A*, vol. 749, pp. 55–64, Mar. 2005.
- [24] R. Rapp and H. van Hees, “Thermal dileptons as fireball thermometer and chronometer,” *Physics Letters B*, vol. 753, pp. 586–590, Feb. 2016.
- [25] J. Steinheimer, J. Auvinen, H. Petersen, M. Bleicher, and H. Stöcker, “Examination of directed flow as a signal for a phase transition in relativistic nuclear collisions,” *Phys. Rev. C*, vol. 89, no. 5, p. 054913, May 2014.
- [26] P. Braun-Munzinger, J. Stachel, and C. Wetterich, “Chemical freeze-out and the QCD phase transition temperature,” *Physics Letters B*, vol. 596, pp. 61–69, Aug. 2004.
- [27] M. A. Stephanov, “Sign of Kurtosis near the QCD Critical Point,” *Physical Review Letters*, vol. 107, no. 5, p. 052301, Jul. 2011.
- [28] J.-W. Chen, J. Deng, and L. Labun, “Baryon susceptibilities, non-Gaussian moments, and the QCD critical point,” *Phys. Rev. D*, vol. 92, no. 5, p. 054019, Sep. 2015.
- [29] T. Matsui and H. Satz, “ J/ψ suppression by quark-gluon plasma formation,” *Physics Letters B*, vol. 178, pp. 416–422, Oct. 1986.

- [30] P. M. Hohler and R. Rapp, “Is ρ -meson melting compatible with chiral restoration?” *Physics Letters B*, vol. 731, pp. 103–109, Apr. 2014.
- [31] N. Herrmann, J. P. Wessels, and T. Wienold, “Collective Flow in Heavy-Ion Collisions,” *Annual Review of Nuclear and Particle Science*, vol. 49, pp. 581–632, 1999.
- [32] H. Oeschler, H. G. Ritter, and N. Xu, “Hadron Production in Heavy Ion Collisions,” *Landolt Börnstein*, vol. 23, p. 111, 2010.
- [33] Y. Hatta, A. Monnai, and B.-W. Xiao, “Elliptic flow difference of charged pions in heavy-ion collisions,” *Nuclear Physics A*, vol. 947, pp. 155–160, Mar. 2016.
- [34] T. Ablyazimov, A. Abuhoza, R. P. Adak, M. Adamczyk, and et al., “Challenges in QCD matter physics - The scientific programme of the Compressed Baryonic Matter experiment at FAIR,” *European Physical Journal A*, vol. 53, p. 60, Mar. 2017.
- [35] “CERN Courier: Public Information Office (PIO), Publication.” [Online]. Available: <http://iopp.fileburst.com/ccr/archive/CERNCourier2017JulAug-digitaledition.pdf>
- [36] Compressed Baryonic Matter experiment. [Online]. Available: <http://www.fair-center.eu/for-users/experiments/nuclear-matter-physics/cbm/introduction.html>
- [37] A. Malakhov and A. Shabunov, Eds., *Technical Design Report for the CBM Superconducting Dipole Magnet*. Darmstadt: GSI, 2013. [Online]. Available: <http://repository.gsi.de/record/109025>
- [38] P. Kurilkin, P. Akishin, A. Bychkov, E. Floch, and et al., “Quench calculations for the superconducting dipole magnet of CBM experiment at FAIR,” in *Journal of Physics Conference Series*, ser. Journal of Physics Conference Series, vol. 742, Aug. 2016, p. 012017.
- [39] P. Klaus, M. Wiebusch, S. Amar-Youcef, M. Deveau, M. Koziel, J. Michel, B. Milanovic, C. Müntz, T. Tischler, and J. Stroth, “Prototyping the read-out chain of the CBM Microvertex Detector,” *Journal of Instrumentation*, vol. 11, p. C03046, Mar. 2016.
- [40] V. Friese*, C. Sturm*, and A. Toia*, Eds., *CBM Progress Report 2015*. Darmstadt: GSI, 2016, literaturang. [Online]. Available: <http://repository.gsi.de/record/186952>

- [41] I. Selyuzhenkov and A. Toia, Eds., *CBM Progress Report 2016*. Darmstadt: GSI, 2017, literaturangaben. [Online]. Available: <http://repository.gsi.de/record/201318>
- [42] “Technical Design Report for the CBM Ring Imaging Cherenkov Detector,” Tech. Rep., 2013. [Online]. Available: <http://repository.gsi.de/record/65526>
- [43] J. Adamczewski-Musch, P. Akishin, K.-H. Becker, S. Belogurov, and et al., “The CBM RICH project,” *Nuclear Instruments and Methods in Physics Research A*, vol. 845, pp. 434–438, Feb. 2017.
- [44] —, “The CBM RICH detector,” *Journal of Instrumentation*, vol. 11, p. C05016, May 2016.
- [45] S. Chattopadhyay, Y. P. Viyogi, P. Senger*, W. F. J. Müller*, and C. J. Schmidt*, Eds., *Technical Design Report for the CBM : Muon Chambers (MuCh)*. Darmstadt: GSI, 2015. [Online]. Available: <http://repository.gsi.de/record/161297>
- [46] R. P. Adak, A. Kumar, A. K. Dubey, S. Chattopadhyay, S. Das, S. Raha, S. Samanta, and J. Saini, “Performance of a large size triple GEM detector at high particle rate for the CBM Experiment at FAIR,” *Nuclear Instruments and Methods in Physics Research A*, vol. 846, pp. 29–35, Feb. 2017.
- [47] N. Herrmann, Ed., *Technical Design Report for the CBM Time-of-Flight System (TOF)*. Darmstadt: GSI, 2014. [Online]. Available: <http://repository.gsi.de/record/109024>
- [48] M. Petriş, D. Bartoş, G. Caragheorgheopol, I. Deppner, and et al., “Time and position resolution of high granularity, high counting rate MRPC for the inner zone of the CBM-TOF wall,” *Journal of Instrumentation*, vol. 11, p. C09009, Sep. 2016.
- [49] Y. Wang, X. J. Huang, P. F. Lyu, D. Han, and et al., “A solution for the inner area of CBM-TOF with pad-MRPC,” *Nuclear Instruments and Methods in Physics Research A*, vol. 845, pp. 318–321, Feb. 2017.
- [50] I. E. Korolko, M. S. Prokudin, and Y. M. Zaitsev, “The CBM Ecal,” in *Journal of Physics Conference Series*, ser. Journal of Physics Conference Series, vol. 798, Jan. 2017, p. 012164.
- [51] V. Friese and C. Sturm, Eds., *CBM Progress Report 2014*. Darmstadt: GSI, 2015. [Online]. Available: <http://repository.gsi.de/record/97909>
- [52] V. Akishina, “Four-dimensional event reconstruction in the CBM experiment,” Ph.D. dissertation, 2016.

- [53] S. Gorbunov, “On-line reconstruction algorithms for the CBM and ALICE experiments,” Dr., Johann Wolfgang Goethe-Universität Frankfurt, 2013, johann Wolfgang Goethe-Universität Frankfurt, Diss., 2013. [Online]. Available: <http://repository.gsi.de/record/206421>
- [54] J. Heuser, W. Müller, V. Pugatch, P. Senger, C. J. Schmidt, C. Sturm, and U. Frankenfeld, Eds., *[GSI Report 2013-4] Technical Design Report for the CBM Silicon Tracking System (STS)*. Darmstadt: GSI, 2013. [Online]. Available: <http://repository.gsi.de/record/54798>
- [55] K. Kasinski and W. Zubrzycka, “Testing and test set-up of STS/MUCH-XYTER2 ASIC,” 2017, the 29th CBM Collaboration Meeting. [Online]. Available: <https://indico.gsi.de/event/4759/session/11/contribution/56/material/slides/0.pdf>
- [56] M. Singla, P. Larionov, T. Balog, J. Heuser, H. Malygina, I. Momot, I. Sorokin, and C. Sturm, “Radiation tolerance studies of neutron irradiated double sided silicon microstrip detectors,” *Nuclear Instruments and Methods in Physics Research A*, vol. 824, pp. 462–464, Jul. 2016.
- [57] P. Larionov, “Systematic irradiation studies and Quality Assurance of silicon strip sensors for the CBM Silicon Tracking System,” Ph.D. dissertation, Goethe-Universität in Frankfurt am Main, 2016. [Online]. Available: <http://d-nb.info/1118512162/04>
- [58] R. Kleczek, “Analog front-end design of the STS/MUCH-XYTER2 — full size prototype ASIC for the CBM experiment,” *Journal of Instrumentation*, vol. 12, p. C01053, Jan. 2017.
- [59] A. S. Brogna, S. Buzzetti, W. Dabrowski, T. Fiutowski, B. Gebauer, M. Klein, C. J. Schmidt, H. K. Soltveit, R. Szczygiel, and U. Trunk, “N-XYTER, a CMOS read-out ASIC for high resolution time and amplitude measurements on high rate multi-channel counting mode neutron detectors,” *Nuclear Instruments and Methods in Physics Research A*, vol. 568, pp. 301–308, Nov. 2006.
- [60] G. Lutz, *Semiconductor Radiation Detectors*. Springer, 2001.
- [61] H. Spieler, *Semiconductor Detector Systems*. Oxford University Press, 2005.
- [62] W. Müller, *CBM Progress Report 2009*. Darmstadt: GSI, 2010. [Online]. Available: <http://repository.gsi.de/record/54081>
- [63] E. Belau, R. Klanner, G. Lutz, E. Neugebauer, and et al., “Charge collection in silicon strip detectors,” *Nuclear Instruments and Methods in Physics Research*, vol. 214, pp. 253–260, Sep. 1983.

- [64] B. Kolbinger, “Simulation of a Silicon-Strip Detector,” Nov. 2012. [Online]. Available: http://personalpages.to.infn.it/~cartigli/Weightfield2/Manual_files/Manual_Weightfield.pdf
- [65] W. Dabrowski, P. Gryboś, and M. Idzik, “Study of spatial resolution and efficiency of silicon strip detectors with different readout schemes,” *Nuclear Instruments and Methods in Physics Research A*, vol. 356, pp. 241–254, Feb. 1995.
- [66] The ATLAS Collaboration, “Operation and performance of the ATLAS semiconductor tracker,” *Journal of Instrumentation*, vol. 9, p. P08009, Aug. 2014.
- [67] R. Brun, F. Bruyant, F. Carminati, S. Giani, M. Maire, A. McPherson, G. Patrick, and L. Urban, “GEANT Detector Description and Simulation Tool,” 1994.
- [68] R. Turchetta, “Spatial resolution of silicon microstrip detectors,” *Nuclear Instruments and Methods in Physics Research A*, vol. 335, pp. 44–58, Oct. 1993.
- [69] S. Straulino, O. Adriani, L. Bonechi, M. Bongi, and et al., “Spatial resolution of double-sided silicon microstrip detectors for the PAMELA apparatus,” *Nuclear Instruments and Methods in Physics Research A*, vol. 556, pp. 100–114, Jan. 2006.
- [70] P. Koppenburg, “A simulation of charge deposition and collection in silicon microstrip detectors,” Tech. Rep., Sep. 2001. [Online]. Available: http://lpheserv2.epfl.ch/publications/iphe_01_001.ps.gz
- [71] K. Lassila-Perini and L. Urbán, “Energy loss in thin layers in GEANT,” *Nuclear Instruments and Methods in Physics Research A*, vol. 362, pp. 416–422, Feb. 1995.
- [72] H. Bichsel, “Inelastic electronic collision cross sections for Monte Carlo calculations,” *Nuclear Instruments and Methods in Physics Research B*, vol. 52, pp. 136–139, Dec. 1990.
- [73] “Resolution of the Layer00 Silicon Detector for Various Configurations.” [Online]. Available: <http://hep.ph.liv.ac.uk/cdf/sidesign/sidesign.html>
- [74] M. Brigida, C. Favuzzi, P. Fusco, F. Gargano, and et al., “A new Monte Carlo code for full simulation of silicon strip detectors,” *Nuclear Instruments and Methods in Physics Research A*, vol. 533, pp. 322–343, Nov. 2004.
- [75] Z. Drasal, “Simulation of charge collection in semiconductor microstrip detectors,” Ph.D. dissertation, Charles U., 2006.

- [76] M. Jeong and M. D. Hammig, “The Atomistic Simulation of Thermal Diffusion and Coulomb Drift in Semiconductor Detectors,” *IEEE Transactions on Nuclear Science*, vol. 56, pp. 1364–1371, Jun. 2009.
- [77] V. Bartsch, W. de Boer, J. Bol, A. Dierlamm, E. Grigoriev, F. Hauler, S. Heising, and L. Jungermann, “An algorithm for calculating the Lorentz angle in silicon detectors,” *Nuclear Instruments and Methods in Physics Research A*, vol. 497, pp. 389–396, Feb. 2003.
- [78] I. Sorokin, “Characterization of silicon microstrip sensors, front-end electronics, and prototype tracking detectors for the CBM experiment at FAIR,” Ph.D. dissertation, Goethe-Universität in Frankfurt am Main, 2013. [Online]. Available: http://fias.uni-frankfurt.de/helmholtz/publications/thesis/Iurii_Sorokin.pdf
- [79] N. Harnew, “The physics performance of LHCb,” *Nuclear Instruments and Methods in Physics Research A*, vol. 408, pp. 137–145, Feb. 1998.
- [80] R. Aaij, A. Affolder, K. Akiba, M. Alexander, and et al., “Performance of the LHCb Vertex Locator,” *Journal of Instrumentation*, vol. 9, p. P09007, Sep. 2014.
- [81] M. A. Parker, “The ATLAS detector for the LHC,” in *American Institute of Physics Conference Series*, ser. American Institute of Physics Conference Series, vol. 272, Feb. 1992, pp. 1837–1841.
- [82] T. Aaltonen, S. Behari, A. Boveia, B. Brau, and et al., “Operational experience, improvements, and performance of the CDF Run II silicon vertex detector,” *Nuclear Instruments and Methods in Physics Research A*, vol. 729, pp. 153–181, Nov. 2013.
- [83] M. Pearce, “The status of the PAMELA experiment,” *Nuclear Physics B Proceedings Supplements*, vol. 113, pp. 314–321, 2002.
- [84] O. Adriani, G. Barbarino, G. Bazilevskaya, R. Bellotti, and et al., “The PAMELA Mission: Heralding a new era in precision cosmic ray physics,” *Physics Reports*, vol. 544, no. 4, pp. 323 – 370, 2014, The PAMELA Mission: Heralding a new era in precision cosmic ray physics . [Online]. Available: <http://www.sciencedirect.com/science/article/pii/S0370157314002087>
- [85] Stopping-power and range tables for electrons. [Online]. Available: <http://physics.nist.gov/PhysRefData/Star/Text/ESTAR.html>
- [86] Stopping-power and range tables for protons. [Online]. Available: <http://physics.nist.gov/PhysRefData/Star/Text/PSTAR.html>

- [87] S. T. Perkins, D. E. Cullen, and S. M. Seltzer, “Tables and graphs of electron-interaction cross sections from 10 eV to 100 GeV derived from the LLNL Evaluated Electron Data Library (EEDL), $Z = 1$ to 100,” Tech. Rep., Nov. 1991.
- [88] H. Tai, H. Bichsel, J. W. Wilson, J. L. Shinn, F. A. Cucinotta, and F. F. Badavi, “Comparison of Stopping Power and Range Databases for Radiation Transport Study,” NASA, Tech. Rep., 10 1997.
- [89] Range and stopping power of ions in various materials. [Online]. Available: http://www.kayelaby.npl.co.uk/atomic_and_nuclear_physics/4_5/4_5_1.html
- [90] K. Kasinski, R. Kleczek, and R. Szczygiel, “Front-end readout electronics considerations for Silicon Tracking System and Muon Chamber,” *Journal of Instrumentation*, vol. 11, no. 02, p. C02024, 2016. [Online]. Available: <http://stacks.iop.org/1748-0221/11/i=02/a=C02024>
- [91] C. Canali, G. Majni, R. Minder, and G. Ottaviani, “Electron and hole drift velocity measurements in silicon and their empirical relation to electric field and temperature,” *IEEE Transactions on Electron Devices*, vol. 22, pp. 1045–1047, Nov. 1975.
- [92] I. Panasenko, “Capacity Measurements, Electrical QA of Sensors,” 2016, the 28th CBM Collaboration Meeting. [Online]. Available: <https://indico.gsi.de/getFile.py/access?contribId=45&sessionId=24&resId=0&materialId=slides&confId=3960>
- [93] M. Singla, “The Silicon Tracking System of the CBM experiment at FAIR: development of microstrip sensors and signal transmission lines for a low-mass, low-noise system,” Ph.D. dissertation, 2014. [Online]. Available: <http://publikationen.ub.uni-frankfurt.de/frontdoor/index/index/docId/33060>
- [94] I. Sorokin, private communication.
- [95] V. Friese and C. Sturm, Eds., *CBM Progress Report 2012*. Darmstadt: GSI, 2013. [Online]. Available: <http://repository.gsi.de/record/54078>
- [96] K. Kasinski, R. Szczygiel, R. Kleczek, and P. Otfinowski, “Status of the STS-XYTER2 ASIC,” 2016, the 28th CBM Collaboration Meeting. [Online]. Available: <https://indico.gsi.de/getFile.py/access?contribId=40&sessionId=24&resId=1&materialId=slides&confId=3960>
- [97] V. Akishina and I. Kisel, “Parallel 4-Dimensional Cellular Automaton Track Finder for the CBM Experiment,” in *Journal of Physics Conference Series*, ser. Journal of Physics Conference Series, vol. 762, Oct. 2016, p. 012047.

- [98] I. Kisel, I. Kulakov, and M. Zyzak, “Standalone First Level Event Selection Package for the CBM Experiment,” *IEEE Transactions on Nuclear Science*, vol. 60, pp. 3703–3708, Oct. 2013.
- [99] H. Malygina, “Detector inefficiency study,” 2015, CBM-STs Workgroup Meeting. [Online]. Available: <https://indico.gsi.de/event/3886/>
- [100] —, “STs performance simulation for different sensor thickness,” 2017, CBM-STs Workgroup Meeting. [Online]. Available: <https://indico.gsi.de/event/6265/>
- [101] —, “Investigation into the particle identification potential of the CBM Silicon Tracking System @FAIR,” 2017, Wilhelm and Else Heraeus Physics School: QCD - Old Challenges and New Opportunities. [Online]. Available: https://indico.cern.ch/event/614845/contributions/2728866/attachments/1530947/2397106/38_HMalygina.pdf
- [102] H. Malygina, V. Friese, and M. Zyzak, “Hit reconstruction in the CBM Silicon Tracking System,” in *2016 IEEE Nuclear Science Symposium, Medical Imaging Conference and Room-Temperature Semiconductor Detector Workshop (NSS/MIC/RTSD)*, Oct 2016, pp. 1–6.
- [103] H. Malygina, V. Friese, and C. Collaboration, “A precision device needs precise simulation: Software description of the CBM Silicon Tracking System,” *Journal of Physics: Conference Series*, vol. 898, no. 4, p. 042022, 2017. [Online]. Available: <http://stacks.iop.org/1742-6596/898/i=4/a=042022>
- [104] D. Simon, *Optimal State Estimation: Kalman, H Infinity, and Nonlinear Approaches*. Wiley-Interscience, 2006.
- [105] G. R. Lynch and O. I. Dahl, “Approximations to multiple Coulomb scattering,” *Nuclear Instruments and Methods in Physics Research B*, vol. 58, pp. 6–10, May 1991.
- [106] D. Hutchcroft, “VELO Pattern Recognition,” CERN, Geneva, Tech. Rep. LHCb-2007-013. CERN-LHCb-2007-013, Mar 2007. [Online]. Available: <http://cds.cern.ch/record/1023540>
- [107] C. Parkes, T. Ruf, and T. Szumlak, “Reconstruction of Cluster Positions in the LHCb Velo,” CERN, Geneva, Tech. Rep. LHCb-2007-151. CERN-LHCb-2007-151, Dec 2007. [Online]. Available: <https://cds.cern.ch/record/1074928>
- [108] C.-E. Wulz, “CMS concept and physics potential,” in *Particle Physics and Cosmology, First Tropical Workshop*, ser. American Institute of Physics Conference Series, J. F. Nieves, Ed., vol. 444, Oct. 1998, pp. 467–478.

- [109] The CMS Collaboration, “Description and performance of track and primary-vertex reconstruction with the CMS tracker,” *J. Instrum.*, vol. 9, no. arXiv:1405.6569. CERN-PH-EP-2014-070. CMS-TRK-11-001, p. P10009. 80 p, May 2014, comments: Replaced with published version. Added journal reference and DOI. [Online]. Available: <http://cds.cern.ch/record/1704291>
- [110] K. A. Olive and Particle Data Group, “Review of Particle Physics,” *Chinese Physics C*, vol. 38, no. 9, p. 090001, Aug. 2014.
- [111] S. Meroli, D. Passeri, and L. Servoli, “Energy loss measurement for charged particles in very thin silicon layers,” *Journal of Instrumentation*, vol. 6, p. 6013, Jun. 2011.
- [112] M. Zyzak, “Online selection of short-lived particles on many-core computer architectures in the CBM experiment at FAIR,” Ph.D. dissertation, 2016. [Online]. Available: <http://publikationen.ub.uni-frankfurt.de/frontdoor/index/index/docId/41428>
- [113] H. M. J. Hung, R. T. O’Neill, P. Bauer, and K. Kohne, “The behavior of the p-value when the alternative hypothesis is true,” *Biometrics*, vol. 53, no. 1, pp. 11–22, 1997. [Online]. Available: <http://www.jstor.org/stable/2533093>
- [114] S. Gorbunov, U. Kebschull, I. Kisel, V. Lindenstruth, and W. F. J. Müller, “Fast SIMDized Kalman filter based track fit,” *Computer Physics Communications*, vol. 178, pp. 374–383, Mar. 2008.
- [115] COSY. Der Beschleuniger am Standort Jülich. [Online]. Available: http://www.fz-juelich.de/ikp/ikp-4/DE/Forschung/Beschleuniger/_node.html
- [116] Test Beam Time @ COSY, December 2013. [Online]. Available: <https://cbm-wiki.gsi.de/foswiki/bin/view/Beamtime/BeamTimeCosyDec2013>
- [117] “CBM Progress Report 2013,” Darmstadt, Tech. Rep. CBM Progress Report, 2014. [Online]. Available: <http://repository.gsi.de/record/64893>
- [118] C. Pauly, private communication.
- [119] CiS Forschungsinstitut für Mikrosensorik GmbH. [Online]. Available: <http://www.cismst.org/>
- [120] Test boards for STS microstrip detectors. [Online]. Available: <https://cbm-wiki.gsi.de/foswiki/bin/view/STS/STSTestBoards>
- [121] Hamamatsu. [Online]. Available: <http://www.hamamatsu.com/us/en/index.html>

-
- [122] P. Senger, Ed., [*GSI Report 2008-04*] *CBM Progress Report 2007*. Darmstadt: GSI, 2008. [Online]. Available: <http://repository.gsi.de/record/54084>
- [123] J. Adamczewski-Musch, H. G. Essel, and S. Linev, “The DABC Framework Interface to Readout Hardware,” *IEEE Transactions on Nuclear Science*, vol. 58, pp. 1728–1732, Aug. 2011.
- [124] I. Sorokin, T. Balog, V. Krylov, and C. J. Schmidt, “Transconductance calibration of n-XYTER 1.0 readout ASIC,” *Nuclear Instruments and Methods in Physics Research A*, vol. 714, pp. 136–140, Jun. 2013.
- [125] *The n-XYTER Reference Manual*. [Online]. Available: <https://cbm-wiki.gsi.de/foswiki/pub/Public/PublicNxyter/nXYTER.pdf>
- [126] V. Friese and C. Sturm, Eds., *CBM Progress Report 2011*. Darmstadt: GSI, 2012. [Online]. Available: <http://repository.gsi.de/record/54080>

Acknowledgments

This work was only possible with the promotion of Peter Senger, Johann Heuser, and the Helmholtz Graduate School for the Heavy Ion Research (HGS-HIRe). I am sincerely thankful to them for the opportunity to joined the STS group and for supporting me to the very end of my PhD project.

I would like to express my gratitude to Volker Frieze, who guided me in my research and helped to keep a critical eye on my work. Moreover, he gave me inspiring examples of efficient code development. Special thanks come to Iaroslav Panasenko, Iurii Sorokin and Maksym Zyzak: fruitful discussions with them result in parts of the thesis. I am very grateful to Christian Sturm, who helped me to take the global view of my work. I thank the referees, Peter Senger and Joachim Stroth, for reading this not-easy-to-read peace of text and agreeing to be on my PhD brainstorming. My sincere gratitude comes to Maksym Teklishyn for eclectic support. I would also like to thank Johann Heuser and Volker Frieze for helping with translations to German. I am deeply indebted to all the readers of my manuscript: Johann Heuser, Volker Frieze, Maksym Teklishyn, Maksym Zyzak, Christian Sturm, Anton Lymanets, Mykola Malygin, Iurii Sorokin (names randomly ordered). Many thanks come to my colleagues and friends, it was really a great pleasure to work with all of them. My deep gratitude comes to my husband, Mykola Malygin, for providing me with inexhaustible pieces of advice in physics, programming, thesis writing, and social skills. I am thankful to Valery Pugatch, who enlightened me the first glance of research.

I express my deep thanks to my family, my husband and two daughters, who continuously provide me with support, understanding and love, which is impossible to overestimate.

Hanna Malygina

GSI Helmholtzzentrum für Schwerionenforschung
Goethe University Frankfurt

Hirschstrasse 20
64291 Darmstadt

+49 (0) 157 34889021

✉ gannamalygina@gmail.com
h.malygina@gsi.de

Personal Information

born January 1988, Ukraine
marital status married, 2 kids
maiden name Melnyk

Languages

English fluent
German conversational
Ukrainian native
Russian native

Computer Skills

Advanced C, C++, ROOT, L^AT_EX, VIM.
Basic MPI, OpenMP, LabView, GEANT4,
shell, Origin, HTML, CSS, svn, git.

Education

- 2011 - 2018 **PhD**, *Goethe University, Frankfurt, Germany*, “Hit reconstruction for the Silicon Tracking System of the CBM experiment”.
- 2009 - 2011 **MSc**, *Taras Schevchenko National University of Kyiv, Ukraine*, Diploma magna cum lauda for “Development of the Detector Elements for CBM Experiment”.
- 2005 - 2009 **BSc**, *Taras Schevchenko National University of Kyiv, Ukraine*, Diploma magna cum lauda for “Research of the Characteristics of the Detector Module Prototype for Silicon Tracker for CBM Experiment”.

Experience

- 2011 - 2018 **PhD**, *GSI Helmholtzzentrum für Schwerionenforschung GmbH, Darmstadt, Germany*, Silicon Tracking System (STS) group of the CBM experiment, under supervision of Prof. Dr. P. Senger, Dr. J.M. Heuser, Dr. V. Frieese.
Responsible for detector response simulation and its validation, development of reconstruction algorithms.
- developed the response model of silicon micro-strip detectors that is a default model in CBM and is employed to make optimised STS design decisions;
 - assembled and commissioned the detector prototypes for three beam tests;
 - developed the beam-test measurement concept and assembled the suitable beam test setup;
 - conducted the beam-test measurements required to finalise the STS design;
 - expanded the data reduction and data analysis, with which validated the developed detector response model;
 - improved the algorithms for cluster and hit reconstruction, implemented the suitable ones for STS.
- 2008 - 2011 **Engineer**, *High Energy Physics Department, Kyiv Institute for Nuclear Research (KINR), Ukraine*, for the STS group of the CBM, under supervision of Prof. Dr. V. Pugatch.
- results of my characterisation of sensor and readout electronics were used in next design of detector prototypes.
- 2010 **Teaching assistant**, *Nuclear Physics Department, Taras Schevchenko National University of Kyiv, Ukraine*, Practical course of C++ with Windows Visual Studio for undergraduates, under supervision of Dr. R. Iermolenko.

Softskill Courses

- “Making an Impact as an Effective Researcher”, February, 2012.
- “Leading Teams in a Research Environment”, June, 2017.
- “Leadership and Career Development”, June, 2017.

Publications

- H. Malygina, V. Friese and M. Zyzak, *Hit reconstruction in the CBM Silicon Tracking System*, in 2016 IEEE Nuclear Science Symposium, Oct 2016, pp.1-6.
- H. Malygina, V. Friese for the CBM Collaboration, *A precision device needs precise simulation: Software description of the CBM Silicon Tracking System*, Journal of Physics: Conference Series, vol. 898, no. 4, p. 042022, 2017.
- Ablyazimov, T and other (CBM Collaboration), *Challenges in QCD matter physics -The scientific programme of the Compressed Baryonic Matter experiment at FAIR*, The European Physical Journal A, Vol. 53, Issue 3, 2017, p.14.
- M. Singla, P. Larionov, T. Balog, J. Heuser, H. Malygina, I. Momot, I. Sorokin, C. Sturm, For the CBM Collaboration, *Radiation tolerance studies of neutron irradiated double sided silicon microstrip detectors*, Nuclear Instruments and Methods in Physics Research Section A, Vol. 824, 2016, pp. 462–464.
- CBM Progress Report and GSI Progress Report 2008, 2009 (2 contr.), 2010, 2011 (2 contr.), 2012, 2013 (2 contr.), 2014, 2015 (3 contr.), 2016 (3 contr.).
- KINR Annual Report 2009, 2011, 2012, 2013.

Conferences

- **IEEE Nuclear Science Symposium (NSS)** 2016, Strasbourg, France (poster): *Realistic hit reconstruction in the CBM Silicon Tracking System*;
- **Computing in High Energy and Nuclear Physics (CHEP)** 2016, San-Francisco, USA (talk at parallel session): *A precision device needs precise simulation: Software description of the CBM Silicon Tracking System*;
- **Deutsche Physikalische Gesellschaft (DPG) Spring Meeting**, Germany:
 - 2017 (talk at parallel session): *Hit position error estimation for the CBM STS*;
 - 2016 (talk at parallel session): *The detector response simulation for the CBM Silicon Tracking System as a tool for the hit error estimation*;
 - 2015 (talk at parallel session), 2014 (talk at parallel session): *An improved detector response simulation for the CBM STS*.
- **Quark Matter** 2014, Darmstadt, Germany.
- **Annual Scientific Conference**, KINR, Kyiv, Ukraine:
 - 2012 (talk): *First test of the nXYTER-chip for sensors for the Silicon Tracking System for CBM experiment in external trigger mode*;
 - 2011 (talk): *Quality Assurance System for sensors for the Silicon Tracking System for CBM experiment with nXYTER*.

Workshops, Lectures, Schools, Meetings

- HGS-HIRe Power Week on Efficient Programming, Schmitten, Germany, 2017;
- WE-Heraeus Physics School: QCD - Old Challenges and New Opportunities, Bad Honnef, Germany, 2017 (Best Student Talk Award);
- Introduction to High Performance Computing. Parallelization with MPI and OpenMP, Frankfurt, Germany, 2017;
- Matter and Technology Annual Meeting, Darmstadt, Germany, 2017 (poster);
- Matter and Technology Student retreat, Darmstadt, Germany, 2017 (talk);
- CBM Collaboration Meeting, March 2017, September 2016 (talk), April 2016, September 2015 (talk), April 2015, April 2014.
- HGS-HIRe Power Week on Detectors and Readout Electronics, Frankfurt, Germany, 2016.
- Matter and Technologies Annual Meeting, Karlsruhe, Germany, 2016 (poster);
- 607th WE-Heraeus-Seminar on “Semiconductor detectors in astronomy, medicine, particle physics and photon science”, Bad Honnef, Germany, 2016 (poster);
- HGS-HIRe Lecture Week on Hadron Physics, Kloster Marienburg, Germany, 2014.
- HADES & CBM Winter School, Kloster Hoechst, Germany, 2014.
- Fifth Meeting of the CBM-MPD Consortium, Alushta, Ukraine, 2011 (talk);
- 13th International Moscow School of Physics (38th ITEP Winter School of Physics), Session “Particle Physics”, Moscow, Russia, 2010.
- Winter High Energy Physics School, Kyiv, Ukraine, 2010.
- Trans-European School of High Energy Physics, Zakopane, Poland, 2009 (talk).